THESE DE DOCTORAT DE L'UNIVERSITE PARIS 13

INSTITUT GALILEE

Mention **Science de L'Ingénieur**

Option **Génie des Procédés**

Présentée et soutenue publiquement par

Khley CHENG

Pour obtenir le titre de

Docteur de l'Université Paris 13

Elaboration de nano-photocatalyseurs mixtes à base d'oxide de métal $Zr_xTi_{1-x}O_2$

Elaboration of mixed metal oxide $Zr_xTi_{1-x}O_2$ nano-photocatalysts

---

Directeur de thèse: Andrei KANAEV

Co-directeur de thèse: Khay CHHOR

Soutenue le 11 avril 2018

Devant le jury composé de:

Christophe COLBEAU-JUSTIN	Professeur, Université Paris 11	Rapporteur
Sophie CASSAIGNON	Professeur, Sorbonne Université	Rapporteur
Rabah AZOUANI	Professeur de l' EBI	Examinateur
Khay CHHOR	Professeur, Université Paris 13	Co-directeur de thèse
Andrei KANAEV	Directeur de Recherche CNRS	Directeur de thèse
Dominique VREL	Directeur de Recherche CNRS	Président

Laboratoire des Science des Procédés et des Matériaux CNRS UPR 3407

Acknowledgment

This PhD work was performed in Laboratoire des Sciences des Procédés et des Matériaux (LSPM CNRS UPR 3407) of CNRS at the Paris 13 University, and I would like to express my gratitude to all people who helped me during all three years of this work.

Firstly, I am deeply grateful to my PhD supervisor, Andrei KANAEV, Research director CNRS, head of group Inorganic Nanomaterials (NINO). He was a great and kind supervisor giving me good advices and ideas in research and teaching, especially, in writing scientific papers. Because of this, there are many articles issued of this PhD work.

I also would like to thank my co-supervisor, professor Khay CHHOR, who introduced me in life in France since the beginning and accompanied during all these years. He transmitted me important knowledge concerning experiment and chemical synthesis, and helping in reduction and correction of this manuscript.

Beside my supervisors, I want to thank Dominique VREL, Research director CNRS, who helped in interpretation of data of X-ray diffraction and structural analysis of the elaborated materials.

I would like to thank professor Khalid Hassouni, Director of LSPM, for a permission to perform this study in laboratory.

I thank professor Christophe Colbeau-Justin, professor Sophie Cassaignon and assistant professor Rabah AZOUANI for the acceptance to take part in PhD defense jury and evaluate this PhD work.

My sincere thank also goes to the permanent members of NINO team, especially assistant professors Mamadou Traore, Mohamed Amamra, Mounir Ben Amar and professor Mehrdad Nikravech for providing me an intellectual assistance in course of this study.

I would like to thank Valéri Bockelee for x-ray diffraction measurements, Ovidui BRINZA for transmission electron microscopy (TEM and EFTEM) measurements and Patrick Portes for specific surface area (BET) measurements and other permanent help. I thank computer and network administrator **Greg Chalvignac** and secretaries Chrystel Redon, Nathalie Duros and Sandrine Ouazan for a permanent assistance in course of my stay at LSPM.

I want to thank my many friends, who colored my everyday' life with fruitful human and scientific discussions and for much other: Easeng SIV (admission and repairing computer), Didier FANOU (admission and experimental collaboration), Sana LABIDI and Paola DIAZGOMEZ TREVINO (purchase of chemicals and materials). I will not forget other friends and PhD student: Mine ER, Sarah DINE, Benoit BAUDRILLART, Abdelkader RAHMANI, Annika PILLE, Khaled OUAHA, Zixian Jia and many others.

Additionally, I would like to offer my special thank to international science programme (ISP) teams in both Sweden and Cambodia countries, especially Professor Peter SUNDIN and Dr. Sorya PROUM for the scholarship covering my living expenses in France.

Last but not the least, I thank to family: my wife and my son, my parents and my brothers who have been waiting for me so long time.

General introduction

General introduction

The composite materials are those made of two or more individual components. As a result, it has significantly different structure and chemical and physical properties than its pure components that can be useful for different application fields. Among other advantages, they can be lighter, stronger with a higher melting point or even cheaper materials compared to the traditionally used. The general uses of composite materials are: (i) aerospace industrials, constructing buildings, bridges and airplanes, (ii) sporting good industrials constructing race car bodies, storage tanks, swimming pool panels, (iii) automotive industrials constructing motor vehicles, (iv) home application industrials constructing electrical and mechanical devices, etc. Consequently, synthesis of composite materials is between important activities world-wide.

Between different composite materials, metal oxides take a special place. One of important fields of their application is environmental protection. In fact, they are stable semiconducting materials providing a strong photocatalytic activity under light illumination, which offer an opportunity for a band gap engineering controlled by smooth compositional changes. Their activity may be even enhanced compared to their pure constituting components. As a result, these materials are considered nowadays as an alternative to the pure photocatalytic materials (e.g. TiO_2, ZnO) modification by anionic and cationic doping.

Elimination of the environmental pollution in ambient air and potable waters is of priority concern in the developed and developing countries worldwide, which set high standards for the pollution by volatile organic compounds and chemicals. The photocatalysis is most effective method permitting elimination of toxic organic compounds by their oxidation/reduction towards carbon dioxide and water. The most known material for photocatalysis applications with high activity, low cost, long time stability and chemical safety is titanium dioxide or TiO_2. TiO_2 generally exhibits an important photocatalytic activity being in anatase crystalline phase. However, this activity is limited by electron-hole recombination and use of ultraviolet sources of light. Much effort has been employed in the past to enhance this activity and/or promote it to the visible spectral range, permitting the process efficiency increase. Between different solutions, anion and cation doping and mixing with other metal oxides, such as Fe_2O_3, ZnO, CuO, ZrO_2, V_2O_5…etc., have been considered.

Despite of many advantages in use, mixed metal oxides exhibited different photocatalytic activities (higher, smaller or inactive) depending of preparation conditions

and methods, such as polymer gel templating, mechanical mixing, solvothermal, spray pyrolysis co-precipitation, sol-gel, etc. One of principal obstacle in preparation of a photocatalyst with stable and reproducible functional properties is the control of its compositional homogeneity at nanoscale. Indeed, inhomogeneities may appear at the preparation stage during mechanical or chemical syntheses resulting to the elemental and/or phase material clustering, which let to heterogeneous materials with far from optimal structural properties and related electronic band structure. The save fabrication of such functional solids cannot be controlled.

In our study, we interested in preparation of stable binary metal oxides, which main component is the most efficient photocatalyst TiO_2. By employing sol-gel synthesis combined with reactor micromixing techniques, the homogenous materials can be successfully realized by insertion of other cations into TiO_2 matrix at the particle nucleation stage. We used Zr as an inserted cation because of the comparable oxidation numbers and ionic radii. In the same time, much different band gap energies make possible bang gap engineering by tuning the elemental composition of solid solutions from x=Zr/(Ti+Zr) from 0 to 100%. The main risk related to this elaboration concerns reactivities of the metal oxide precursors that may result in co-nucleation of different pure metal oxide units instead of the composite ones. To achieve macroscopic quantities (grams) of the composite size-selected nuclei, one has to strictly control the preparation conditions, understand and made a right choice of key parameters of the total process, controlled by the Damköhler number: $Da=t_{mix}/t_{nucl}$, where t_{mix} and t_{nucl} are respectively characteristic times of physical mixing and solid nucleation processes. The resulting Ti/Zr oxo-alkoxy nanoparticles with a high monodispersity and compositional homogeneity would be considered as excellent building blocks for novel functional bulk solids, because they can form mechanically adherent layers on complex-form substrates of different natures without changing properties.

TiO_2 composites with ZrO_2 are known for applications in catalysts, sensitized solar cell, etc. They can advantageously form porous ceramics with improved mechanical properties. In the field of environmental photocatalysis, the obtained results concerning the optimal composition and activity strongly differ, which may be explained by heterogeneity of the obtained materials. In our work, we aimed to prepare the composite $Zr_xTi_{1-x}O_2$ solids ($0\leq x\leq 1$) by nucleation of size-selected zirconium-titanium oxo-alkoxy (ZTOA) nanoparticles in a sol-gel chemical reactor with ultrarapid micromixing of the reacting fluids in a turbulent flow, which is equipped with atmosphere and temperature control and in-situ particles granulometry ($R\geq 1$ nm). After a careful examination of influence of the

preparation conditions and nucleation-growth process (including their heat treatment and modification of crystalline phases: ZTOA→*a*-$Zr_xTi_{1-x}O_2$→cryst1→cryst2, etc.), glass beads will be coated with these nanoparticles and used as photocatalytic media in a continuous flow fix-bed reactor for ethylene decomposition. The obtained results with be compared with literature data to make a definite conclusion on the role of the material homogeneity.

This PhD thesis contains five chapters.

In chapter I, we made bibliography review concerning (i) TiO_2 synthesis by focusing on nucleation-growth kinetics, its physical and chemical properties and applications including photocatalysis, (ii) ZrO_2 with emphasis of the nucleation and growth process and (iii) ZrO_2-TiO_2 composites putting forward synthesis methods, structures including phase transitions, bonding, band gap energy, applications with more detailed survey of the domain of photocatalysis. The principle of dynamic and static light scattering (DLS/SLS) and sol-gel reactor with ultra-rapid micromixing developed in LSPM laboratory was also described.

The principle measurement techniques and characterization methods employed in this study will be described in chapter II: thermal analysis TGA/DTA, X-ray diffraction, Brunauer–Emmett–Teller (BET), transmission emission spectroscopy (TEM), UV-visible optical absorption, inductively coupled plasma-optical emission spectroscopy (ICP-OES), etc.

Chapter III is devoted to experimental studies of the nucleation and growth process of composite ZTOA species in a large range of the elemental compositions $0 \leq x = Zr/(Ti+Zr) \leq 1$. We studied effect of solvent nature (n-propanol and isopropanol) on size of titanium oxo-alkoxy nanoparticles and influence of the precursors (Zr and Ti) concentrations and hydrolysis ratio on size of ZTOA nanoparticles.

Chapter IV describes structural properties of the prepared nanoparticles after heat treatment at temperatures from 0 to 800 °C. The characterization techniques TGA/DTA, X-ray diffraction, BET, TEM, UV-visible optical absorption and ICP-OES were used. The crystalline phases of the obtained $Zr_xTi_{1-x}O_2$ solids were analyzed and the transitions onset temperatures for anatase, orthorhombic, monoclinic and tetragonal phases were established in correlation with the ZTOA nucleus size. The electronic band gaps were measured depending on the elemental composition x. The nanoporous morphology and single crystalline nature of $Zr_xTi_{1-x}O_2$ particles is emphasized.

Chapter V presents experimental results of photocatalytic activity of the prepared nanocoatings made of preformed ZTOA nanoparticles. The activity underwent detailed studies on ethylene decomposition in a fix-bed continuous-flow gas-phase reactor and more

general evaluation of the activity is made in an aqueous phase on methylene blue and phenol decompositions in a batch stirred reactor, with UVA light illumination. The photocatalytic activity is connected to the nucleus size, composition and heat treatment temperature. We conclude about optimum composition x=0.0425 of $Zr_xTi_{1-x}O_2$, which activity is considerably higher when that of the pure anatase TiO_2.

General conclusions and perspectives, which summarizes main results of this study and proposition for future studies in the domain of the composite nanomaterials.

Bibliography references and Annex conclude the manuscript.

Chapter I: Literature review

This bibliography chapter will first describe the structural properties of TiO_2, ZrO_2 and ZrO_2-TiO_2 composite as well as the technique of their preparation. This part is followed by the description of kinetics studies on the nucleation and growth of titanium and zirconium oxo-alkoxide nanoparticles carried out manually or by using a micromixing sol-gel reactor. Finally, optical properties and photocatalytic applications of materials are exposed.

I.1 Materials and their structural properties

I.1.1 Titanium dioxide (TiO_2)

There are many polymorphous of TiO_2 [1] and the well known phases are anatase, brookite and rutile [2, 3]. Their representative crystallographic structures are shown in the Figure I-1.

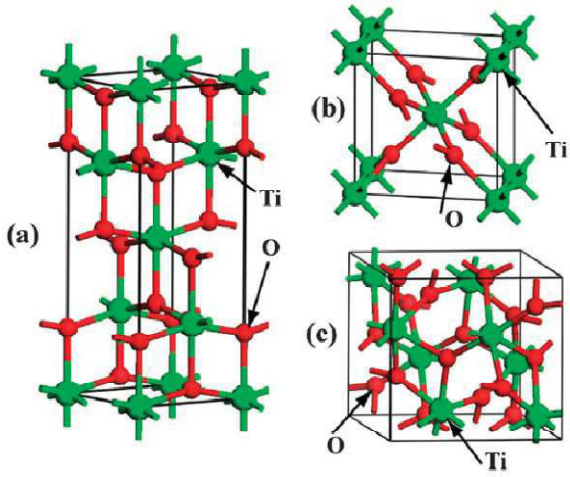

Figure I-1: Representative crystallographic structures of TiO_2 (a) anatase, (b) rutile and (c) brookite: The green color is Ti and red color is O [4].

Crystallographic structures of these three phases are summarized in refs [5, 6]. **Anatase** has a cell volume of 131 $Å^3$ in a tetragonal crystal structure with lattice parameters, $a = b$ =3.73 Å and c = 9.37Å. The length of Ti-O bonds is 1.94 and 1.97 Å. The density and the refractive index of this form are respectively 3.79 g/cm^3 and 2.55. **Rutile** crystallizes in tetragonal crystal structure associated with a cell volume of 62 $Å^3$ and lattice constants, $a = b$ = 4.58 Å and c = 2.95 Å. The Ti-O bonding lengths are equal to 1.95 and 1.98 Å. The density and refractive index are respectively equal to 4.13 g/cm^3 and 2.75. **Brookite** has a density of 4.17 g/cm^3 and a cell volume equal to 256 $Å^3$ in a rhombohedral crystal structure with a = 5.44, b = 9.17 and c = 5.13 Å. These data are summarized in table I-1.

Table I-1: TiO_2 structural properties of anatase, rutile and brookite

Phases	Ti-O bonding lengths (Å)	Lattice parameters	Lattice volume ($Å^3$)	Density	Structural system
Anatase	1.94 1.97	$a = 3.73$ $b = 3.73$ $c = 9.37$	131	3.79	tetragonal
Rutile	1.95 1.98	$a = 4.58$ $b = 4.58$ $c = 2.95$	62	4.13	tetragonal
Brookite	1.96*	$a = 5.44$ $b = 9.17$ $c = 5.13$	256	4.17	rhombohedral

* The Ti-O bonding length was taken from ref [7].

I.1.2 Zirconium dioxide (ZrO_2)

Zirconium oxide, called zirconia (ZrO_2), is a ceramic material that crystallizes mainly in three distinct stable crystalline structures with different temperatures [8]. These three allotropic forms stable at relatively low temperature are presented in Figure I-2. This is zircon α which crystallizes in the monoclinic phase and is stable from room temperature to 1170°C and zircon β phase of tetragonal symmetry which is stable in the temperature range from 1170 °C to 2370 °C[9]. The structure of this last polymorph derives from a small distortion from a cubic symmetric structure of ZrO_2 called zircon γ. This cubic phase is stable at high temperature from 2370 °C to melting point at 2680 °C.

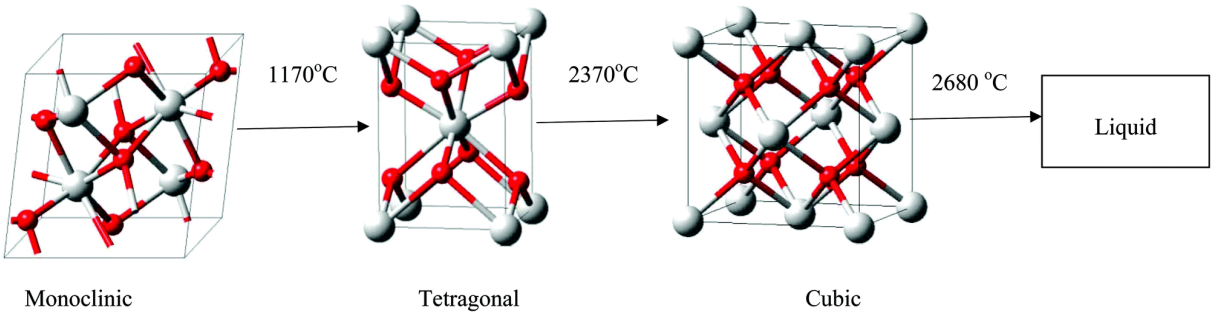

Figure I-2: Crystallographic structures of monoclinic tetragonal and cubic ZrO_2 (red color is O and white color is Zr) [10].

The characteristics of these phases are the following: **Monoclinic** ZrO_2 has a cell volume equal to 144 $Å^3$ with lattice constants, a = 5.17, b = 5.23 and c = 5.34 Å [9]. **Tetragonal**

form has a lattice volume of 67 $Å^3$ with a = b = 3.61 and c = 5.15 Å [8]. The cubic phase parameters are as follows: a = b = c = 5.09 Å, α = β = γ = 90 °. Zr-O bonds lengths are 2.05, 2.06, 2.15 and 2.16 Å for monoclinic cell, 2.10 and 2.35 Å for tetragonal cell and 2.20 Å for cubic cell [11]. The lattice volume and density are respectively 132 $Å^3$ and 6.09 g/cm^3. These structural data are summarized in table I-2.

Table I-2: Some structural properties of monoclinic, tetragonal and cubic ZrO_2.

Phases	Zr-O bonding lengths (Å) [11]	Lattice parameters (Å) [8, 9]	Lattice volume ($Å^3$)	Density (g/cm^3) [12]
Monoclinic	2.05 2.06 2.15 2.16	a = 5.17 b = 5.23 c = 5.34	144	5.83
Tetragonal	2.10 2.35	a = 3.61 b = 3.61 c = 5.15	67	6.10
Cubic	2.20	$a = b = c$ = 5.09	132	6.09

I.1.3 Composite zirconium-titanium oxide (ZrO_2-TiO_2)

There are many compositions of ZrO_2-TiO_2 composite prepared for different applications. Most of them are used as catalysts, supported catalysts or composite catalyst. These last materials can be obtained by mixing with metals or metal oxides such as Pt, Ag, In ... and vanadium oxide etc)) [13]. The compositions employed in these applications essentially correspond to a zirconium content x ≤ 0.5 (x is defined as follows: $0 \le x = n_{Zr} / (n_{Zr+Ti}) \le 0.5$ n = zirconium mole number). Frequently, the composite with x = 0.5 is suitable for catalysis and x <0.5, particularly x < 0.2, is used in photocatalysis. TiO_2-ZrO_2 composite has also been used for applications such as water photosplitting [14-17], controlled acid-base properties[18-20], ceramics of high hardness [21-23], dyes solar cells [24-28], chromatography [29], high capacity adsorbents [30-33], ceramic membranes for microfiltration [34-37] etc.

A. Effect of composition on phase transformation temperatures

TiO_2-ZrO_2 composites with high zirconium and titanium contents are non-crystalline when starting mixed amorphous powders obtained from sol-gel [18, 38-40], or coprecitation reactions [41, 42] are calcinated up to 600 °C [18, 38-42] while pure TiO_2 and ZrO_2 are well crystalline at this temperature range. Several authors have shown that the crystallization of the TiO_2-ZrO_2 composite depends strongly on the composition of the starting oxides TiO_2 and ZrO_2. The closer their content in the material is the higher the crystallization temperature [39, 40, 43]. As an example, for TiO_2-ZrO_2 with composition 10:1, the crystallization takes place at 500 °C [44]. When the mixture is equimolar, the composite forms a defined monophasic compound $ZrTrO_4$, called Zirconium Titanate [45]. This solid crystallizes at a higher temperature, from 600 °C [43] to 712 °C [40]. This change observed in crystallization temperature may be due to the difference in the homogeneity level of the initial mixture and/or preparation methods.

B. Effect of compositions on the composite crystal structure

Aust et al [37] reported the results on the crystallization behaviour of ZrO_2-TiO_2 binaries oxide, prepared sol-gel method. From DTA and X-ray diffraction techniques, the crystalline structures and transformation temperatures of ZrO_2-TiO_2 composite were found to depend strongly on the composition of oxide precursors. The major domains of the transformation temperature from amorphous to crystalline phase as function of TiO_2 and ZrO_2 composition were shown in Figure I-3. According to this figure, from 60 to 100% of ZrO_2 molar content, the composite crystallizes in ZrO_2 tetragonal phase. From 30 to 60 % of ZrO_2 content, crystallization occurs in $ZrTiO_4$ orthorhombic phase and from 0 to 30% the crystallization in TiO_2 anatase phase was observed.

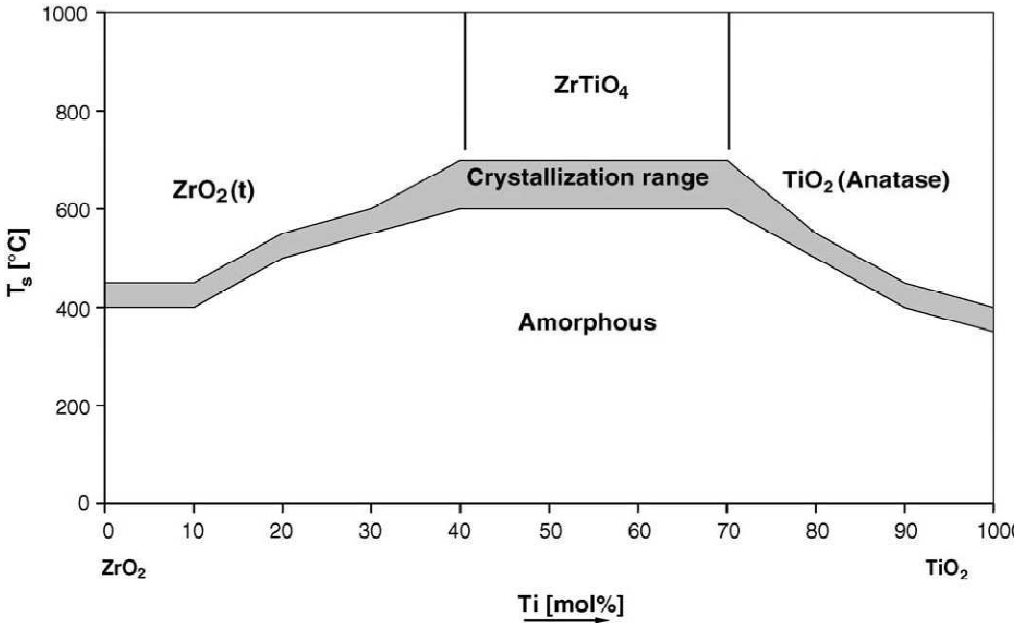

Figure I-3: Phase domains and transformation temperature of mixed ZrO_2-TiO_2 composite as function of TiO_2 and ZrO_2 composition [37].

Zhu et al [46] synthesized $Zr_xTi_{1-x}O_2$ composite in nine compositions (x = 0.1, 0.2, …, 0.9) using sol-gel dry-spinning method and the materials were calcinated at 1050 °C. The major phases found by these authors were similar to those mentioned by Aust et al. [37].

In a structural study between 0 to 50% ZrO_2 content, Kitiyanan et al [47] observed that the mixed ZrO_2-TiO_2 binaries were in anatase phase up to 40% ZrO_2 content and they became crystalline at 500 °C. These results were slightly different from Aust et al [37], which showed that the maximum loading of ZrO_2 into TiO_2 was only 30% with higher transformation temperatures (≈ 700°C instead of 500 °C).

Liang et al [48] investigated on various phases of ZrO_2-TiO_2 films obtained by sol-gel method. Five compositions as well as pure TiO_2 and ZrO_2 were prepared: ZrTi91, ZT73, ZT55, ZrTi37 and ZrTi19. When materials were treated at 700 °C, the usual results were observed for the two pure solids: mixed tetragonal and monoclinic phases for pure ZrO_2 and mixed anatase and rutile for TiO_2, while ZrTi91 and ZrTi19 were tetragonal and anatase respectively. The three other compositions, namely ZT73, ZT55, and ZT37, crystallize in orthorhombic phase with a small fraction of teragonal and anatase respectively for ZrTi73 and ZrTi37. X-ray diffraction patterns of different solids obtained are compared in Figure I-4.

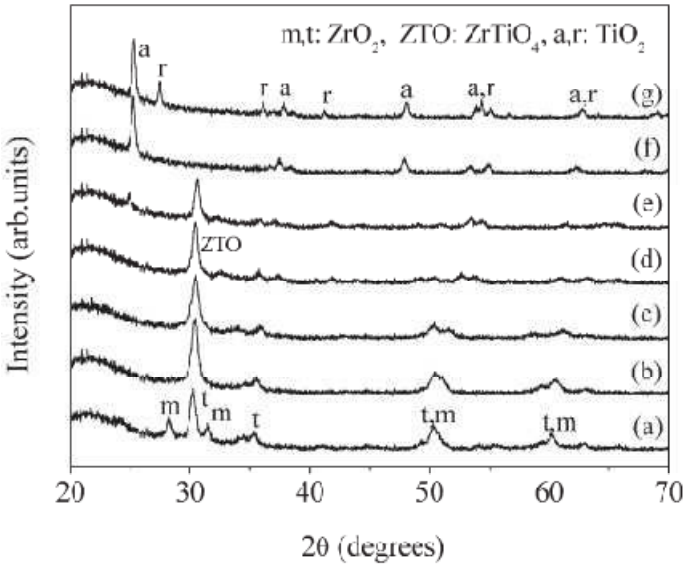

Figure I-4: X-ray patterns of mixed film samples after calcinations at 700 °C (a) ZrO_2,(b) ZrTi91, (c) ZrTi73, (d) ZrTi55, (e) ZrTi37, (f) ZrTi19 and (g) TiO_2 [48].

Gionco et al [49] used sol-gel method to synthesize this composite in range of 85-99.9 % ZrO_2 content. In range of 99-99.9 % ZrO_2 content, samples fired at 1273 K, crystallized in monoclinic phase and became tetragonal at lower percentages e.g. 85 and 90% of ZrO_2 content.

Effects of composition on anatase - rutile transformation

Different from pure titanium dioxide TiO_2, small amount of ZrO_2 in ZrO_2-TiO_2 composite significantly retarded phases transformation from anatase to rutile [47, 50-52]. Kitiyanan et al [47] reported that ZrO_2-TiO_2 composite with 5% ZrO_2 loading, the anatase-rutile phases transition was retained up to a temperature between 800-900 °C, while pure anatase TiO_2 transformed into rutile phase at a temperature around ~ 600 °C [53]. This finding was supported by the results of Kim et al [51], who found that, for composite with 10% ZrO_2 content, the transformation anatase-rutile took place in the temperature range 800-900 °C and between 900-1000 °C for material with 20 % ZrO_2 loading [52].

I.2 Composite ZrO_2-TiO_2 preparation

I.2.1 Preparation methods

Several methods used to develop the ZrO_2-TiO_2 composite have the objective of obtaining a homogeneous material. A review article published by Reddy et al [13] presents

the state of the art on the preparation techniques of this material. A number of techniques can be listed below: classical sol-gel [18, 24, 25, 37, 38, 48, 49, 54-58], coprecipitation [19, 41, 42, 59-66], polymer gel templating [33, 67], surfactant self-assembly [15, 30, 47, 68-70], micro-arc oxidation technique [71], ultrasonic spray pyrolysis [72], sol-gel/SCF extraction [73], solid state dispersion [74] etc.

Among these techniques, sol-gel process is the most popular because it produces high homogenous materials, processes at low temperature and provides the possibility to efficiently control particles size and morphology [75, 76].

I.2.2 Generality on sol-gel method

Sol-gel process for producing solid materials from metallic precursors has been well known for decades [77-79]. This method has become attractive in the fields of nanotechnology, particularly in optics, electronics, and biomaterials. The reactions taking place in this process involved in inorganic precursors and normally alcohols as solvents. To get the desired materials, the choosing precursor is one of the important factors. The most uses are metal alkoxides of general formula $M(OR)_n$, which M is metal atom with *n* valences, R is alkyl groups. 2 steps of mechanism occur during the process [80-83]:

(1) Hydrolysis: The mechanism of this reaction is based on nucleophilic substitution:

$$H_2O + M-O-R \rightarrow H-O-M + R-O-H$$

(2) Condensation: There are two possible reactions [84, 85]: alcoxolation and oxolation:

(i) Alcoxolation

Two molecules react in this reaction: precursor molecule and partly hydrolyzed precursor. The reaction mechanism can be written as following:

$$M-O-H + M-O-R \rightarrow M-O-M + R-O-H$$

The general reaction is:

$$(RO)_{n-x}M(OH)_x + M(OR)_n \leftrightarrow (RO)_{n-x}(OH)_{x-1}M-O-M(OR)_{n-1} + ROH$$

(ii) Oxolation

In this case, two partly hydrolysis precursors react each other and release water molecule according to the mechanism:

$$M-O-H + H-O-M \rightarrow M-O-M + H_2O$$

This equation can be generalized as:

$$(RO)_{n-x}M(OH)_x + (RO)_{n-y}M(OH)_y \leftrightarrow (RO)_{n-x}(OH)_{x-1}M-O-M(OH)_{y-1}(OR)_{n-y} + H_2O$$

The factors that are strongly affected the reactions are: nature of ligand groups or R-groups, hydrolysis ratios (concentrations of water) and catalysis concentrations [86].

With sol-gel method, a wide variety of materials can be produced in different forms including thin films, ceramics, fibers, powders, monoliths, porous gels etc. Various possibilities offered by sol-gel process are shown in Figure I-5 [87]. As shown in this figure, a sol is formed after precursors are hydrolyzed and condensed. The nature of products depends on the intermediated of the process such as gelling, coating, precipitating etc.

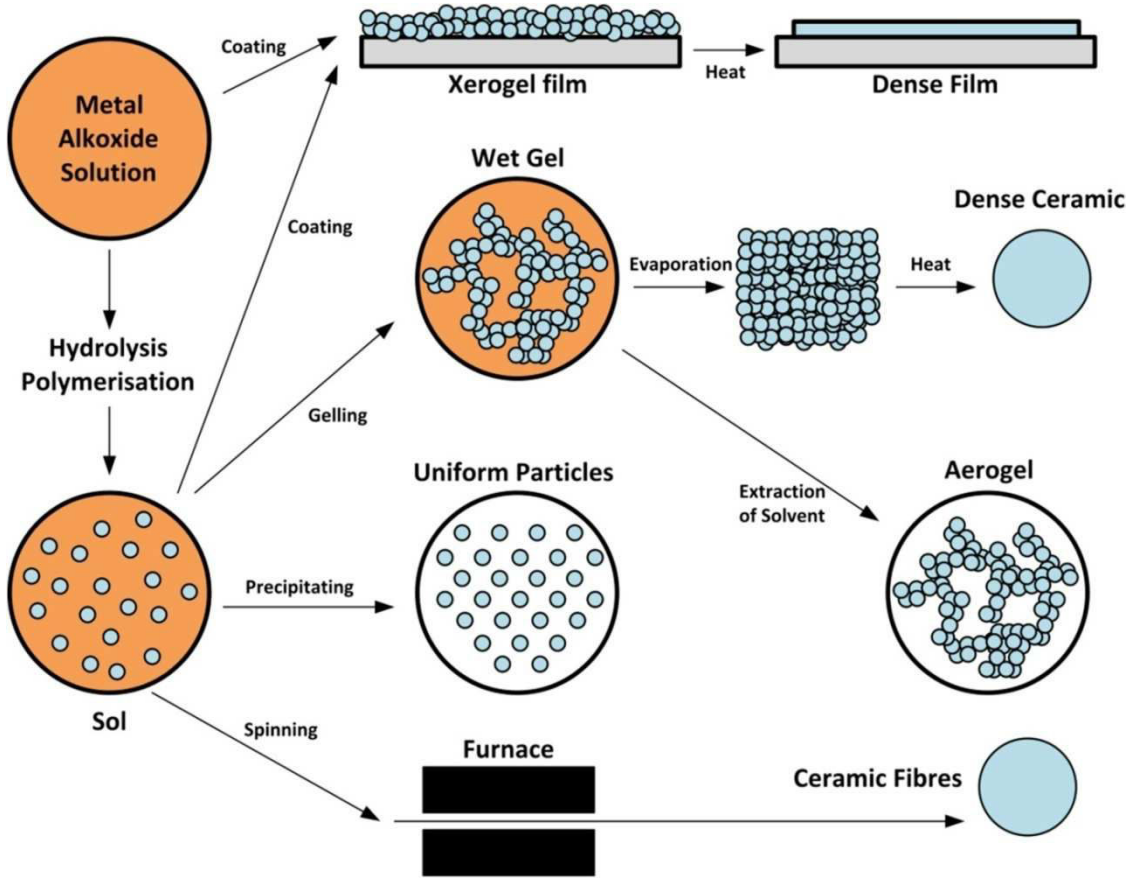

Figure I-5: The possible products in sol-gel process for technology and chemistry [87].

I.2.3 Sol-gel method for ZrO_2-TiO_2 preparation

Sol-gel method and its modifications have been carried out to synthesize materials of various compositions of mixed zirconium and titanium oxide by several researchers [18, 40, 48, 54, 56, 57, 69, 88, 89]. Ghiaci et al [69] reported about synthesis ZrO_2-TiO_2 composite. The mixture of zirconium(IV) isopropoxide and titanium(IV) n-butoxide precursor were in n-butanol and complex agent of 2,4-pentandione were added. Then this mixture was hydrolyzed with water containing surfactant of cetylpyridinium bromide. Sizes could be controlled by varying ratios of water and surfactant and concentration of reagent. Manríquez

et al [18] synthesized ZrO_2-TiO_2 composite as the following process: n-butoxides of titanium and zirconium were dissolved in n-butanol by adjusted solution with nitric acid to conserve pH 3.0. Then mixture solution of these precursors was hydrolyzed. The product of gel form was obtained. Zou et al [40] prepared this binary oxide by dissolving salts of titanium chloride ($TiCl_4$) and zirconium oxide chloride ($ZrClO_2$) in water separately. Hydroxides of titanium or zirconium were precipitated by addition of ammonium hydroxide. To obtain pure TiO_2 and ZrO_2, the hydrous precipitates were filtered and cleaned with distilled water. These hydrous precipitates were dissolved back in nitric acid. These titanium and zirconium nitrate solutions were mixed together in different rations to the desired compositions and then precipitated by adding ammonium hydroxide solution. Liang et al [48] reported about this composite using chelating agent of diethanolamine. Zirconium(IV) n-propoxide and titanium(IV) n-butoxide precursors were dissolved in diethanolamine solution (anhydrous ethanol as solvent). To obtain composite sol, this solution was rapidly mixed with another prepared water/ethanol solution. Neppolian et al [57] synthesized this binary oxide by dissolving the different weight ratios of TTIP and zirconium(IV) isopropoxide precursors in isopropanol solvent. After that this mixture solution was added dropwise into nitric acid solution of pH 1.5 under mechanical stirring. Aghabeygi et al [89] prepared titanium and zirconium gel separately at the beginning. For titanium gel, TTIP was diluted with isopropanol and then water by using nitric acid to adjust and conserve pH 1.5. H_2O_2 was added to get white suspension and this suspension was filtered and cleaned to obtain precipitate. For zirconium gel, $ZrCl_4$ was dissolved in isopropanol for producing precursor. H_2O_2 solution was added and pH was kept at 9 by adjusting with ammonium hydroxide. To mix ZrO_2-TiO_2 nanocomposite, the precipitation of titanium was introduced into gel of zirconium and mixed by utrasonic probe. Pirzada et al [88] prepared this nanocomplosite by dissolved $ZrOCl_2$ in methanol and TTIP solution (in methanol) was added. The reaction solution was maintained by chloridric acid of concentration from 2.0 to 5.0 mol/L. The translucent gel form was obtained.

Sol-gel reactions of mixed precursors zirconium (IV) and titanium(IV) butoxide (1:1) was proposed [90]:

1) $\mathrm{Ti(OR)_4 \cdot Zr(OR)_4 + 8H_2O = Ti(OH)_4 \cdot Zr(OH)_4 + 8ROH}$

2) $n\mathrm{Ti(OH)_4 \cdot Zr(OH)_4} + n\mathrm{Ti(OH)_4 \cdot Zr(OH)_4} = (\mathrm{Ti-O-Zr-O-Ti-Zr}) + n\mathrm{H_2O}$

I.3 Nucleation and growth processes of metal oxide particles

I.3.1 Particle size measurement (light scattering methods)

A. Light scattering

Static light scattering (SLS) and dynamic light scattering (DLS) are non-destructive spectroscopic analysis techniques that allows measuring correspondingly (i) light intensity scattered by ensample of nanoparticles and (ii) size of particles suspended in a liquid from 1 to 500 nm of diameter. Fluctuations evaluation is commonly known as dynamic light scattering (DLS) while absolute mean intensity analysis is known as static light scattering (SLS). From the intensity of fluctuations in the time of the scattered light by particles in suspension (Figure I-6) information on the dynamics of the particles within the solution are obtained.

Figure I-6 presented the intensity fluctuation of light scattered by particles in suspension when the sample was illuminated.

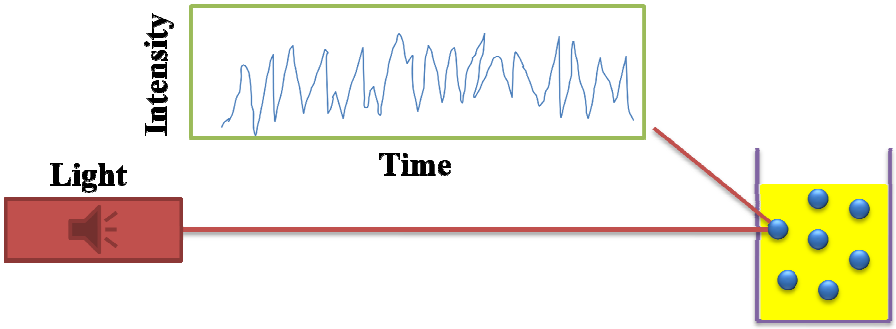

Figure I-6: Schematic diagram showing the scattering light from the particles suspended in a liquid.

B. Theories of DLS

In the condition that the particle radius is much smaller than the wavelength of incident light ($R << \lambda$), the following relation can be written:

$$\frac{2\pi nR}{\lambda} << 1 \qquad \textit{Equation I-1}$$

Where n is a refractive index of the particles. The theory of diffusion was developed by Rayleigh [91] and Van de hulst [92]. The light diffusion intensity depends on the observed angle and the equation can be given by the following equation:

$$I(\theta) = I_0 \frac{9\pi^2 {n_0}^4}{\lambda^4} \frac{V^2}{r^2} \left(\frac{m^2 - 1}{m^2 + 2} \right)^2 \frac{1 + \cos^2(\theta)}{2} \qquad \textit{Equation I-2}$$

Which θ, I_0 (Hz), n_0, V, r and $m = n/n_0$ are a diffusion angle, initial light intensity of the incident beam, a refractive index of medium, a real volume of the particle, a distance between particle and the observation point, and relative reflective index respectively.

From this equation, one can notice that:

i) The intensity, I , is proportional to the inverse of λ^4

$$I \propto \frac{1}{\lambda^4} \qquad \textit{Equation I-3}$$

ii) The scattered intensities forward at $\theta = 180°$ and backward at $\theta = 0°$ are the same $(Cos\ (\pi - \theta) = Cos\ \theta)$

$$I(\theta) = I(\pi - \theta) \qquad \textit{Equation I-4}$$

iii) The scattered intensity is proportional to the square of the volume of the particle

$$I \infty V^2 \qquad \textit{Equation I-5}$$

This relationship can be explained by assuming that a particle consists of N identical molecules and a molecule has the electric field scattered E. If the particle size is very small compared to the wavelength of the incident light, the scattered waves by N molecules are in phase. In this case, the total scattered electric field E_T is equal to the sum of the electric fields scattered by each molecule: $E_T = N.E$.

As the intensity of a radiation is proportional to the square of the associated electric field, the scattered intensity became:

$$I \propto {E_T}^2 = N^2 E^2 \propto N^2 \qquad \textit{Equation I-6}$$

For homogeneous particles, the density is the same at every points, its volume V is then proportional to N:

$$I \infty V^2 \qquad \textit{Equation I-7}$$

The particle shape does not matter; it can be a spherical or an open structure (fractal particles), provided that the inequality $\frac{2\pi nR}{\lambda} << 1$ is verified. For a dense spherical particle of radius R, it can be written:

$$I \infty R^6 \quad \left(V = \frac{4}{3} \pi R^3 \right) \qquad \textit{Equation I-8}$$

Furthermore, Soloviev and Rivallin et al [93-95] showed that for a particle with fractal dimension D_f , the intensity of the scattered light *I* is proportional to the average radius *R* of the particles raised to the power D_f .

$$I \infty R^{D_f} \qquad \textit{Equation I-9}$$

C. Measurements of particles hydrodynamic radius

The intensity of the dynamic scattering of DLS light was used to measure the hydrodynamic radius of the particles. The method is based on the Doppler Effect. When a particle is in Brownian motion in the fluid phase, the spectrum of scattered light widens; this is due to the Doppler Effect. Particles in the scattering volume that approach the observation point scatter the light with, and on the contrary, those that move away diffuse the light at a wavelength.

The hydrodynamic radius of particles can be estimated from the intensity of the dynamic light scattering DLS. The method is based on the ***Doppler Effect***. When a particle is in **Brownian** motion in the fluid phase, the spectrum of scattered light is broadening due to the ***Doppler Effect***. When a particles moves close to the observation point $\lambda' < \lambda$ and $\lambda'' > \lambda$ in the opposite direction. For the whole particles, this leads to a continuous broadening of the diffused spectrum. This process depends on the velocity of the particles: the higher the particle velocity is the more the spectrum broadening increases.

The particle radius *R* can be obtained from the Stokes-Einstein equation [96].

$$D = \frac{k_B T}{6\pi\mu R} \qquad \textit{Equation I-10}$$

Where *D,* μ (Pa.s), *T* (K) and $k_B = 1.3806\times10^{-23}\,\mathrm{J\cdot molecule^{-1}\cdot K^{-1}}$ are respectively diffusion coefficient, dynamic viscosity of the medium, temperature of medium and Boltzman constant. This relation showed that, the diffusion coefficient is proportional to the inverse of particles radius when the temperature is constant.

D. Theory of the dynamic light scattering

There are two possible parameters (i) particles in Brownian motion and (ii) the particles number in the observed diffusion volume, which induce the fluctuation of the light diffusion spectrum. Therefore, the temporal correlation function will provide the information about the spectrum of light diffusion intensity and then the particle size [97]. Cummins et al [98] and Pecora et al [99] have established the relationship between the

diffusion coefficient and the shape of the diffusion spectrum using the autocorrelation functions of the intensity and the electric field of the scattered wave. The expression of this function related to the electric field and the intensity of the light can be written as:

$$G^{(1)}(t') = \left\langle E_D^*(t) \cdot E_D(t+t') \right\rangle \qquad \textit{Equation I-11}$$

Where $\langle\ \rangle$ is the average value of the measurement and t' is correlation time.

The relation of $G^{(1)}$ with spectral intensity $I(\omega)$ is:

$$I(\omega) = \frac{1}{2\pi} \int_0^{\infty} G^{(1)}(t') \cdot e^{i\omega t'} \cdot dt' \qquad \textit{Equation I-12}$$

The normalized function $g^{(1)}$ of the autocorrelation from the electric field diffused by particles in Brownian motion with a diffusion coefficient D is given by the relation [99]:

$$g(t') \infty \exp(-Dq^2 t' - i\omega_0 t') \qquad \textit{Equation I-13}$$

- $g^{(1)}$ is the normalized form of $G^{(1)}$ with respect to the initial time. It is defined by

$$g^{(1)}(t') = \frac{G^{(1)}(t')}{G^{(1)}(0)} \qquad \textit{Equation I-14}$$

- $\omega_0 = 2\pi/v$ is the angular frequency (v is frequency) of the incident light
- $q = \frac{4\pi n_0}{\lambda} \sin\left(\theta/2\right)$ is the modulus of the diffusion wave vector. The inverse of the wave vector module, q^{-1}, represents the observation scale of the system fixed by the observation angle θ.

Of a half-width **Lorentzian**, the spectral intensity has the form $\Gamma = Dq^2$:

$$I(\omega) \propto \frac{\Gamma}{(\omega - \omega_0)^2 + \Gamma^2} \qquad \textit{Equation I-15}$$

The autocorrelation function of the intensity I can be written as

$$G^{(2)}(t') = \left\langle I_D(t) \cdot I_D(t+t') \right\rangle \ \textit{with}\ I_D = E^2 \qquad \textit{Equation I-16}$$

Its standardized form is

$$g^{(2)}(t') = \frac{G^{(2)}(t')}{G^{(2)}(0)} \qquad \textit{Equation I-17}$$

The correlation function of the diffused intensity $g^{(2)}$ is obtained from the data of the dynamic light scattering experiments. In case that light scattering follows Gaussian statistics (particles concentrations in the diffusion volume is high), $g^{(1)}$ and $g^{(2)}$ are linked by the relation [100] :

$$g^{(2)}(t') = \left|g^{(1)}(t')\right|^2 + 1 \qquad \textit{Equation I-18}$$

Finally

$$g^{(2)}(t') = 1 + e^{-2\Gamma t'} \qquad \textit{Equation I-19}$$

In the experiments of diffusion dynamic light scattering, the measured function is rather in the following form:

$$\tilde{G}^{(2)}(t') = A + B \cdot e^{-2\Gamma t'} \qquad \textit{Equation I-20}$$

In order to simplify the writing, we replace $\tilde{G}^{(2)}$ by G.

When t' tends to 0, the value of $G(t')$ is equal to $\left\langle I_D^2(0)\right\rangle$ because the intensity at time t, is the same as the initial time when $t \to 0$. After a sufficiently long time (t tends to ∞), the correlation at the initial time become null. This phenomenon is the consequence of the particles Brownian motion. In this case $G(t') = \left\langle I_D(\infty)\right\rangle^2$. The constants A and B depend on the light coherence and the autocorrelation function accumulation time:

$$A = \left\langle I_D(\infty)\right\rangle^2 \text{ and } B = \left\langle I_D^2(0)\right\rangle - \left\langle I_D(\infty)\right\rangle^2 \qquad \textit{Equation I-21}$$

The constants A, B and D extracted from the autocorrelation function allow obtaining the mean radius using Stokes-Einstein equation.

E. Data treatment of the autocorrelation function

The intensity of light measured under Rayleigh conditions is the sum of all the intensities scattered by each particle present in the suspension volume studied.

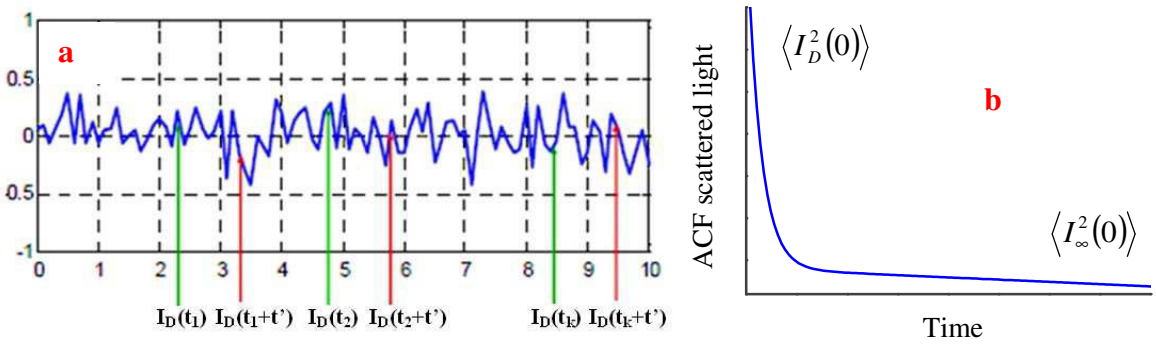

Figure I-7: The diagram showing the temporal fluctuation of the scattered intensity (a) and the intensity of autocorrelation function as a function of time (b). The time scale of the fluctuation depends on the of the particles diffusion coefficient which is inversely proportional to their radius[101].

Because of the particles random motion, the temporal evolution of the scattered intensity presents a fluctuation as shown in Figure I-7. Using a correlator, the autocorrelation function of intensity can be calculated. From a fixed value of t', the product $I_D(t) * I_D(t+t')$ is realized at each value of t. This is repeated for many values of t'.

To get the G value in photocounting regime, the experiments are needed to be carried out. To get the G value, the intensity of light diffusion is measured by photomultiplier as series of photon pulses. Between t and $(t+dt)$, the number of photons $N_{ph}(t)$ is a function of the scattered intensity value $I(t)dt$. Because of the process is Gaussian, the mean value can be obtained by integration:

$$G = \lim_{T \to \infty} \left(\frac{1}{T} \int_0^T N_{ph}(t) \cdot N_{ph}(t + t') \cdot dt \right) \qquad \textit{Equation I-22}$$

T is the accumulation time. When T increases, the precision of G values increases.

F. Experimental set-up

Nucleation and growth kinetics during hydrolysis-condensation of titanium TOA and zirconium ZOA oxo-particles have been extensively studied by Kanaev et al. team [95, 101-105]. The schematic diagram of a DLS device is shown in Figure I-8.

There are three main parts of this instrument:

i) A laser light source (20 mW, He-Ne laser spectra physics, $\lambda = 632.6\,\text{nm}$).

ii) An optical system equipped with two monomode fibers (transmitter and receiver**).**

iii) Some electronic devices such as: a photomultiplier, an amplifier, a discriminator, a digital correlator and a computer for recording and processing the data.

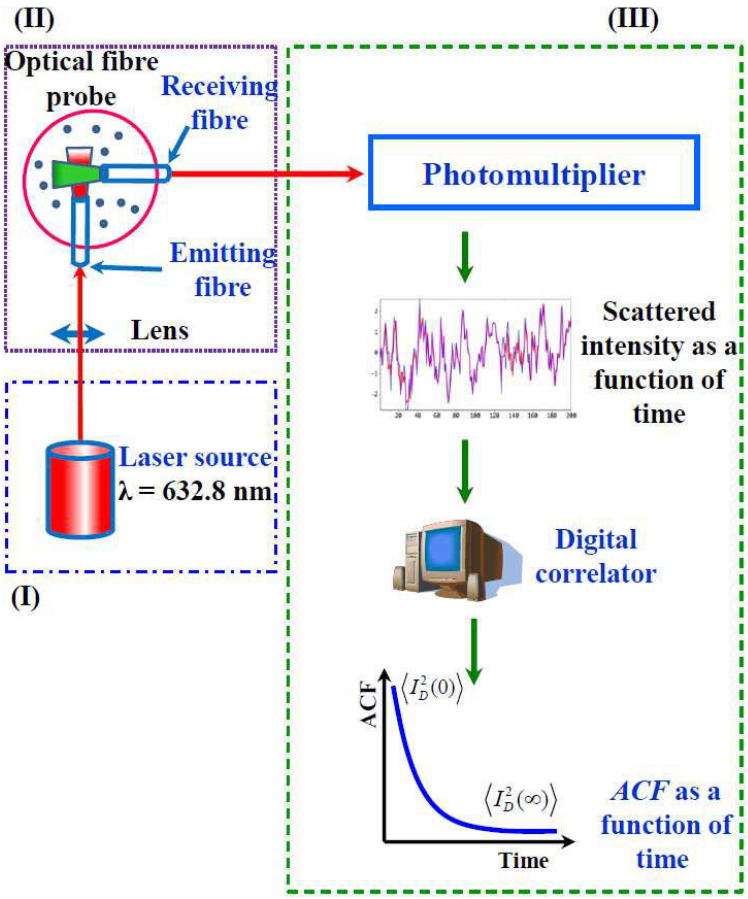

Figure I-8: Schematic diagram of the experimental device for the measurement of DLS at LSPM CNRS Villateuse [101].

Optical fiber: The incident light of the laser light source (20 mW, He-Ne laser spectra physics, $\lambda = 632.6\text{nm}$) is focalized at the observation zone in the reactor solution after the precursor(s) and water solutions are mixed. There are two fibres that are attached by glue on a probe: (1) the emission fibre probe and (2) the reception fibre probe. The observation volume, defined by a mutual positioning of two monomode optical fibres, is small enough (~10^{-6} cm^3) to avoid multiple scattering events particularly in high-concentration colloids. After precursors and water solutions are mixed, the collected experiments data with the automatic sampling mode is carried out. The short data accumulation period, took equal to 60 s permitted (i) to easy reject the non-desirable events due to rare contaminated dust particles producing strong light scattering spikes (ii) to obtain a good signal-to-noise ratio particularly from small particles. This method can be performed by in-situ measurements. Frequently, the fibre probes are calibrated with a Latex-Polystyrene particles suspended in water ($2R$ = 100 nm, Sigma Aldrich) before use.

G. Hydrodynamics radius determination

The autocorrelation curve obtained with a Latex-Polystyrene suspension is shown in Figure I-9. Using the equation $G = A + Be^{Dq^2t'}$, a non-linear less square fit allows extracting the coefficients *A*, *B* and *D*.

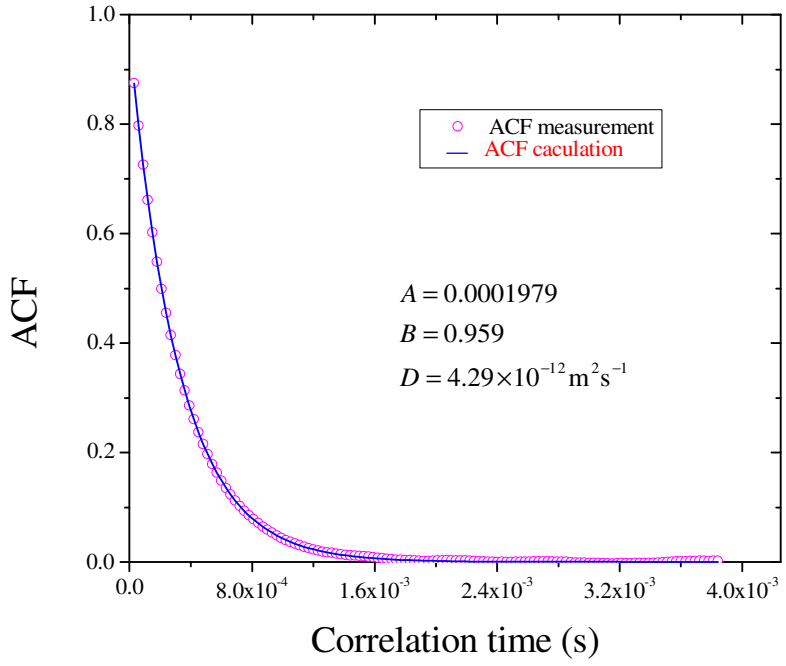

Figure I-9: Autocorrelation function of the scattering light from Latex-Polystyrene suspension in water[101].

Experimental parameters:

- Laser wavelength at 632.8 nm
- Angle of diffusion $\theta = 90°$
- Refraction index of water $n_0 = 1.33$ at 20 °C
- $Dq^2 = k$ and $q = \frac{4\pi n_0}{\lambda}\sin\left(\theta/2\right)$, so the diffusion coefficient is given by ACF function, $D = 4.29\times10^{-12} m^2 s^{-1}$

Using Stokes-Einstein equation and the value of the diffusion coefficient *D* the particles mean radius was obtained: $R = 50 \pm 1\text{nm}$.

I.3.2 Titanium dioxide (TiO_2)

I.3.2.1 Observations by Chapell

Oxo-particles of TiO_2 were prepared by Chappell et al [106] from a reaction in ethanol of 0.4 mol/L titanium(IV) tetraethoxide with 2 mol/L water in the presence of silane triol.

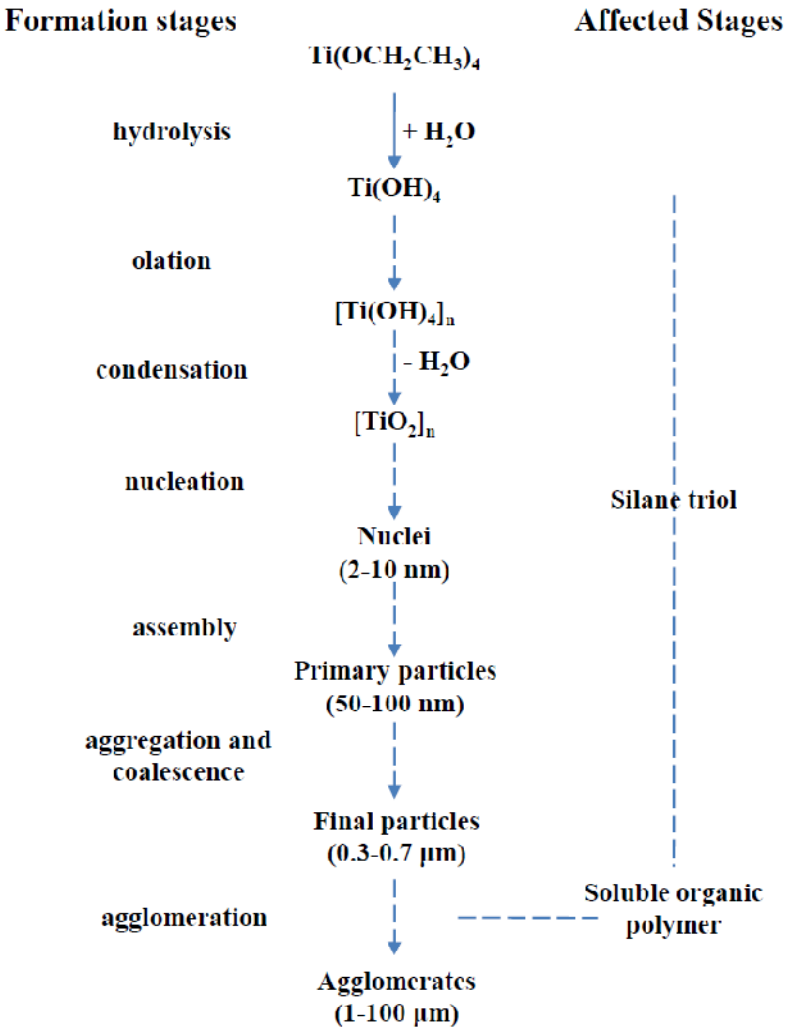

Figure I-10: Particle sizes in several stages for hydrolysis of titanium tetra-ethoxide in the presence of silane triol additive [106].

The obtained results allow highlighting a succession of growth stages after hydrolysis. These steps are appeared in the following order: a condensation polymerization which leads to the formation of nuclei (2 to 10 nm), followed by the formation of primary particles (50 to 100 nm), to finally arrive at spherical particles (0.3 to 0.7 µm). These authors showed that

the morphology of the obtained materials varies depending on the concentration of silane triol in reaction medium. The different steps of particles growth during sol-gel process are showed in Figure I-10.

I.3.2.2 Effect of critical hydrolysis ratios on particles growth kinetics

Soloviev et al [93, 94] prepared by sol gel method titanium oxo-alkoxide particles (TOA). The study of their growth kinetics during hydrolysis and polycondensation reactions was investigated. The experiments were carried out by manual mixing. In brief, solutions in isopropanol of titanium tetraisopropoxide (TTIP) precursor and water was mixed quickly. After stirring about 30 s, the colloidal suspension was transferred to a Photocor DLS device where the scattering light was measured. Figure I-11 presents the evolution of light intensity as function of time.

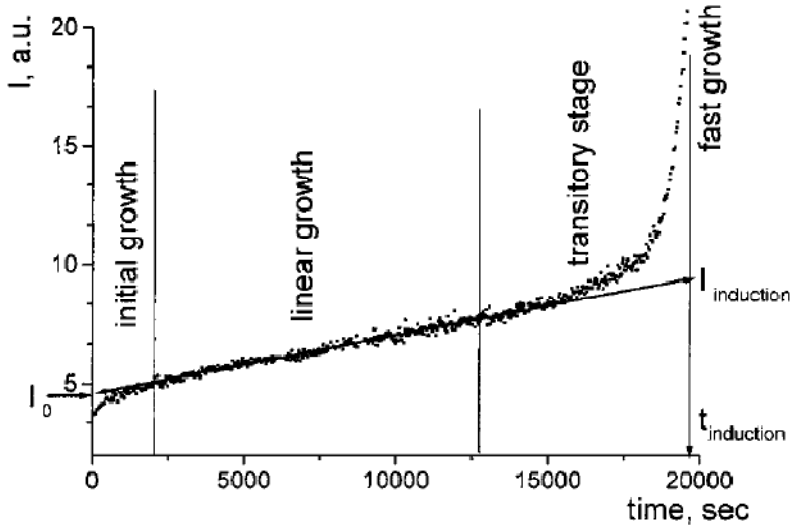

Figure I-11: Scattering intensity of sol-gel growth during induction time [94].

These studies also allow defining an induction time characteristic of the experience corresponding to an intensity of scattered light equal to five times that of origin. This choice is justified by the fact that the increase of light intensity diffused by the suspension is so rapid during precipitation that the difference between $5I_0$ and $10I_0$ represents only a small part of the induction period. In this case, the induction time is defined by Soloviev et al [94] as the moment of the change in growth mechanism, from slow kinetics to rapid kinetics, as shown in Figure I-11.

Four stages could be distinguished in the above graph: initial growth, linear growth, transitory and fast growth stages. The kinetics of particle sizes evolution of this reaction

strongly depends on concentrations of TTIP and water. The kinetics rate proposed by these authors is as the following:

$$r_{ind} = k \cdot C_{Ti}^{\alpha} \cdot C_{H_2O}^{\beta} = k \cdot C_{Ti}^{\alpha+\beta} \cdot H^{\beta} \qquad \textit{Equation I-23}$$

Where r_{ind}, $C_{Ti,}$ C_{H_2O}, k and H $(H = \frac{C_{H_2O}}{C_{Ti}})$ are respectively kinetics rate, precursor concentration, water concentration, rate constant and hydrolysis ratio. a and β are the reactions order.

In order to take into account the fact that the initial hydrolysis reaction is much faster than whole induction period, the equation I-23 is needed to be modified by introducing the critical hydrolysis ration h*.

$$r_{ind} = k \cdot C_{Ti}^{\alpha}(C_{H_2O} - C_{Ti} \cdot h^*)^{\beta} = k \cdot C_{Ti}^{\alpha+\beta} \cdot (H - h^*)^{\beta} \qquad \textit{Equation I-24}$$

The hydrolysis ratio h* (particular value of the hydrolysis rate H) is the ratio between the molar concentration of the water consumed during the initial hydrolysis $C_{H_2O}^0$ and the concentration of TTIP $h^* = C_{H_2O}^0 / C_{Ti}$. The introduction of h^* allows to explain the appearance or not of a precipitate. Indeed, the precipitation can effectively appear, provided that "clusters" are initially formed after a certain number of condensations represented by a critical ratio h^*. The authors found that precipitation occurred after a finite induction time if $H \geq h^*$ in the opposite case $H \leq h^*$, no precipitate is observed. After fitting the data by equation I-23 and equation I-24, the critical hydrolysis ratio was found equal to $h^* = 1.4 \pm 0.1$.

I.3.2.3 Oxo-TiO_2 particles prepared by micromixing sol gel reactor

Revallin et al [107, 108] investigated the nucleation and growth kinetics of TOA particles in isopropanol, after TTIP precursor was hydrolyzed with different hydrolysis ratios. Precursor and water solutions were mixed by a sol-gel micromixing reactor. The results revealed that the evolutions of particle sizes and induction times were highly reproducible. The reproducibility is less than 10% $\left(\Delta t_{ind} / t_{ind} < 10\%\right)$. The evolution of particle sizes and light intensity as function of time is shown in Figure I-12.

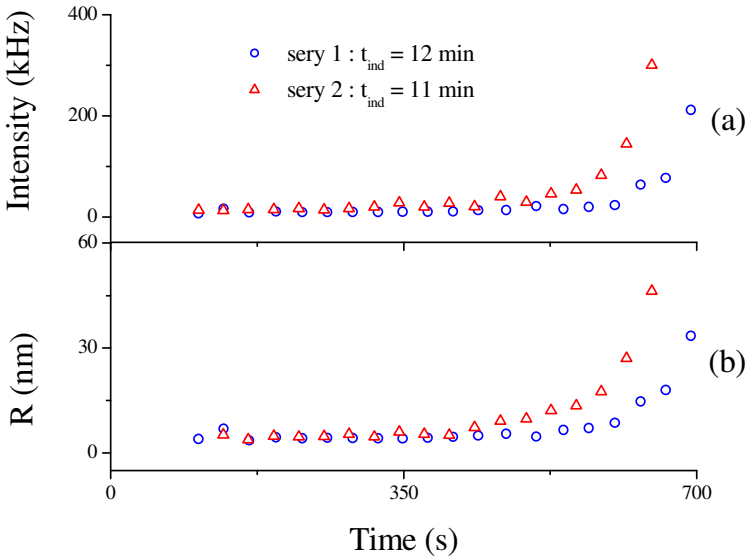

Figure I-12: The evolution of scattered light intensity and TOA particle sizes versus time in micromixing reactor [108], (experimental condition: concentration of precursor TTIP = 0.146 mol/L, hydrolysis ratio H = 2.74, solvent isopropanol, T= 20°C).

The kinetics of oxo-TiO_2 (TOA) particles precipitation in sol-gel obtained in micromixing reactor were investigated with various temperature [95]. The observation was carried out at induction stage in the temperature range 5-40 °C using 0.146 mol/L of TTIP and a hydrolysis ratio H = 2.46. The evolution of TOA particle sizes with temperature was found to be thermally activated with an activated energy equal to $E_a = 0.33 \pm 0.02$ eV . This energy was assigned to hydrolysis reaction of the groups Ti-OPr^i on the surface. Using the formular $I(t) \infty R^{D_f}$ (see equation I-9) the authors fitted the evolutions of the particle sizes with light scattering intensity and obtained the value of fractal dimension D_f which decreased from 1.5 to 1 when the temperature was increased from 5 to 35 °C.

I.3.2.4 Influence of the injection fluid hydrodynamics on particle size

Azouani et al [102, 109, 110] investigated the effect of Reynolds numbers of the injection fluid in T-mixer on the particles size distributions. Experiences were realized by varying the applied injection pressure. The profile of fluids flow in T-mixer and the particles size distributions at different *Re* is presented in Figure I-13(**i**).

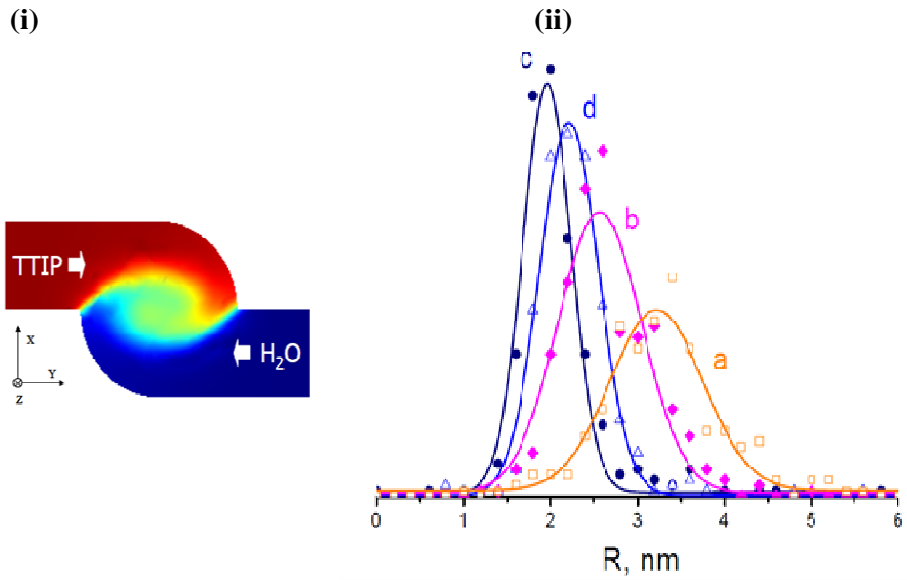

Figure I-13: ***(i)*** *Representative scheme of the turbulent fluid flow injection in T-mixer at mixing zone point and* ***(ii)*** *Distributions of TOA particle sizes corresponding to the mixing fluid Reynolds number Re equal to* 2×10^3 *(a),* 3×10^3 *(b),* 6×10^3 *(c),* 8×10^3 *(d) (TTIP = 0.146 mol/L, H =1.9 and T = 20 °C)[110].*

Large particle size distributions are obtained with small *Re* = 2×10^3 and 3×10^3. For very high *Re* value 8×10^3, the distribution is narrow but the reproducibility is low. The cavitations phenomenal appeared at the critical *Re** = 8×10^3 [111], which imposes a limit on reactive systems using the turbulent micromixing method. The optimum condition was obtained with *Re* = 6×10^3.

I.3.2.5 Hierarchical growth of oxo-alkoxide particles

Using micromixing sol gel reactor, Azouani et al [102] reported a study concerning the effect of hydrolysis ratio on the particle sizes change. The evolution of initial particle sizes as function of hydrolysis ratios is given in Figure I-14, which can be divided in four domains.

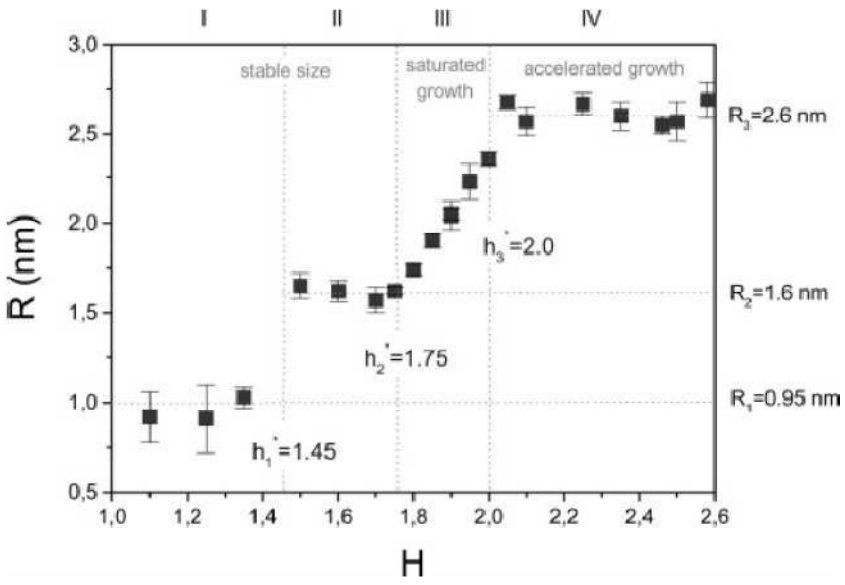

Figure I-14: Particle sizes of TOA at different hydrolysis ratios(TTIP= 0.146 mol/L, T = 20 °C) [102].

Four domains can be observed:

Domain I and II (H ≤ 1.75): In domain I, the particle sizes were stable during 24 h with $R = 0.95 \pm 0.1\,\text{nm}$. When H increases (domain II), particles grow and $R = 1.60 \pm 0.01\,\text{nm}$.

Domain III (1.75 < H ≤ 2.0): As shown in Figure I-14, the size of particles increases; a maximum limit size was obtained after approximately ten minutes. This domain corresponds to period called "growth limitation". The particle size at saturation depends on the hydrolysis ratio H: the higher the concentration of H_2O in the medium, the greater the formation of large units. When the size of the clusters attained the limit, they remain stable for a long time (> 24 hours).

Domain IV (H > 2): In this domain, the global kinetics of nucleation-growth has 2 stages. During the first step, particles of size around R~2.6 nm are obtained. This first step is associated with the rapid and accelerated growth process due to condensations of particles. The second step, not shown, concerns the agglomeration of the precipitating particles.

I.3.2.6 Doped oxo-TiO_2 nanoparticles

A. Cationic doping: Fe-TiO_2 nanoparticles

Siteng et al [101, 104] reported a study on the nucleation and growth process of particles oxo-TiO_2 doped with iron acetylacetonate ($Fe(acac)_3$). Doped oxo-particles were prepared from the mixture of TTIP/isopropanol and $Fe(acac)_3$/water/isopropanol solutions.

They observed that $Fe(acac)_3$ significantly reduces the rate of doped oxo-particles growth (r_{ind}). Its influence can be illustrated in Figure I-15.

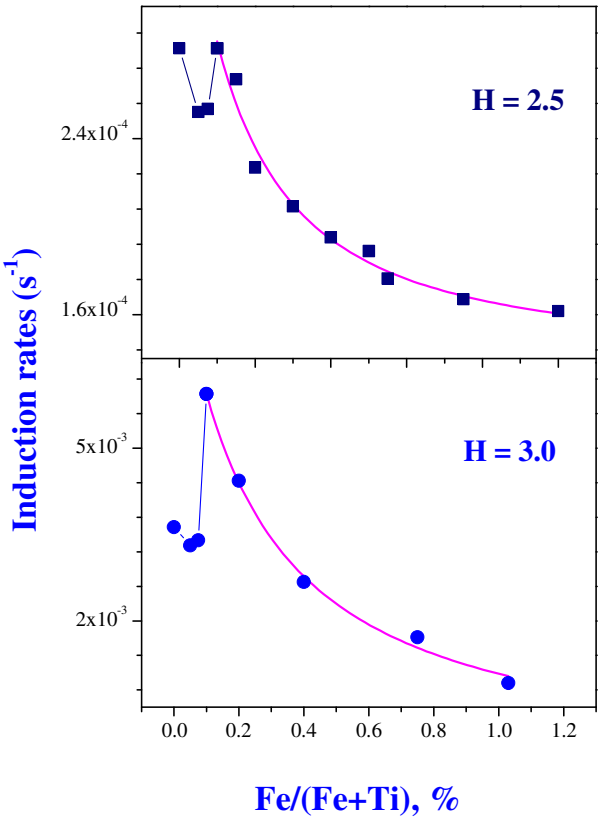

Figure I-15: Induction rate of iron doped titanium oxo-particles (C_{Ti} = 0.146 mol/L, T = 20 °C, H = 2 and 3 and Re = 4500) [104].

The observed reduction of the induction rate is explained by the formation of large particles on which the surface groups acac slow down the rate of hydrolysis and condensation. Even thought the iron doping affects notably the induction rates, doped oxo-particles sizes were not significantly different from pure TOA. Figure I-16 presents the initial radius of iron doped TOA particles versus doping ratio.

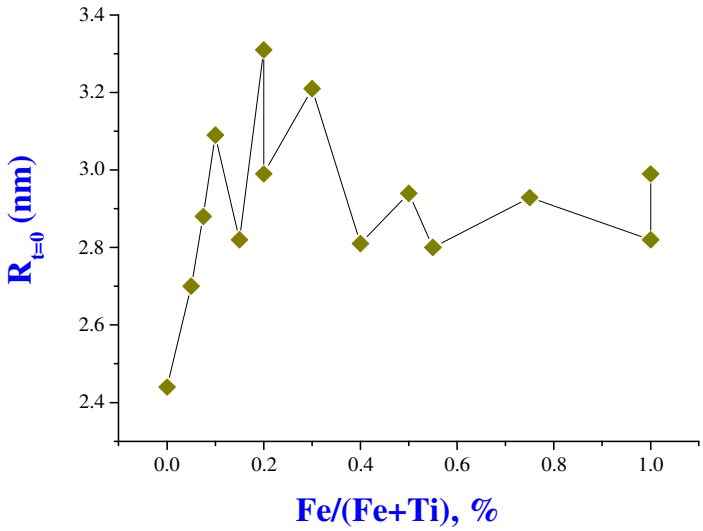

Figure I-16: Initial particle sizes of iron doped TOA nanoparticles versus doping ratios (C_{Ti} = 0.146 mol/L, H = 2.5, Re = 4500) [101].

B. Anionic doping: N-TiO_2 nanoparticles

Azouani et al [103] have reported TOA anionic doping by hydroxyurea and monodispersed particles were obtained. Different from iron doping, this doping accelerates kinetics rate in both nucleus and aggregation stages. The N-doping at the nucleation stage of oxo-alkoxy nanoparticles was found very effective. In contrast, it has been observed that N easily leaves the solids during heating at temperatures close to those required for the anatase phase crystallization. A major problem of the N-doped photocatalyst preparation by the proposed method is therefore related to N atoms retention at the heat treatment stage.

I.3.3 Zirconium dioxide (ZrO_2)

Zirconium element is in the same group as titanium element and their alkoxides have four ligands –OR groups. The preparation of zirconium oxo-alkoxide nanoparticles (ZOA) in alcohol in a micromixing sol-gel reactor was carried out by Siteng et al. [112] and Sana et al. [105, 113]. Study on the nucleation and growth process of these oxo-particles was firstly performed by Siteng et al. [112]. It was confirmed that particles sizes are monodisperse and equal to 4.7 nm diameter and the growth behavior is similar to that of titanium oxo-particles.

More detailed studies were reported by Sana et al. [105, 113]. These authors investigated the effect of both precursors and solvents on the particles growth and proposed a model.

Solvent effect on ZOA particle sizes [105, 113]

Several experiments were carried out in a micromixing sol-gel reactor using zirconium n-butoxide and zirconium n-propoxide as precursors, and ethanol, n-propanol, 2-propanol and n-butanol as solvent. These authors found that ZOA oxo-particles are stable and monodisperse with small sizes when zirconium n-propoxide and n-propanol were used. The characteristic of the autocorrelation functions (ACF) in different couples solvents-precursors are shown in Figure I-17.

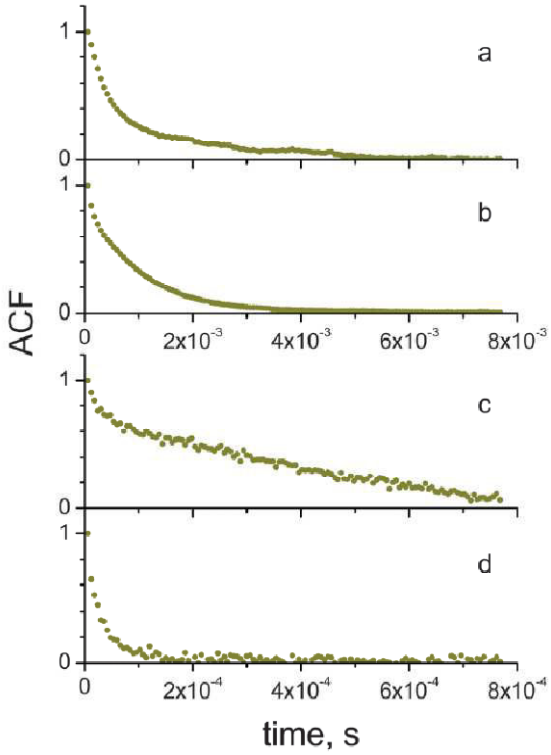

Figure I-17: ACFs of ZOA particles in the different precursors–solvent pairs: zirconium n-butoxide in n-butanol (a), zirconium n-butoxide in 2-propanol (b), zirconium n-butoxide in ethanol (c) and zirconium n-propoixde in n-propanol (d) (C_{Zr} = 0.15 mol/L, T = 20 °C) [105].

The size of ZOA particles prepared from zirconium(IV) propoxide in n-propanol obtained in the large range of precursor concentration and hydrolysis ratios is equal to R = 1.8 nm. This is significantly smaller than that of titanium oxo-particles TOA (R = 2.6 nm ,

H > 2). However, the induction time of particle growth depended on the concentrations of precursors and water. The evolution of rate and sizes respectively obtained from DLS versus hydrolysis ratios are shown in Figure I-18. TEM photograph of ZrO_2 powder showing the presence of particles around 1.8 nm is given in Figure I-19.

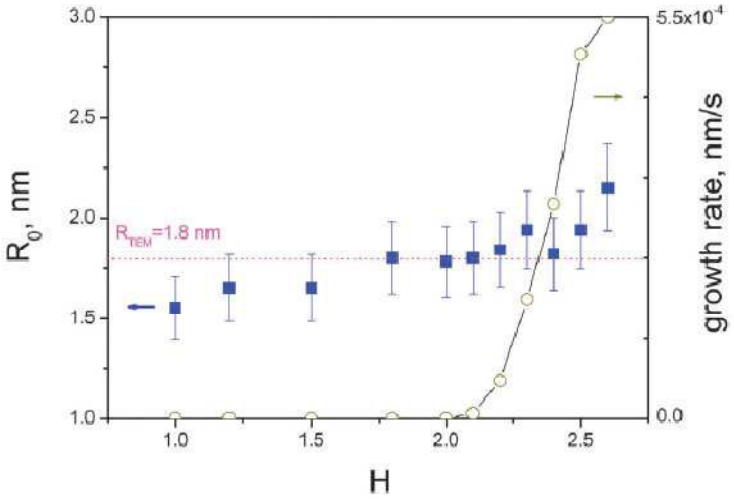

Figure I-18: Initial sizes of particle (R_0) and slope of I(t) curves during the induction period of ZOA n-propanol sol–gel process for different hydrolysis ratios (C_{Zr} = 0.15 mol/L, T = 20 °C) [105].

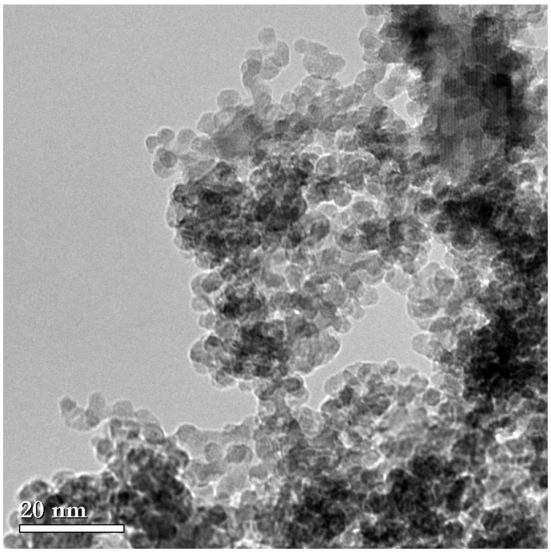

Figure I-19: TEM Image of ZOA nanoparticles obtained in the following experimental condition: C_{Zr} = 0.15 mol/L, H = 2.5, T = 20 °C [105].

Kinetics of sol-gel particles growth

According to hydrolysis ratios, there are two domains of particles growth:

Domain H ≤ 2: Monodisperse nanoparticles appeared in the millisecond timescales and were very stable (longer than 24 hours) with R = 1.8 nm.

Domain H > 2: Particles grow quickly with some aggregations after the injection. The fractal dimensions are close to 1 e.g $D_f = 1.05 \pm 0.4$ and 1.35 ± 0.2 for H = 2.1 and 2.3 respectively.

Critical hydrolysis ratios

The authors proposed the kinetics model similar to that of TOA nanoparticles [94, 95, 108] that can be expressed as:

$$r_{ind} = kC_{Zr}^{\alpha}(C_{H_2O} - C_{H_2O}^{0})^{\beta} = kC_{Zr}^{\alpha+\beta}(H - h^{*})^{\beta} \qquad \textit{Equation I-25}$$

Where r_{ind}, k, C_{Zr}, C_{H_2O}, H and h^* are rate at induction stage, rate constant, zirconium precursor concentration, water concentration, hydrolysis ratios and critical hydrolysis ratios respectively. α and β are order reactions.

From linear plotting presented in Figure I-20, two values of critical hydrolysis ratio h^* = 1.5 and 2.0 can be proposed: (i) for h^* = 1.5, the value of β = 6.6 and α value became negative after deriving. Therefore, it was rejected. (ii) For h^* = 2.0, the value of β = 2.4 and after deriving α = 3.9. This last value, largely higher that found for titanium oxo-particle α = 1, cannot be retained, in so far as the two models are similar. To apply the same model the authors proposed the critical $h^* \approx 1.7$ [105].

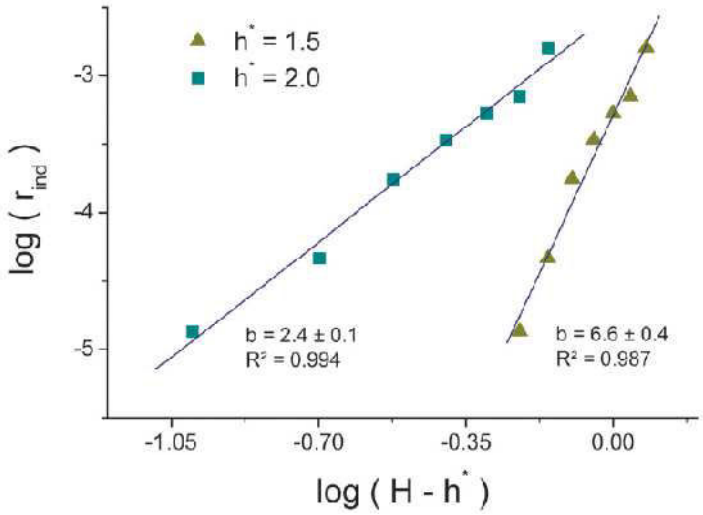

Figure I-20: The induction rate depends on the hydrolysis ratios at the critical hydrolysis ratios h = 1.5 and 2.0 (C_{Zr} = 0.15 mol/L, T = 20 °C) [105].*

I.4 Sol-gel reactor with ultrarapid micromixing

The micro-mixing reactor set up was described in the refs [108, 110, 114]. Figure II-21 shows the schematic diagram of micromixing sol-gel reactor used in LSPM CNRS Villetaneuse.

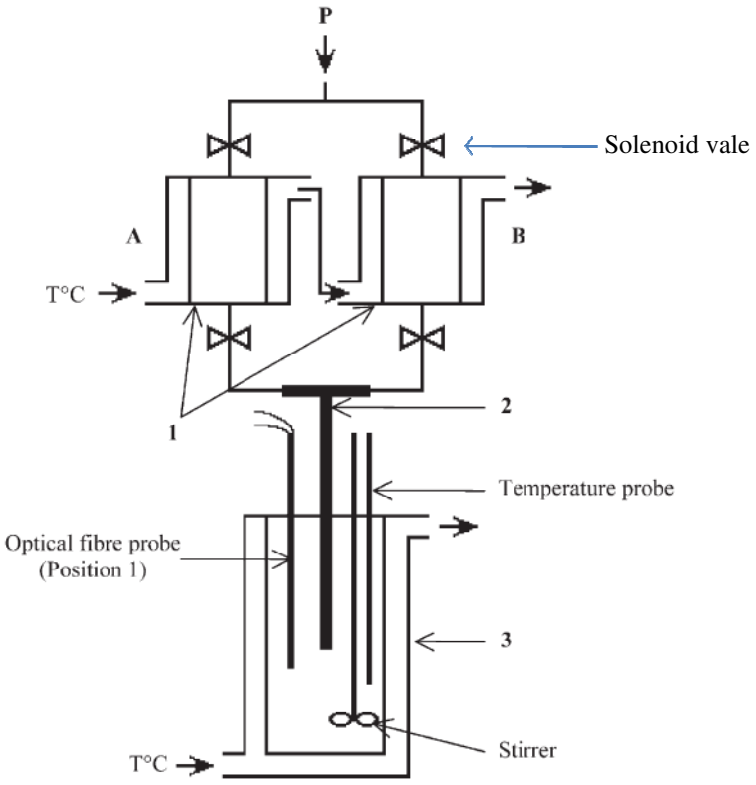

Figure I-21: Representative diagram of the microreactor developed by Rivallin [108] (A) precursors and (B) water (reactor tanks (1), T-mixer (2) and thermostatic reactor (3)).

The main parts of this microreactor are:

Reactor tanks for stock solutions: There are two thermostated stock solutions of volume 100 mL: (A) contains precursor(s) solution and (B) water solution.

Applied pressure gas and vales:

Nitrogen gas bottle containing water less than 5 ppm is connected with tubes to the thermostatic stock solutions, (A) and (B). The solenoid vales are used to control the period of applied gas pressure into the reactor tanks. The pressure from the bottle can be adjusted or changed in different Reynolds numbers to get the best populations of the desired results or monodisperse particle sizes.

T-mixer: It is the main part of mixed precursors and water in solvent. T-mixer was made of two arms with initial diameter of 1 mm and one exit leg diameter of 2 mm with length of 200 mm as shown in Figure I-22.

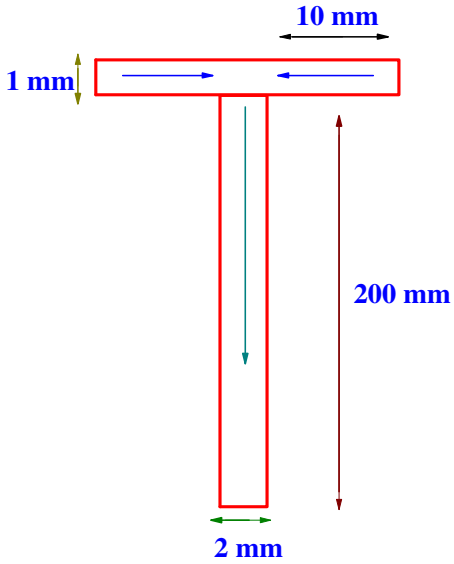

Figure I-22: Schematic diagram of T-mixer [115].

Double-walled cylindrical glass: This is the place of keeping colloids after precursor and water solutions are mixed in T-mixer. A fibre optical probe is introduced into this tank for particle sizes measurement.

The temperature of the whole system (double-walled glass, tanks (A) and (B) is controlled by a thermo-cryostat (Haake, DC10K15).

I.5 Optical properties and applications

I.5.1 Band gaps of TiO_2, ZrO_2 and of ZrO_2-TiO_2 composite

According to their band gap energy (E_g), metal oxides can be conductors, semiconductors or isolators. Band gap energy is the important factors to be considered for photocatalytic study. There are few papers that reported on band gaps of ZrO_2-TiO_2 composite which depended on the method preparations. Some values of E_g were compared in table I-3.

Table I-3: Band gaps of ZrO_2-TiO_2 as function of ZrO_2 content. Those of TiO_2 and ZrO_2 were given for comparison.

Band gaps (eV)					
TiO_2	ZrO_2	ZrO_2-TiO_2	ZrO_2 content (%)	Methods	refs
3.23	-	3.23 to 3.32	0 to15	Modified sol-gel	[88]
3.39	5.15	between TiO_2 and ZrO_2	0 to100	Sol-gel	[116]
3.25	5.26	—‖—	—‖—	—‖—	[48]
3.2	7.8	—‖—	—‖—	—‖—	[117]
3.17	-	3.17 to 3.45	0 to50	templating sol-gel route	[118]
-	5.0	3.4	90	Sol-gel	[49]
-	-	3.65	50	—‖—	[119]
3.19	-	3.19 to 3.38	0 to 30	—‖—	[120]

From these data, it can be noted that TiO_2 band gaps are not much different regardless the preparation methods. However, E_g of ZrO_2 and ZrO_2-TiO_2 composite are significantly dependent on the preparation method and the compositions of starting oxides (ZrO_2 or TiO_2) for the binaries oxides.

I.5.2 Photocatalytic properties of titanium dioxide (TiO_2)

TiO_2 can be used as photocatalytic material to decompose pollutants of volatile organic compounds (VOC) such as alkane, alkene, alcohol, aromatic, organic acids etc [101] as well as inorganic gas pollutants e.g. H_2S, CO, SO_x and NO_x [121]. For water treatment, it is very useful to photodegrade pollutants especially organic wastes [2, 122].

When a semiconductor material, such as TiO_2, absorbs light, the electron valences (e^-) are excited from the valance band (V.B.) by creating a hole (h^+) to conduction band (C.B.). These photogenerated charges (e^-/h^+) can recombine or participate in photocatalytic processes. It is known photocatalytic materials such as TiO_2 have longer electron-hole lifetime.

(1) $TiO_2 + h\nu \rightarrow TiO_2(h^+_{V.B.} - e^-_{C.B.})$

At conduction band, electron reduces O_2 in the medium to form $O_2^- \bullet$.

(2) $O_2 + e^- \rightarrow O_2^- \bullet$

The hole (h^+) at valance band can react with water molecule to form $HO\bullet$ and H^+.

(3) $H_2O + h^+ \rightarrow OH\bullet + H^+$

These species are able to decompose organic pollutants. The general reactions occurring during photocatalytic process are shown in Figure I-23.

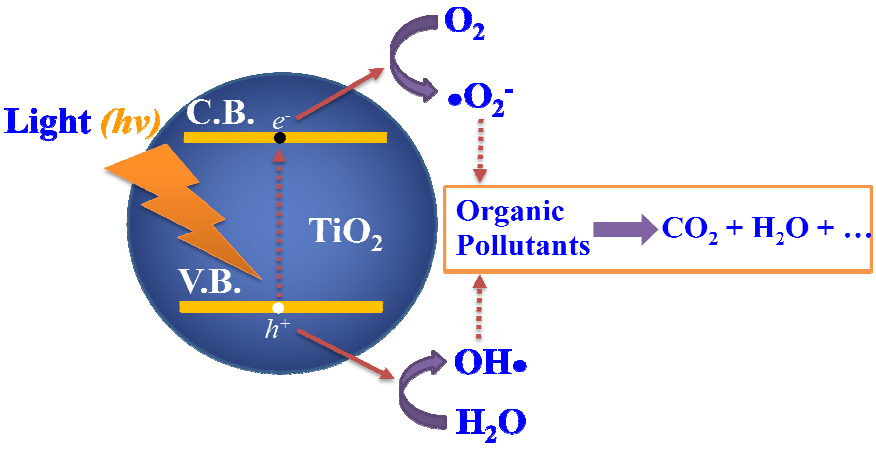

Figure I-23: General mechanism photodegradation using TiO_2 catalysts.

Other reactions that occur during the photocatlytic process were summarized by Siteng et al. [101].

(4) $O_2^- \bullet + H^+ \rightarrow HO_2 \bullet$

(5) $HO_2 \bullet + HO_2 \bullet \rightarrow H_2O_2 + O_2$

(6) $H_2O_2 + O_2^- \bullet \rightarrow OH \bullet + OH^-$

(7) $H_2O_2 + hv \rightarrow 2OH \bullet$

(8) $h^+ + OH^- \rightarrow OH \bullet$

I.5.3 Photocatalytic properties of zirconium dioxide (ZrO_2)

ZrO_2 can also be used as photocatalytic materials, but the publications involved are much more abundant than for TiO_2. It was reported that it could be used to decompose hexane and methanol and even more active than P25-TiO2 in case of amorphous material [123]. This high activity came from the abundant hydroxide groups on its surface.

Karunakaran et al [124] reported on the photocatalytic activity of ZrO_2, TiO_2, ZnO, Fe_2O_3, V_2O_5, CdO, CdS and Al_2O_3 to photooxidize aniline to azobenzene in ethanol. The photocatalyst were irradiated at λ = 254, 365 nm and sunlight. These authors found that ZrO_2 was more active than others oxides when the wavelength λ = 254 nm was applied. However, V_2O_5 and ZnO oxides illuminated with λ = 365 nm were more active. Using sunlight illumination, V_2O_5, ZnO, Fe_2O_3, CdO have shown better results. This photocatalytic activity of ZrO_2 was explained by the presence in this material of defects of formed by oxygen vacancies. Kumar et al [125] reported that the presence of defects in this material improved photocatlytic activity for methylene blue photodegradation. The material

was active even though the wavelength of 365 nm was used, which photons energy is below the material band gap equal to 5.1 and 4.8 eV respectively after calcinations at 500 and 700 °C. As mentioned above, the authors explained that oxygen vacancies were responsible for the activity of this photodegradation. The proposed mechanism for this photodegradation is in Figure I-24.

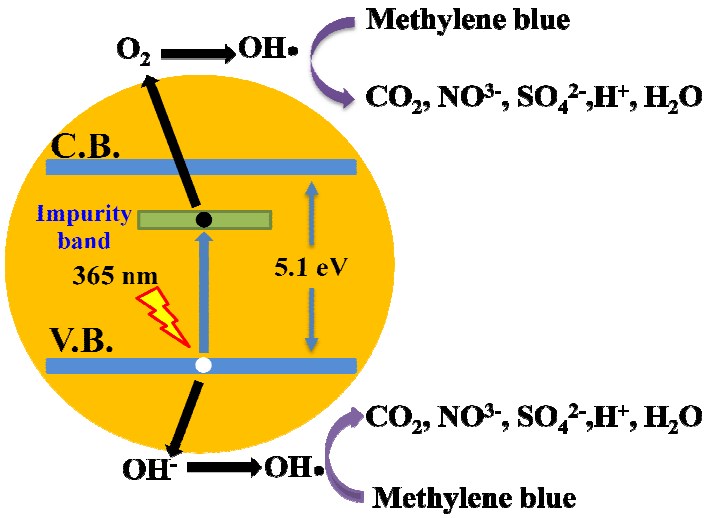

Figure I-24: The proposed mechanism of methylene blue photodegradation by ZrO_2 [125].

Renuka et al [126] reported a photocatalytic study of ZrO_2 obtained by sol-gel process (SGR) and solution combustion method (SCR). The samples band gaps energy E_g were 4.8 and 5.1 eV respectively for sol-gel and solution combustion methods [126]. They explained that the defect formed oxygen vacancies caused E_g of ZrO_2 (SGR) lower than that of solid obtained by SCR methods and improved the photocalytic activity to decompose methylene blue from 63% for ZrO_2 (SCR) to 97 % for ZrO_2 (SGR).

I.5.4 Photocatalytic properties of composite ZrO_2-TiO_2

Even though TiO_2 has been known and used in past decades as photocatalysts for environmental purification due to low cost, safety and long time stability [127], the improved photocatalytic activities by mixed photocatalyst with other oxides or doped by some foreign metal ions have been interested so far [13]. For this objective, ZrO_2 is one of the popular oxides to be mixed with TiO_2 [13].

The use of ZrO_2-TiO_2 composite for photocatalytic applications has significant advantages. Materials with less zirconium contents than 10% have an improved activity: E.g 5.7% [88], 9% [72], 10% [67], 7.7 % [57] etc. However, some materials with higher

zirconia contents were reported 30% [66], 39% [74]. For composite with high zirconia content, the light having lower wavelengths was frequently used.

Table I-4 witnesses a large discrepancy in the optimal elemental composition of the photocatalyst, varied from 5.7 % to 50 %, which apparently reflects the material inhomogeneity at nanoscale. This case is similar to that earlier widely discussed in the literature concerning iron doped titania [128], where iron clustering resulted in overestimation of the optimal doping. It has been largely recognised in previous studies that inhomogeneity of the elemental repartition serves to be an obstacle in reproducibility of the material functional response. The homogeneity remains one of principal issues in the research on the mixed oxide TiO_2-ZrO_2 photocatalyst not yet explicitly documented in the scientific literature. This homogeneity is closely related to the chemicals mixing quality during the elaboration process that can be represented by the Damköhler number: $Da=t_{mix}/t_{nucl}$, where t_{mix} and t_{nucl} are respectively times of the physical mixing and solid nucleation processes. By consequence, for the best material homogeneity in a chemical engineering process one needs to satisfy $Da \leq 1$ [129].

Table I-4: ZrO_2-TiO_2 photocatalysis.

Synthesis	Optimal composition Zr/(Zr+Ti)	Homogeneity	Photocatalysis	Pollutant	Ref.
sol-gel	0.12	not confirmed	gas-phase	Ethylene	[130]
polymer gel templating	0.10	- ‖ -	liquid-phase	salicylic acid, 2-chlorophenol	[67]
sol-gel	$TiO_2/Zr_{0.5}Ti_{0.5}O_2$	- ‖ -	- ‖ -	methyl orange	[131]
sol-gel	≤0.10	inhomogeneous	- ‖ -	trichloroethylene	[54]
mech. mixing	0.05 - 0.10	- ‖ -	gas-phase	ethanol	[132]
ultrasonic spray pyrolysis	0.09	not confirmed	liquid-phase	rhodamine B	[72]
solvothermal, ACF templating	0.197	- ‖ -	gas-phase	ethylene, trichloromethane	[133]
EISA	0.20	- ‖ -	liquid-phase	rhodamine B	[134]
PCMS	0.09	- ‖ -	gas-phase	NO_X	[51]
Zr-incorporated TiO_2	0.14	- ‖ -	liquid-phase	rhodamine B	[135]
co-precipitation	0.075	- ‖ -	- ‖ -	acetone	[136]
colloids mixing	0.39	inhomogeneous	- ‖ -	phenol	[74]
sol-gel	0.08	not confirmed	gas-phase	formaldehyde	[137]
colloids mixing	0.44	inhomogeneous	liquid-phase	methylene blue	[138]
surfactant self-	0.069	not confirmed	- ‖ -	rhodamine B	[68]

assembly					
Sol-gel	0.057	not confirmed	- ‖-	azo-dye Ponceau BS	[88]

Generally, the factors that were considered to improve photocatalytic activity in UV domain of binary oxide nanoparticles ZrO_2-TiO_2 over pure ZrO_2 and TiO_2 are: high surface area, high content of TiO_2 anatase and ZrO_2 monoclinic phase, presence of OH surface groups [74], small particle size [51, 74], strong adsorption in the ultraviolet region[139], band gap and low electron-hole recombination [140].

The mechanism describing the photocatalytic activity of this composite was firstly reported by Fu et al.[130]. More detail of this mechanism can be found in refs [57, 74, 88]. Many authors seem to agree with the fact that there exist the C.B. surface trap states of ZrO_2 which lie below the C.B. edge of pure TiO_2. So the easy transfer of the photo-generated electrons from ZrO_2 to the conduction band of TiO_2 can take place. This process may prevent the recombination of the electron and hole, allowing ZrO_2–TiO_2 composite to acquire a high photocatalytic activity. Schematic diagram of electron transfer is illustrated in the Figure I-25.

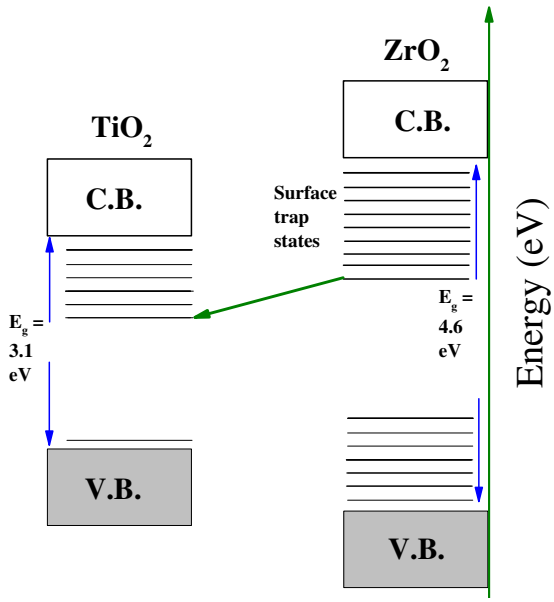

Figure I-25: The diagram of electron in surface trap states of ZrO_2 conduction band crossed section into TiO_2 conduction band [57].

Influence defect of $Zr_xTi_{1-x}O_2$ on photocatalytic activity

Photocatalytic reactions proposed by Yu et al are as the following [136]:

(1) $Zr_xTi_{1-x}O_2 + h\nu \leftrightarrow h^+ + e^-$

(2) $OH^-_{(ads)} + h^+ \rightarrow OH\bullet$

(3) $O_{2(ads)} + e^- \rightarrow \bullet O^-_{2(ads)}$

(4) $O^{2-}_L + h^+ \rightarrow O^-$

(5) $O^- + h^+ \rightarrow O$

(6) $O^-_{ads} + h^+ \rightarrow O$

(7) O^- (and $O^-_{(ads)} + H_2O_{(ads)} \rightarrow OH\bullet_{(ads)} + OH^-_{(ads)}$

(ads) symbol: A specie adsorbed on the surface of catalyst

O^{2-}_L: The escaped oxygen species from the surface of catalyst

According to these authors, reactions (4)-(7) does not take place in case of pure TiO_2, because this material has low defects compared to composite $Zr_xTi_{1-x}O_2$.

I.5.5 Applications

Because of its high refractive index and UV light absorption, titanium dioxide is very effective in many areas of applications, including photocatalysis, use as pigment in the paint, food coloring, personal care and other products [141, 142]. In the area of photocatalytic applications, it is used as self-cleaning surface, water purification, air purification, self-sterilizing surfaces, anti-fogging surfaces, environmental friendly surface treatment, photocatalytic lithography etc [2, 101, 122]. Unlike TiO_2, ZrO_2 and ZrO_2-TiO_2 composite have not yet been used for industrial applications. Principal Fields of TiO_2 photocatalytic applications are shown in Figure I-26.

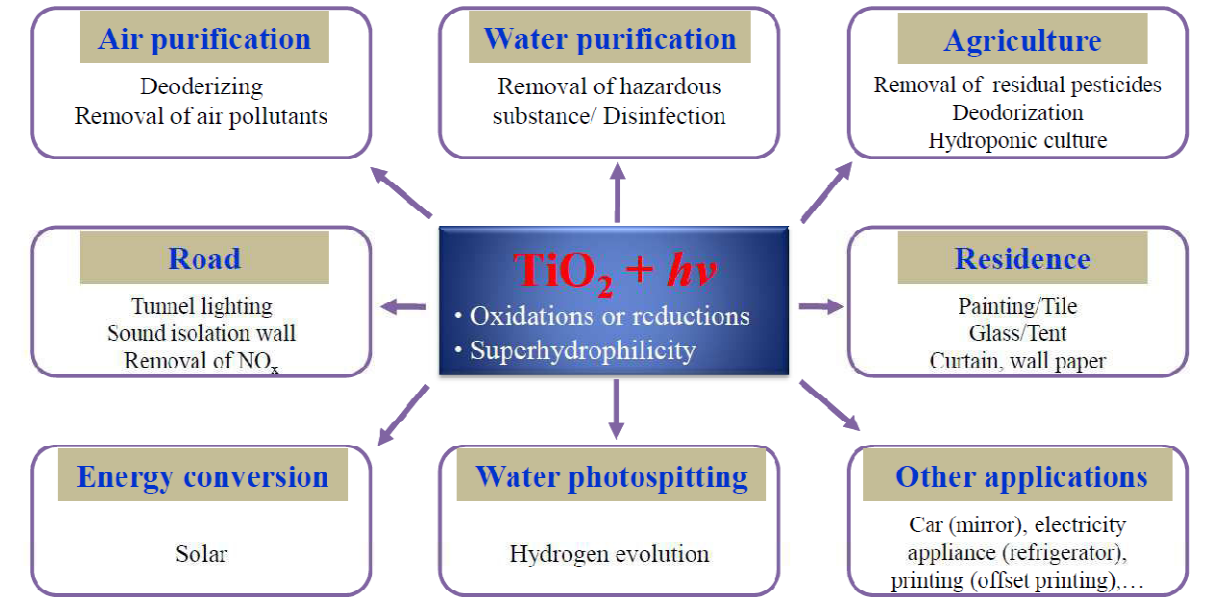

Figure I-26: Principal applications of TiO_2 [143].

I.6 Conclusion

This literature review starts from the presentation of the main crystallographic structure of titanium dioxide TiO_2 and zirconium dioxide ZrO_2. It is followed by a description of structural properties of ZrO_2-TiO_2 composite with an emphasis on the dependence of the structural and thermal properties on ZrO_2 content. Many controversies exist about the reported results. This change was explained by the homogeneity level of starting mixed oxides and the preparation method. The next paragraph focused on the work of the predecessors in the laboratory related to the nucleation and growth process of Titanium oxo-particles (TOA), Zirconium oxo-particles (ZOA). The micromixing of the reagents is an essential parameter for obtaining monodisperse particles. To obtain these results, Rivallin et al developed a sol-gel precipitation reactor to control micromixture, temperature and humidity. The implementation of this reactor allowed Azouani et al to show that the particles resulting from the hydrolysis of TTIP alkoxide undergo a hierarchical growth as a function of the H_2O concentration. Moreover, these authors have found that the hydrodynamics of mixture fluid significantly influent on the distribution of particle size formed in sol-gel reactor. This paragraph ends with a study on the process of nucleation and growth of ZrO_2 particles in several pairs alkoxide-solvent. These authors revealed that

zirconium oxo-particles are monodisperse, their size is stable and smaller than that observed for titanium oxo-particles in the same hydrolysis ratio H > 2.

The last paragraph was devoted to optical properties of TiO_2, ZrO_2 and ZrO_2-TiO_2 composite. Photocatalytic process of TiO_2 was briefly presented and a number of examples related to environmental applications of photocatalysis were shown. For ZrO_2, several authors explained that the presence of the defects formed by oxygen vacancies improved the phocatalytic activity of this material. A mechanism, taking into account the involvement of defects was proposed. Finally, the high photoactivity of ZrO_2-TiO_2 composite was explained by the existence of C.B. surface trap states of ZrO_2 below the C.B. edge of pure TiO_2. Consequently, the photo-generated electrons can transfer from C.B. (ZrO_2) to C.B. (TiO_2), thus preventing the electron-hole recombination.

Notations

n_{Zr}	molar of zirconium (mol)
n_{Ti}	molar of titanium (mol)
C_{Ti}	titanium concentration (mol/L)
C_{Zr}	zirconium concentration (mol/L)
C_{H_2O}	water concentration (mol/L)
n_{Zr+Ti}	molar of mixed zirconium and titanium (mol)
T	temperature (°C or K)
Ts	transition temperature (°C)
E_g	band gap energy (eV)
eV	electron volt (energy of band gaps)
$h\upsilon$	applied energy
V.B.	valence band
C.B.	conduction band
VOC	volatile organic compound
Re	Reynolds numbers
D_f	fractal dimension
M	total mass
m	mass of particle
N_i	number of particles
TTIP	titanium tetraisopropoxide
-OPr^i	isopropoxide
TOA	titanium oxo-alkoxide
ZOA	zirconium oxo-alkoxide
H	hydrolysis ratio
h^*	critical hydrolysis ratio
k	rate constant
V	volume of particle
r_{ind}	rate at induction time
t_{ind}	induction time
DLS	dynamic light scattering
SLS	static light scattering

I_0	initial intensity (Hz)
I	scattering intensity (Hz)
n	refractive index
n_0	initial refractive index
r	distance between particles
E	electric field
E_T	total scattered electric field
k_B	Boltzmann constant
R	radius of particle
D_f	fractal dimension
D	diffusion constant

Symbols

Δt_{ind}	different induction time
α	order reaction
β	order reaction

Chapter II: Characterization methods

In this part, we will describe about general techniques and principle of the characterization methods including, thermal analysis TGA-DTA, transmission emission spectroscopy (TEM), X-ray diffraction, BET for specific surface area, optical band gaps measurement and inductively coupled plasma-optical emission spectroscopy (ICP-OES).

II.1 Thermal analysis TGA-DTA

Thermogravimetric analysis (TGA): Thermogravimetric analysis (TGA) consists of measuring the mass variation of a material as a function of time and temperature. This technique is used to determine the characteristics of materials such as thermal stability, the kinetics of chemical reactions, volatility, and adsorption-desorption etc.

Differential thermal analysis (DTA): This technique measures the difference in temperature between a sample and a reference when both are heated under the same atmosphere. The temperature difference between the reference Tr and the sample Ts is followed and plotted against Tr as a differential thermogram. Peaks present in a differential thermogram result from physical changes such as phase transition or chemical reactions induced by heating the sample. The thermal effect can be exothermic or endothermic.

In this work, thermal behaviors of samples were carried out on a SETARAM TG-DTA 92 device operating simultaneously in thermal gravimetric analysis (TGA) and differential thermal analysis (DTA). The following experimental conditions are used: Prepared powders between 36 to 67 mg were finely ground with a ceramic mortar then introduced into the sample holder and heated from 50 to 1200°C with a rising speed of 2°C min^{-1}.

An example of GTA / DTA curves is given in Figure II-1.

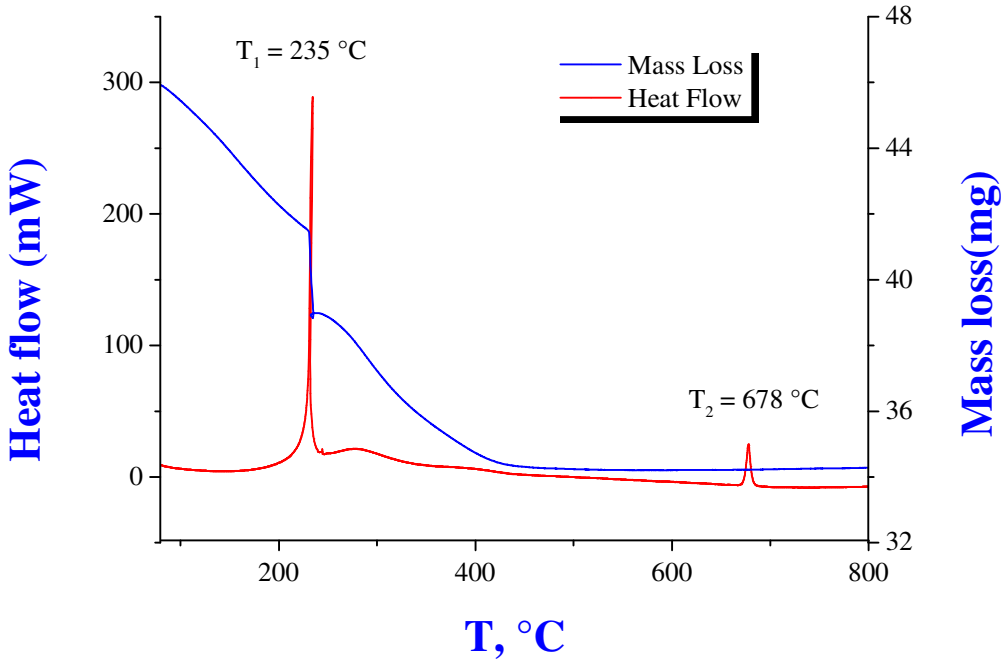

Figure II-1: TGA/DTA curves of a TiO_2-ZrO_2 composite sample obtained with a Setaram 92 device operating in a simultaneous mode.

II.2 Transmission Electron Microscopy (TEM)

Transmission electron microscopy (TEM) is a technique based on the interaction between electrons with atoms constituting the material. Signals produced by a TEM include secondary electrons, back scattered electrons (BSE), characteristic x-rays, light (cathodoluminescence), and transmitted electrons. This technique permits to highlight the morphology and structure of the solids and the possible presence of crystalline defects, deformations, amorphous and crystalline phases. It also allows the determination of crystallographic orientations and the inter-planar distances. The most recent improvements in piloting and aberration correction techniques give to TEM a resolution of the order of angstrom (1Å). Another interest of this technique is to be able to combine this high resolution with the information provided by the sample diffraction. The samples are observed by transparency, visualized by fluorescent screen in order to adjust the focus. The pictures are obtained using a CCD digital camera.

In this work, the prepared samples was characterized using JEOL2011 high resolution transmission electron microscopy (TEM) operating at 200 KeV with LaB_6 emission source of electrons. The electron diffraction and absorbance patterns were

measured as well. Element maps (Zr and Ti) of the prepared samples were obtained using energy filtered transmission electron microscopy (EFTEM) with Gatan Imaging Filter 2000 system connected to TEM. The energy and spatial resolutions of the system were respectively 1 eV and 1 nm.

Samples finely ground using an agate mortar are dispersed in an ethanol solution and sonicated around 10 min. One droplet of the suspension is placed onto a 3 mm holey carbon-coated copper grid.

A typical photograph obtained from a combination of high resolution TEM and diffraction technique for a composite TiO_2-ZrO_2 sample is depicted in the Figure II-2.

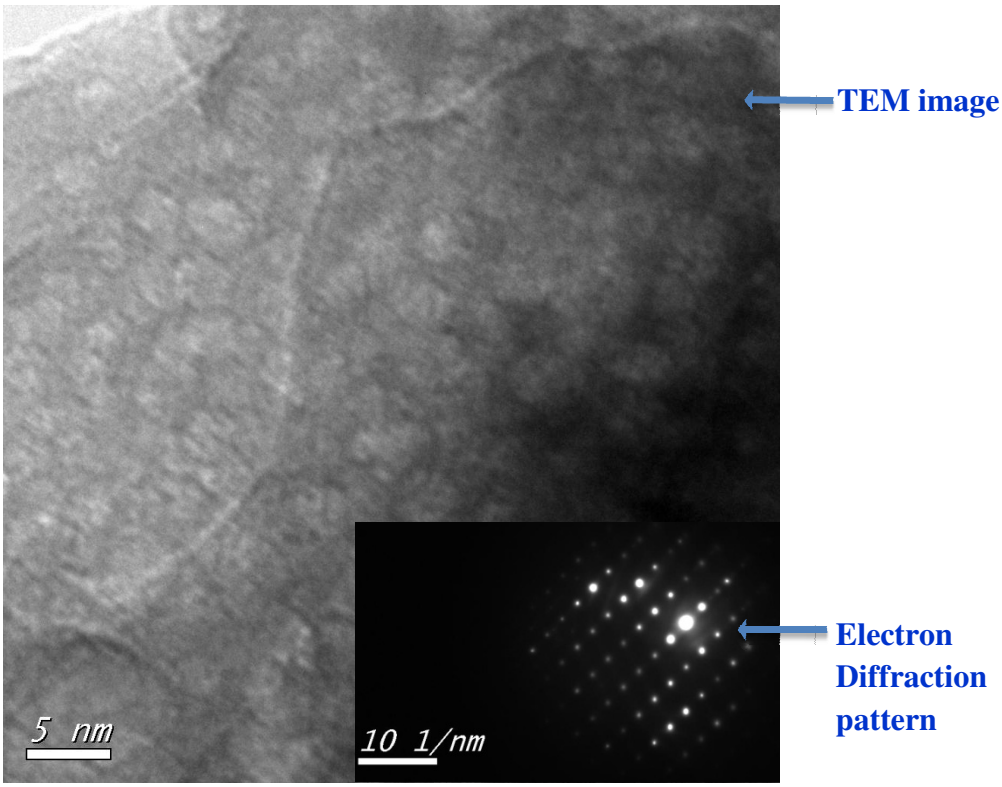

Figure II-2: Microstructure of the composite TiO_2-ZrO_2 realized by High resolution TEM combined with diffraction techniques.

II.3 X-ray diffraction method

X-ray diffraction (XRD) is a non-destructive technique that allows determining, among other things, the crystallinity and nature of different crystalline phases of a material, their relative proportions as well as the size of the crystallites.

When the incident X-ray beam with wavelength λ reaches a crystal lattice, the electrons surround the atoms start oscillating and emitting the same frequency electromagnetic wave. The waves coming from the electronic clouds of the different atoms interfere destructively in most of the directions of space. However, since the atoms of the crystalline materials are organized periodically, there are conditions defined for the waves to interfere constructively and produce an intense beam. In that case, the distance traveled by the X-rays reflected from successive planes differs by a complete number *n* of wavelengths, which leads to Bragg's equation:

$$2d_{hkl}\sin\theta = n\lambda \qquad \textit{Equation II-1}$$

- λ is the wavelength of incident radiation.
- d_{hkl} is the interplanar distance between planes hkl.
- θ is Bragg angle.
- n is the integer of diffraction order.

The general X-ray diffraction by a crystal was shown in Figure II-3.

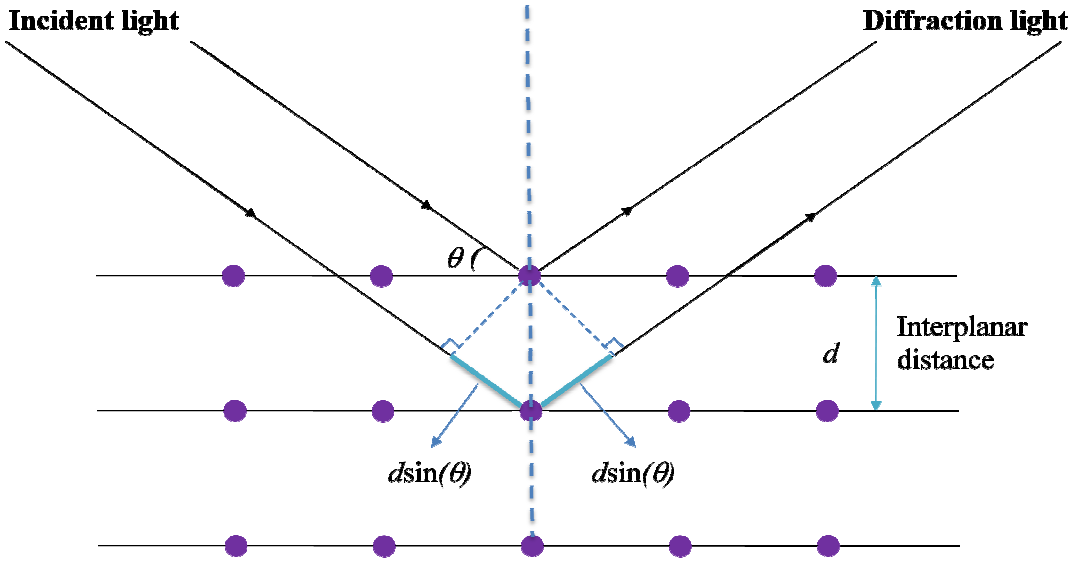

Figure II-3: X-ray diffraction from two planes of atoms in a crystal.

Plotting the angular positions and intensities of the resultant diffracted peaks of radiation produces a pattern, which is characteristic of the sample.

A typical X-ray diffraction diagram of TiO_2 with anatase structure is given in Figure II-4:

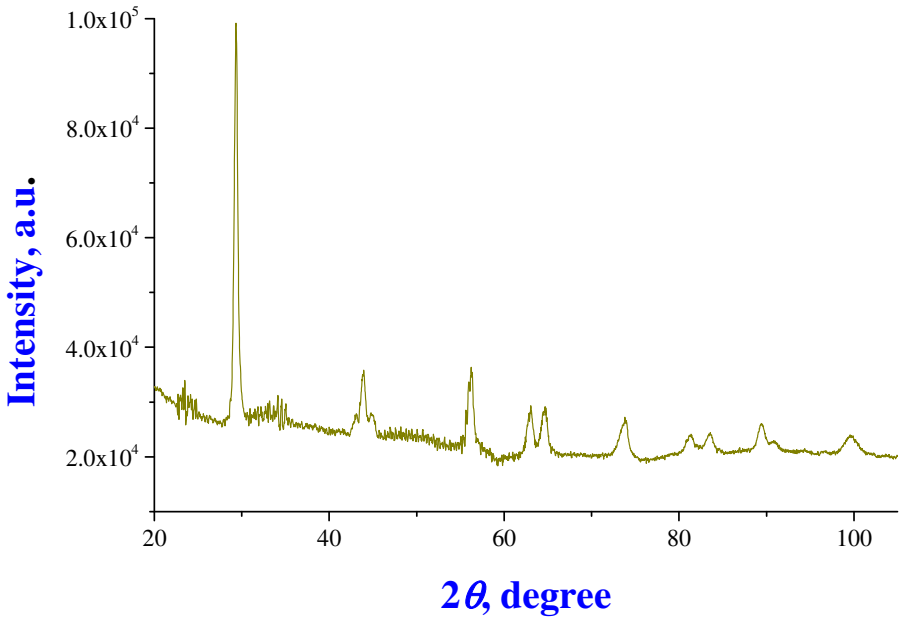

Figure II-4: Typical XRD pattern of TiO_2 anatase.

The intensity and shape of peaks obtained (full width at haft maxima) are influenced by the presence of coherent micro-domains (domain in which the periodicity of atoms is conserved), the size of which can be calculated by the formula of *Debye-Scherrer* [144] using the broadening of the X-ray diffraction lines.

$$\phi = \frac{K\lambda}{\beta \cos(\theta)} \qquad \textit{Equation II-2}$$

- ϕ is the average size (in Å).
- β is the line broadening at half the maximum intensity (in radians).
- θ is the Bragg angle (in degrees).
- K is a dimensionless shape factor, with a value close to unity. The shape factor has a typical value of about 0.9, but varies with the actual shape of the crystallite.
- λ is the X-ray wavelength (in Å).

This method is applicable for crystallites of size between 2-150 nm and gives a measurement with an accuracy of 1 to 10%. This method is generally used for comparative purposes.

In this work, the treatment powders were analyzed with Benchtop X-ray Diffractometer (EQUINOX 1000-Inel) with Co-radiation ($CoK\alpha_1$ (λ=1.788976 Å)).

II.4 Brunauer–Emmett–Teller (BET) for specific surface area

Surface area and porosity are important parameters in powdered materials. The most widely used techniques for estimating surface area are based on physical adsorption of gas molecules on a solid surface. The method is based on the determination of the gas volume required to form a monolayer of gas at the surface of the sample at the temperature of the liquid nitrogen. The adsorbed gas volume is determined according to the Brunauer, Emmet and Teller (BET) model according to the formula:

$$P/[v(P_0-P)]=[1/(V_mC)]+[(C-1)/(V_mC)]P/P_0$$

P = pressure at equilibrium

P_0 = adsorbate saturation pressure at the working temperature

v = volume of adsorbed gas per gram of solid at the pressure P

V_m = volume of gas required to completely cover the surface of the solid with a molecular monolayer of adsorbate

C = characteristic constant of the studied gas-solid system

This equation allows to determine the adsorbed gas volume in mono-layer, V_m. Once this volume is known, the specific surface of the sample is obtained by the following equation:

$$S_{\text{BET}}=(V_m/22414)N_a\sigma$$

S_{BET} = total sample surface

σ = surface occupied by a gas molecule, $\sigma = 0.162$ nm^2 for N_2 at 77 K.

N_a is Avogadro number, $N_a = 6.022\times10^{23}$ / mol.

V_m is determined by plotting the straight line: $P/[v(P_0-P)]$ as a function of P/P_0.

In this work the specific surface measurement is carried out via an automatic BET COULTER SA3100 by nitrogen adsorption. The samples of the composite powders were degassed for 1 hour under a nitrogen or helium sweep at 120 °C. The precision of the measurements is in the order of 3%. The schematic representation of BET instrument during experimental process is in Figure II-5.

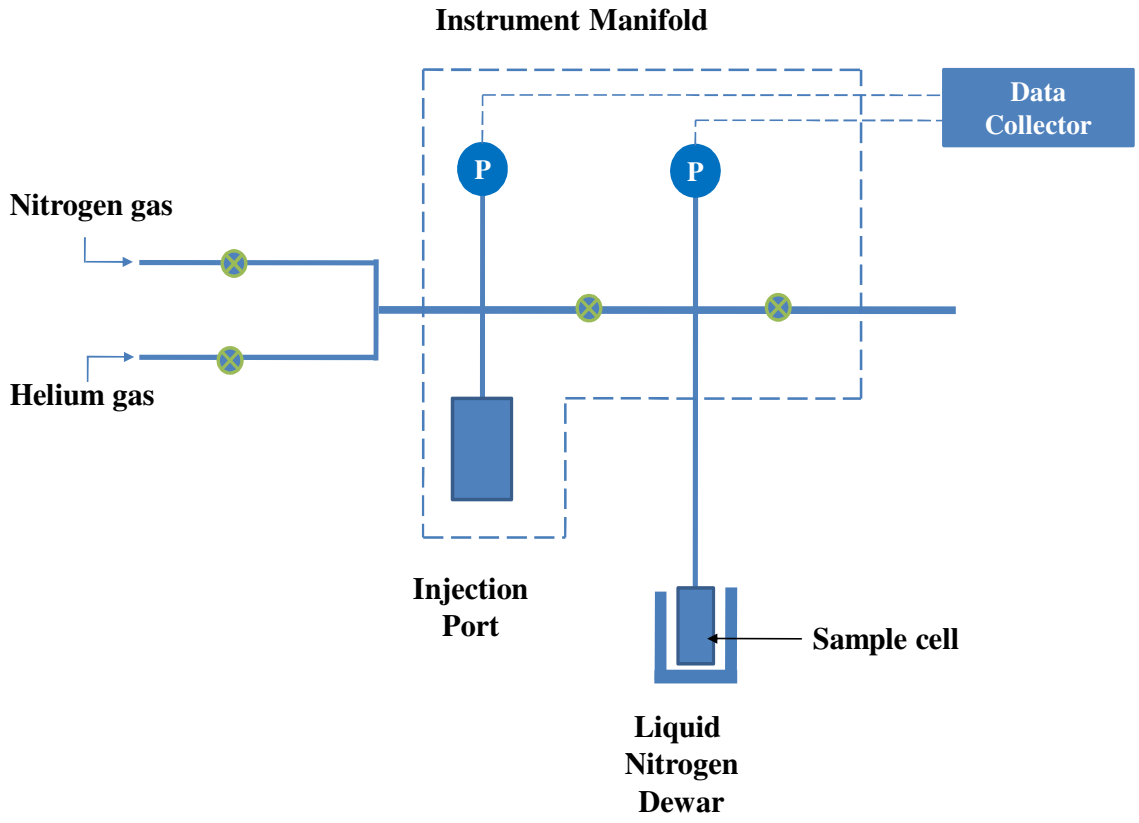

Figure II-5: Schematic representation of BET [145].

II.5 UV-visible absorption

The band gap energy E_g of as synthesized nanoparticles was calculated from the following equation $\alpha(h\nu) = A(h\nu - E_g)^n$ where α, ν, E_g and A are the absorption coefficient, light frequency, band gap energy and a constant respectively [146]. Among them, n is determined by the type of optical adsorption of a semiconductor (n = 1/2 for indirect transition and n = 2 for direct transition). For a semiconductor material, a plot of $(\alpha h\nu)^{1/n}$ against $h\nu$ should show a linear domain just above the optical absorption edge. The band energy was calculated by extrapolating a straight line to the abscissa axis, where α is zero for $E_g = h\nu$ [147].

In this work, the constant n is taken equal n = 2 and the optical absorption was measured by an Jasco V-660 UV-visible spectrometer. The substrates without coating were used as blanks and the coated quartz substrates were oriented during the experimental measurements to be easy to omit the interferences.

Samples were prepared as films of five layers using dip-coating technique. To obtain well-crystallized composite, samples were heat-treated for 4 h at 410-700 °C in a furnace under continuous air flow.

Figure II-6 gives an example of the above-mentioned analysis for a well-crystallized sample of TiO_2-ZrO_2.

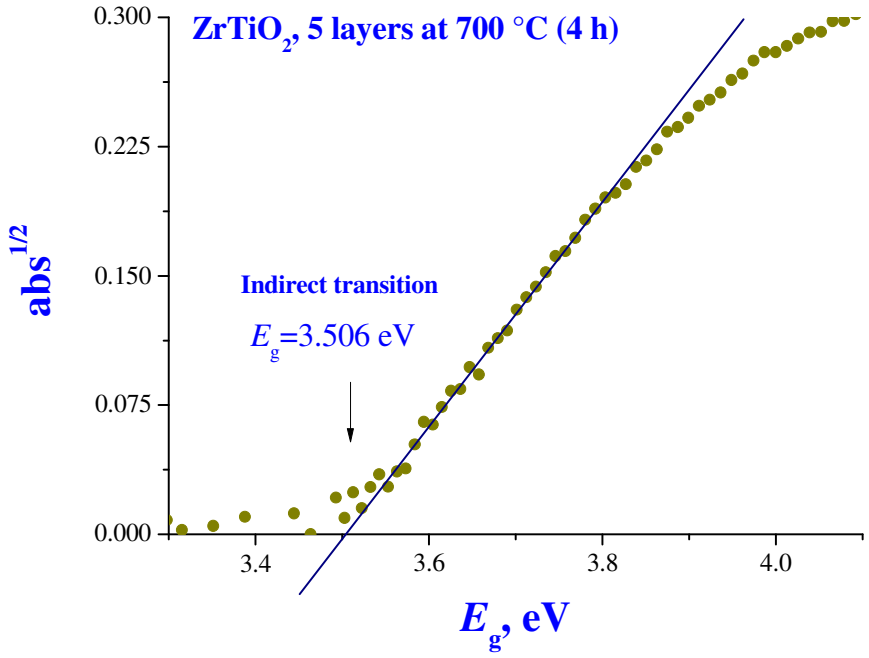

Figure II-6: Typical absorption $(\alpha h\nu)^{1/2}$ versus $h\nu$ plot for a TiO_2-ZrO_2 composite sample. The experimental band gap value can be obtained from the x-intercept of the straight tangent line to this plot.

II.6 Inductively coupled plasma-optical emission spectroscopy (ICP-OES)

One method for analysis metals in the materials is inductively coupled plasma-optical emission spectrometry. Atoms of the samples are excited from ground to excited states when the plasma energy is applied. While the excited atoms come back to lower energy states, the relief emission rays corresponding to the photon wavelength are measured. The determination each element is based on the photon ray position. For the amount of the element type is based on the intensity of the rays. For generation plasma, argon gas is needed to be supplied to the torch coil. Then the electricity with high frequency currents is applied to the coil of the torch tube to create the electromagnetic field. From this, the argon gas is ionized, thus, the plasma is generated. The energy of this plasma that has

high temperature (10000K) and electron density can be used to excite the atoms of the samples. To analyze samples, the solutions of samples are introduced into the plasma through the narrow tube. Samples are atomized in the center of the torch tube. Figure II-7 is the schematic diagram of ICP-OES.

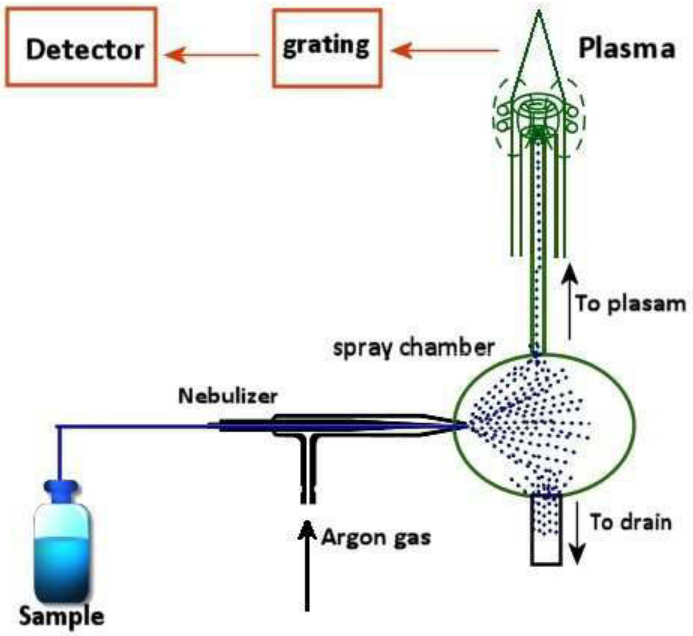

Figure II-7: The general diagram of samples introduced into ICP-OES[148].

The device used in this work is iCAP 6000 that has an optical resolution < 0.02 nm. The spectrometer is equipped with a polychromator with optical assembly of the type Scale purged and thermostatic at 38 °C. The spectral range is between 193 and 900 nm. The detector RACIDTM is of type CID and the generator is RF 27, 12 MHz. The iCAP 6000 provides direct control via the iTEVATM software.

The analysis was carried out in aqueous matrix. Calibration is carried out using CLARITAS PPT multi-element solutions with a 10 ppm concentration of elements in an H_2O / HF / HNO_3 solution. The precision of the concentration is 0.05 ppm and is verified by SPEX Certi Prep. The detection limit is < 4.5 ppb. The exposure time was 2 min.

In this experiment, samples were prepared according to the following procedure:

Powders: 1-2 mg of ZTOA powders were digested by concentrated of HNO_3 (15 mol/L) with stirring and heating at 60 °C for 1 h. The metal ions in solutions were diluted to concentrations of lower than 10 ppm with keeping concentrations of HNO_3 about 6 mol/L.

Films: Coated $Zr_xTi_{1-x}O_2$ borosilicate beads between 2-4 g were digested and diluted in the same as procedure as for powders.

Notation

ZTOA	zirconium titanium oxo-alkoxide
TGA	thermogravimetric analysis
DTA	Differential thermal analysis
TEM	transmission emission microscopy
T	temperature (°C)
mW	milliwatt
E_g	band gap (eV)
eV	electron volts
d_{hkl}	interplanar distance of Miller indices
n	interger of diffraction order
K	dimensionless shape factor
UV	ultraviolet
abs	absorbent
ppm	part per million
ppb	part per billion
ICP-OES	inductively coupled plasma-optimission emission spectroscopy
Symbols	
h	planck's constant ($6.626 \times 10^{-34}\ j \cdot s$)
ν	light frequency (Hz)
λ	wavelength (nm or Å)
ρ	density ($kg.m^{-3}$)
η	dynamic viscosity (Pa.s)
ϕ	average size (Å)
β	mid-height width (radian)
θ	diffusion angle (°)

Chapter III: Preparation of size-selected ZTOA nanoparticles

This chapter is devoted to an experimental study of the nucleation and growth kinetics of composite zirconium titanium oxo-alkoxy nanoparticles. The first part describes the solvent effect on titanium oxo-alkoxide nanoparticles, which provided a reference point to the study of the more complex composite system. The main part of this chapter will concern the mixed oxide zirconium-titanium oxo-alkoxide nanoparticles of different compositions.

III.1 Introduction

III.1.1 Solvent effect on nucleation-growth of titanium-oxo-alkoxy nanoparticles

The sol-gel process of transition metal alkoxides is of permanent interest since a long time [79, 149, 150]. Recently, its classical description has been reconsidered regarding the structure and reactivity of molecular precursors to conclude that the simplified hypothesis of the kinetically controlled hydrolysis-polycondensation process is not realistic. In contrast to the unconsciously accepted, the hydrolysis does not proceed for homometallic alkoxides via hydroxide intermediates but results directly in well-defined oligonuclear oxo-alkoxide species through one-step hydrolysis-condensation transformation associated with profound restructuring of the oxometallate species as the reactions progress [151-153]. The soft chemistry processes occurring in gas, liquid and solid phases share common features of nanomaterial formation from precursor to solid and require further investigation.

Unfortunately, little information is available concerning hierarchy of different smallest metal-oxo-alkoxy units, clusters and nanoparticles, appearing in the beginning of a chain of the sol-gel transformations as well as about their relative stability and reactivity. The most studied were titanium-oxo-alkoxy (TOA) species [154], which thermodynamically stable molecular species have been experimentally discovered and theoretically confirmed. The size of these identified clusters is smaller than 1 nm. Small angle x-ray scattering (SAXS) measurements in titanium oxide sol-gel media have revealed two stages of the induction period related to precursor hydrolysis and directed by reaction limited aggregation mechanism and concluded about smallest building blocks of 0.46 nm size [155]. Although structure and size of the smallest species are expected to be sensitive to the surface state and therefore solvent environment, general conclusions about sol-gel kinetics of titania species studied by SAXS and DLS/SLS (dynamic / static light scattering) methods were similar.

Larger cluster escaped observations for different reasons and their theoretical validations were limited by a calculation methods capacity.

An obstacle in the observation of nanometric oxo-alkoxy nanoparticles consists in a high reactivity of sol-gel species leading to a common polydispersity of the prepared colloids. Accordingly, no kinetic constants of hydrolysis-polycondensation reactions are known in literature and only an estimation of the process rates was communicated in the past [79]. In order to overcome natural heterogeneity of the nucleated units, attempt to create point-like reaction conditions was undertaken by us [108, 110, 155]. As a result, we succeeded in preparation of easily observable macroscopic quantities (~1 g) of size-selected titanium-oxo-alkoxy (hydrodynamic radius R = 1.6 nm and 2.5 nm) [102] and zirconium-oxo-alkoxy (R = 1.8 nm) [105] clusters and nanoparticles. Moreover, zirconia species showed a strong sensitivity to the solvent / precursor nature suggesting modifying ligands to be involved in the structural transformations. These two systems remain however the only example of nanometric metal-oxo-alkoxy species reported until now and more studies would be required to understand the nucleation mechanism.

The present study is devoted to the solvent effect on the titanium oxide species stability and reactivity. The experiments were conducted in point-like reaction conditions, which provide equal starting conditions for chemical transformations and, therefore, best selectivity for the nucleated TOA units. The units size and growth kinetics were inquired by light scattering methods, enabling new information about role of ligands in the nucleation process.

III.1.2 Kinetics nucleation-growth of the mixed zirconium titanium oxo-alkoxide nanoparticles

The sol-gel method for production of solid materials from precursors of small molecules has been extensively studied and developed since decades [78, 149]. It showed its particular efficiency for synthesis of composite materials, for which the homogeneity of a local structure is considered to be a major precondition for the material quality and functional properties control. The sol-gel method and its modifications have been effectively used to prepare mixed zirconium and titanium oxides for applications as catalysts and catalytic supports [13] for different applications in photocatalysis, water photosplitting, catalysis, microporous ceramic membranes for gas separation, dye sensitized solar cells, etc.

The previous studies have shown that the new phase crystallization is strongly affected by the local material composition. In particular, pure TiO_2 and ZrO_2 crystallites showed up at temperatures about 400 °C and an addition of one component to other resulted in a significant increase of the crystallization temperature by ~300 °C [37]. This partially explains why in many studies, anatase TiO_2 and monoclinic/tetragonal ZrO_2 appeared as dominant crystalline phases of the composite material with no evidence for formation of any zirconium titanate compounds [18, 38, 57, 69, 70, 156], when heat treatment temperatures characteristic of the amorphous crystalline phase transition in titania and zirconia (400-500 °C) were applied to the mixed oxide. However in other cases, even when an appropriate heat treatment was used, a definite dispersion of the crystalline phase's stability versus an average elemental composition could be remarked. For example, Liang et al [48] have reported on polymorphous samples containing orthorhombic $ZrTiO_4$ with tetragonal ZrO_2 and anatase TiO_2 with respectively Zr:Ti=0.7:0.3 and Zr:Ti=0.3:0.7 and pure $ZrTiO_4$ crystallite at Zr:Ti=0.5:0.5. Similar results have been obtained at somewhat lover (25 mol% Ti or Zr) elemental admixtures [40]. The anatase TiO_2 and tetragonal ZrO_2 solid solutions have been observed respectively with 30 % Zr and less than 40 % Ti, while the orthorhombic $ZrTiO_4$ appears in the range of 40-70 % Zr [37]. The orthorhombic $ZrTiO_4$ was often mixed with monoclinic or tetragonal ZrO_2 in samples with < 50% Ti [59]. The low-temperature phase diagram of TiO_2-ZrO_2 composites has been proposed by Xu et al [157], suggesting the stability of $ZrTiO_4$ solid solutions in the range of $20 \leq Zr/(Zr+Ti) \leq 50$ mol%; TiO_2 anatase and mixed monoclinic-tetragonal ZrO_2 solid solutions appear respectively at Zr < 20 mol% and Zr > 60 mol%, while pure tetragonal ZrO_2 solid solutions crystallized in the range between 50 and 60 mol% of Zr in the ZrO_2-TiO_2 compositions. A choice of the processing chemistry of $ZrTiO_4$ has been reported to have little influence on the homogeneity and local structure of the calcined precursors, where EXAFS data clearly indicated the presence of Zr-O-Ti links in the $ZrTiO_4$ gel produced using the nonhydrolytic route [39]. This conclusion however concerned the samples with stoichiometric amounts of zirconium and titanium, in confirmation of previous experimental data on the pure orthorhombic $ZrTiO_4$ phase; the non-stoichiometric compositions have not been addressed in this detailed study.

The sol-gel synthesis was previously considered as a sequence of chemical reactions starting with hydrolysis of alkoxides and terminating with the condensation step. Consequently, an eventual difference in the hydrolysis and condensation rates of Ti- and Zr

alkoxides has been suggested to be a major problem in the preparation of the atomically dispersed mixed oxide structure and its solution lied in the control of the reaction rates [13]. This simplified picture of the kinetically controlled hydrolysis-polycondensation reactions has been recently reconsidered. In particular, it has been shown that the hydrolysis does not proceed for homometallic alkoxides via hydroxide intermediates but results directly in well defined oligonuclear oxo-alkoxide species through one-step hydrolysis-condensation transformation associated with profound restructuring of the oxometallate species as the reactions progress [151, 152, 158]. The same mechanism could be expected also working for the mixed metal oxide species. In framework of this new understanding of the sol-gel process, the centre of gravity of the relevant research shifts from understanding of elementary reactions kinetics (which has never been measured so far) to that of intermediate nanometric units and their transformations.

In support of this approach, particle sizes and nucleation-growth process of titaniumoxo-alkoxy (TOA) [102, 159] and zirconium-oxo-alkoxy (ZOA) [105] species have been investigated using a rapid micromixing reactor [108, 110]. This technique enables point-like reaction conditions in a regime of low Damköhler numbers Da ≤ 1 [129], which allowed generating size selected clusters and nanoparticles and distinguishing important steps of the sol-gel growth. In these earlier studies, species appeared in the beginning of the induction period of the sol-gel process, R = 2.6 nm TOA and R = 1.8 nm ZOA were assigned to nuclei. Consequently, nuclei and their associates were called nanoparticles, in contrast to smaller stable species appeared at small hydrolysis ratio (H) and/or as intermediates during the nucleation stage at large H, which were assigned to clusters: R = 1.6 nm TOA. The crystalline materials have been obtained on this base to show their enhanced effectiveness in catalytic (ZrO_2) [160] and photocatalytic (TiO_2) [161] processes. In contrast, no information concerning relationships between the nucleated units and crystalline phases obtained after the heat treatment was reported in literature until now for complex mixed oxides ZrO_2-TiO_2. At the same time, the nanoscale morphology does not only define size-specific functional properties but also those of the bulk solids, especially in case of doped and composite materials. In this communication, we present first study of the nucleation and growth process of mixed zirconium-titanium oxo-alkoxy (ZTOA) nanopaticles of different elemental compositions $0 \leq x \leq 1$ ($x = C_{Zr}/(C_{Ti} + C_{Zr})$). The nanoparticle size and growth kinetics were monitored *in situ* by the dynamic/static light scattering methods.

In this part, we will describe the revealed results of monodispersed, new and stable domain nanoparticle sizes at different compositions and the change sizes at different hydrolysis ratios of mixed ZTOA. More detail, the kinetics mechanism of selected composition $x = C_{Zr}/(C_{Zr} + C_{Ti})$ was studied.

III.2 Experimental part

III.2.1 Chemicals

Chemicals used in this study were TTIP (98%, Acros), n-propanol (99.5%, Sigma-Aldrich), 2-propanol (99.5%, Acros), zirconium n-propoxide (ZNP, 70 wt% supplied by Interchim) and distilled twice-filtered water (syringe filter 0.1 and 0.2 µm porosity PALLs Acrodisc for synthesis ZTOA and TOA respectively). To avoid contamination with atmospheric humidity, all chemical manipulations related to the stock solutions preparation were carried out in a glove box workstation MBraun ($O_2 \leq 80$ ppm, $H_2O \leq 0.5$ ppm).

For TOA synthesis, we used the TTIP concentration of 0.146 and 0.292 mol/l and hydrolysis ratio $H = C_{H_2O}/C_{Ti}$ between 1.0 and 4.0.

For synthesis ZTOA(x) nanoparticles, the concentration of the mixed precursor ZNP+TTIP ($C_{pr} = C_{Zr} + C_{Ti}$) was kept constant at 0.292 M with the molar composition $x = C_{Zr}/C_{pr}$ varied between 0.0 and 1.0 in a step of 0.1. The hydrolysis ratio $H = C_{H_2O}/C_{pr}$ was varied between 1.0 and 2.0 with the precision estimated to be 0.05. The following are structures of precursors and solvents that been used:

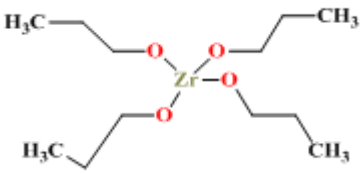

Zirconium(IV) propoxide

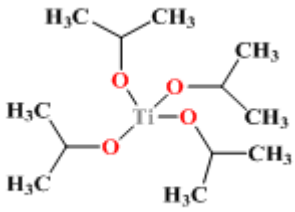

Titanium(IV) isopropoxide

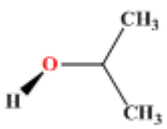

Isopropanol

n-propanol

III.2.2 Chemical reactor with ultrarapid micromixing

The experiments were carried out with microreactor similar to Rivallin et al. [108]. Figure III-1 is shown the reactor set up: (A) precursors (TTIP or mixed TTIP with ZNP) and (B) water in n-propanol and isopropanol as solvents. Both precursors and water were in the same solvent for each conducted experiments.

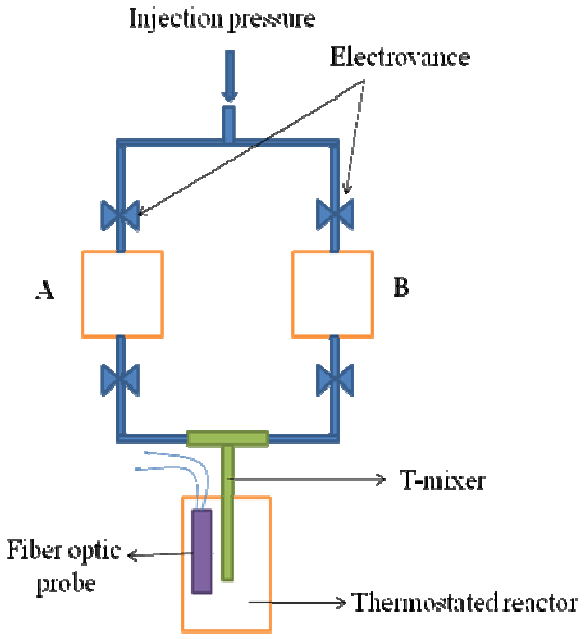

Figure III-1: Representative of the microreactor for sol-gel synthesis from the reaction of TTIP with water in n-propanol and isopropanol as solvents (A) for precursor and (B) for water.

The nanoparticles were prepared by sol-gel method with rapid micromixing reactor described in our previous studies [108, 110]. Two stock solutions of 50 mL each, containing (A) precursors of TTIP in different concentrations or mixed TTIP/ZNP with different elemental ratios $0 \le x \le 1$ in solvent and (B) water in solvent, were prepared in the glove box and injected by a syringe into the thermostatic stock tanks. After synchronous opening of the magnetic valves, the pressure (4 bar) of dry nitrogen gas pushed synchronously the stock solutions A and B into a T-mixer of Hartridge and Roughton type with two inlet arms of 1 mm diameter and outlet arm of 2 mm diameter. The injected fluids with the flow rate about 10 m/s exhibit a strong turbulence by propagating through the mixed zone with Reynolds numbers ~6000 ($Re=4Q\rho/\pi\eta d$, where Q, ρ, and η are respectively flow rate, density and dynamic viscosity of the fluid). The reactor operated at 20.0 °C controlled with Haake

DC10K15 thermo-cryostat. The reacting fluids mixed in these conditions during several milliseconds, which assured point-like reaction conditions with Da ≤ 1, which signifies that characteristic time of the fluid composition homogenizing being shorter compared to that of chemical reactions, leading to the narrowest particle size distribution [129]. In order to avoid any extra atmospheric contaminations, the reactor was maintained under overpressure 0.1 bar of N_2 gas during the preparation process. The experimental series in the reactor were limited by 24 hours duration to guarantee an excellent isolation of the reaction solution from external atmosphere.

Solvents: n-propanol and isopropanol for TTIP and only n-propanol for mixed TTIP/ZNP

The main place of mixed solutions is at the mixing zone in T-mixer and then reaction happened of precursors with water in prepared solvent. This whole process is shown in Figure III-2 (clusters may be built in T-mixer after mixing zone).

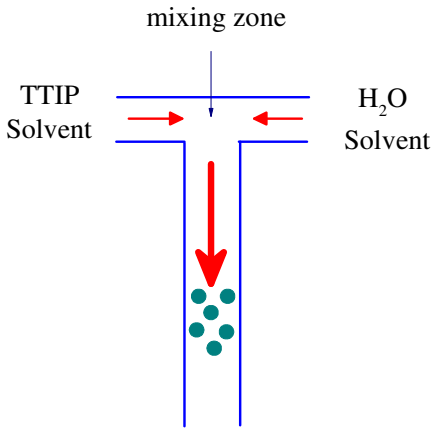

Figure III-2: Representative of mixing zone in T-mixer (● is representative of particle built after mixing).

Dynamic light scattering (DLS) and static light scattering (SLS) methods were used to monitor the size (2R, nm) and scattered light intensity (*I*, Hz) of nanoparticles in the reactor solutions, using an original home-made fibre optical probe, consisted of two monomode optical fibres. One emitting fibre transmitted 40 mW light radiation at $\lambda = 640$ nm from a single frequency laser Cube 640-40 Circular (Coherent) another receiving fibre collected the light scattered by colloidal nanoparticles and transmitted it for the analysing equipment, photon correlator Photocor-PC2 (48 bits / 288 channels). The observation volume defined by a mutual positioning of two monomode optical fibers is small enough (~10^{-6} cm^3) to avoid multiple scattering events even in high-concentration

colloids. The intensity and size were measured with 60 s data accumulation periods in the automatic sampling mode, which permits easy elimination of non-desirable strong scattering events due to rare micronic-size dust particles. The particle radius was obtained from the Stokes-Einstein equation $R = k_B T q^2 \tau / 3\pi\eta$ where k_B, T, $q = \frac{4\pi n}{\lambda \cdot Sin(\theta/2)}$, η and n are respectively Boltzmann constant, temperature, scattering vector, dynamic viscosity and refraction index of the solution, and the decay time τ was obtained by experiment and fitting to autocorrelation curves (ACF). The particle radius from this formula is equivalent to that of a spherical particle having the same diffusion coefficient. The smallest size of these measurements R = 1.0 nm was defined by the self-correlation function of the PhotoCor photomultiplier. The duration of experimental series of (R, I) evolution in the colloids was limited by 24 hours.

III.2.3 Manual mixing for estimation induction time of oxo-TiO_2

Before doing the experiments with micromixing reactor, a simple manual mixing was carried out to be estimated the induction time for aggregation time of TOA particles in n-propanol. The solution containing precursor as (A) with TTIP 0.292 M in n-propanol with stirring in 10 min was prepared in glove box. After that, it was brought out of glove box and then tested manual mixing with solution containing water as (B) (H = 2.5, 3.0, 3.5, 4.0 and 4.5 after mixing). The following are the steps and conditions of experiments:

- 10 mL from (A) with stirring in beaker and 10 mL (B) solution was slowly dropped into it (concentration of Ti after mxing was 0.146 M).
- After mixed 5 min, the colloidal solutions were transferred into vials and then closed and waited to see the precipitation time.
- There was no temperature control (10-25 °C) in whole experiments.
- During mixing and waiting 5 min, there was no moisture and oxygen control (the experiments were conducted in atmosphere).

During the mixed precursors before hydrolyzing, it is possible of rearrangement with role of Ti-O-Zr bonding that was proposed by Yutaka et al [162] as the following this equation:

$$n\mathrm{Ti(OC_3H_7)_4} + n\mathrm{Zr(OC_3H_7)_4} \rightarrow [\mathrm{Ti(OC_3H_7)_m - O - Zr(OC_3H_7)_m}]$$

III.2.4 Micromixing experiments for synthesis TOA

Two solutions of precursor TTIP and water were prepared in two beakers separately in glove box: (A) titanium(IV) isopropoxide and (B) water were dissolved into n-propanol and isopropanol preparation and then stirred by magnetic stirrer around 200 cycles per minute. The stirring time was carried out in 10 min for each solution continuously starting from (A). These solutions were transferred into the syringes and stoppers were used to close the syringe needles to protect the penetration of oxygen and moistures into the solutions when they were brought out of glove box. The general preparation is shown in Figure III-3.

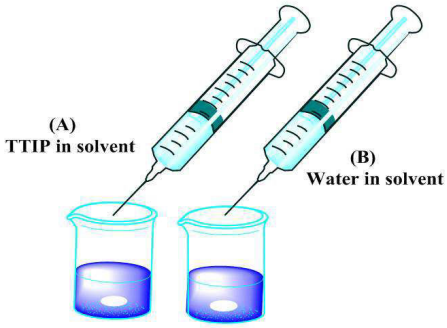

Figure III-3: Representative of precursor and water solutions is in beakers and then they were transferred into syringes as preparation in glove box.

The time of the stock solutions preparation and transfer to the thermostatic reactor after the glove box operations was about 25 min. The reactor volumes (A) and (B) were filled with the stock solutions under dry nitrogen gas flow to avoid any atmospheric contamination. The reactor performance was checked by measuring the standard induction time 50 ± 5 min of the TTIP/H_2O = 0.146/0.365 solution in isopropanol [108].

III.2.5 Micromixing experiments for synthesis ZTOA

III.2.5.1 Starting point for ZTOA nanoparticles synthesis

We started mixing of oxo-alkoxide nanoparticles ZTOA experimentations with the equimolar or x = 0.5 of $C_{Zr} = C_{Ti}$ = 0.146 M and hydrolysis ratio $H = C_{H_2O}/C_{pr}$ in n-propanol according to the monodispersity from previous studies of TOA and ZOA in case only one kind metal element. The concentration of water was started by C_{H_2O} = 0.365 M and

in this case, H would be 2.5 if all molecules of water reacted with only titanium or only zirconium precursors. If all molecules of titanium (IV) isopropoxide reacted with water in n-propanol, the particle size should be 1.9 nm with the infinite induction time. If all molecules of water reacted with zirconium (IV) propoxide, the particle size would be 1.8 nm with the induction time around one hour.

III.2.5.2 Protocol of preparation of stock solutions

The following are the steps for preparations of precursors and water in glove box before injection into tanks (A) and (B) of microreactor:

- n-propanol was prepared in each beakers, labeling (A) and (B). The prepared volumes of solvent in beakers (A) and (B) depended on the volumes of precursors and water (the densities of titanium(IV) isopropoxide and zirconium(IV) propoxide were 0.9500 and 1.044 g/ml respectively.).
- Zirconium(IV) propoxide precursor was firstly dissolved in solvent and then TTIP precursor.
- This solution was stirred in 10 min to get homogeneity of precursors in solvent. After that it was transferred into syringe.
- Water solution (in n-propanol) was also carried out after mixed dissolved precursors in the same process.
- It was taken around 25 min including brought out of glove box (total time before injection).
- Note: Up to several percent isopropoxide from TTIP alkoxide groups may contain in some solutions in case of high percentage titanium precursor contents.

III.3 Solvent effect of nucleation and growth of TOA nanoparticles

III.3.1 Induction kinetics of TOA with manual mixing

The precipitation times of the aggregation TOA were noted by naked eyes seeing the white appeared particles (changed from transparent to white color): The precipitation times are in the table III-1.

Table III-1: Induction time of TOA for different hydrolysis ratios in n-propanol solvent with manual mixing

Hydrolysis ratio, H	Induction time, min
2.5	infinite
3.0	infinite
3.5	37
4.0	18
4.5	5

These results helped us to be estimated the amount of hydrolysis ratios for new environment TOA particles as solvent effect for our experiments with micromixing reactor of environmental and temperature control.

III.3.2 Solvent effect on TOA kinetics with micromixing

The induction kinetics of the sol-gel process using the same TTIP precursor and different solvents, n-propanol and isopropanol, are shown in Figure III-4. In both cases, the appearance of a precipitate comes after some time called "induction period", during which small nanoparticles nucleate and grow by a mutual aggregation. Despite of much similarity in this behavior, clear differences between the two systems can be remarked: (i) reactivity of TOA species in isopropanol is higher compared to n-propanol, since the same induction time is obtained with much smaller water content, and (ii) nucleus size in n-propanol (2R~4 nm) is larger compared to that in isopropanol (2R~5 nm).

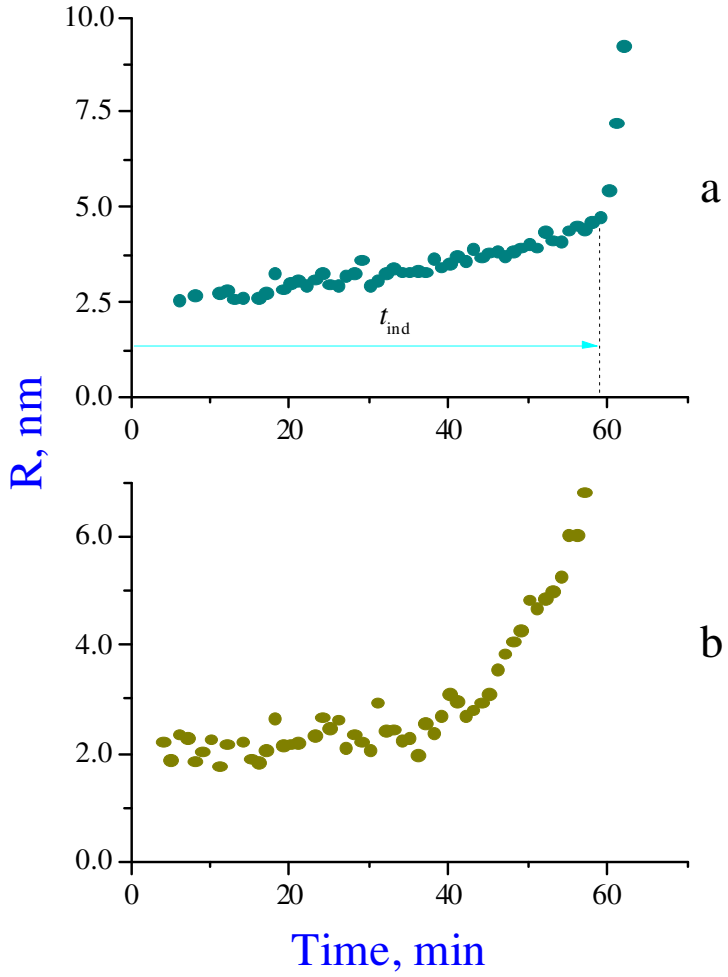

Figure III-4: Evolution of TOA particles radius in (a) isopropanol (H=2.5) and (b) n-propanol (H=3.4) solvents (C_{Ti} = 0.146 mol/l, T = 20.0 °C, Re ≈ 6000).

More detailed comparison between the two systems can be made in framework of the induction model proposed by Soloviev et al. [94] and formalized by Rivallin et al. [95, 108]. Based on a general description of the hydrolysis and polycondensation reactions, it was assumed that they coexist while the first one is totally reversible and the second has a critical condensation number, above which the reversibility is cancelled. The integral population balance equation (PBE) was solved by the moment transform method to obtain the induction rate expressed as

$$r_{ind} \equiv \tau_{ind}^{-1} = kC_{\mathrm{Ti}}^{\alpha}(H - h^{*})^{\beta} \qquad \textit{Equation III-1}$$

where C_{Ti} is the titanium precursor concentration, $H = C_{H_2O} / C_{Ti}$ is the hydrolysis ratio, h^* is the critical hydrolysis ratio that defines the amount of water consumed on the nucleation stage prior to aggregation, α and β are the reaction orders and *k* is a constant. The critical hydrolysis ratio h^*=1.5 has been suggested by Soloviev at al. [94] to explain the condensation ratio related to the chemical composition of the oxo-alkoxy nucleus $TiO_{1.5}OR$ and the amount of free water remaining in the solution after the nucleation stage H-h^*, which enables nanoparticles aggregation. Long time after these studies, this critical hydrolysis ratio was admitted however not verified. In particular, Azouani et al [102] have considered different H-domains of the sol-gel process concluding about the appearance of stable clusters with R_{cl} = 1.6 nm at H ≤ 1.7 and stable nuclei enabling induction kinetics at H ≥ 2.0; the limited growth of clusters towards nuclei was proposed in the intermediate domain between these two H values. These results made clear necessity to verify the critical h^* value.

Using the suggested h^* = 1.5, induction rates in two solvents n-propanol and isopropanol are shown versus H-h^* in Figure III-5a. The linear fit (dotted lines 1 and 2) of the n-propanol data in logarithmic frame results in a slope β = 5 as predicts the model equation III-1 [94, 95, 108]. The same slope has been previously reported for the induction rates in isopropanol solvent, which indicates a strong similarity between both systems. Our results support the critical value of the hydrolysis ratio h^* = 1.5 compared to 2.0, since the experimental data plotted for h^* = 2.0 (curve 3 in Figure III-5a) significantly deviate from linearity. Being not evidence, this analysis supports a validity of the earlier proposed model (1) for the oxo-alkoxy species growth in both studied solvents.

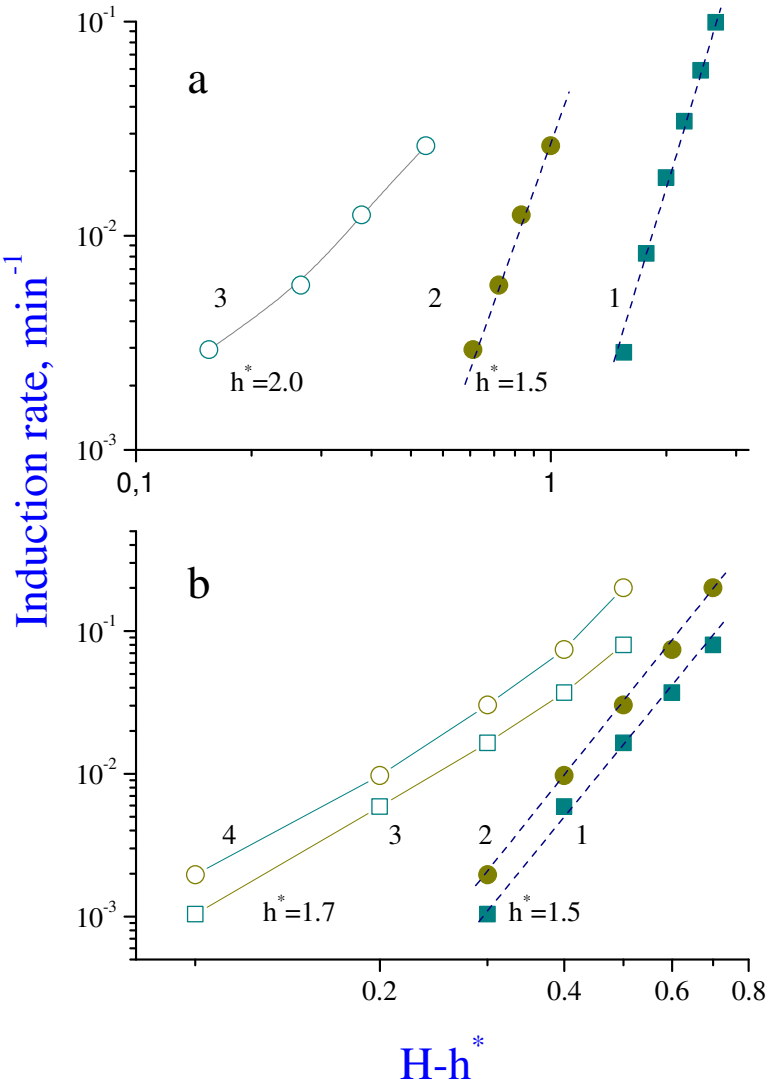

Figure III-5: Induction rate ($1/t_{ind}$) versus H-h for large H >2 (C_{Ti} = 0.146 mol/l) (a) and low H < 2 (C_{Ti} = 0.292 mol/l) (b) in n-propanol (■, □) and isopropanol (●, ○) solvents. The critical h* is taken 1.5 (1 and 2 in (a) and (b)), 1.7 (3 and 4 in (b)) and 2.0 (3 in (a)).*

III.3.3 Kinetics comparison at high precursor concentrations

A better selection between possible h* values could provide direct measurements of the induction period at low H < 2.0. In general, at the precursor concentration C_{Ti} = 0.146 mol/l the induction time tends to "infinity" when H approaches 2.0, i.e. becoming longer than limiting 24 hours of the experiment. This however does not allows to conclude that the critical h* value is equal to 2.0 since the very slow induction rates failed to be observed at

the experiment timescale. To overcome an ambiguity in the experimental data interpretation, we performed a series of measurements with a higher precursor concentration of C_{Ti} = 0.292 mol/l. According to equation III-1, this accelerates the induction rate almost two orders of magnitude, thus allowing decreasing H by remaining within the allowed experimental timescale t ≤ 24 hours.

Two series of experiments with C_{Ti} = 0.292 mol/l and H = 1.8 and 1.9 in n-propanol solvent are shown in Figure III-6a. Similar measurements (not shown in figure) were performed in iso-propanol solvent. These measurements permitted to refine the model by choosing between h^* = 1.5 and another possible value 1.7, which according to Azouani et al [102] corresponds to the beginning of the limited growth of oxo-alkoxy clusters. Indeed, Figure III-5b shows a very good agreement with the model (β = 5 in equation III-1) for h^* = 1.5 while indicates a significant deviation from the power low for 1.7 in both solvents. This strongly argues in a favour of the choice h^* = 1.5 compared to higher critical values 1.7 and 2.0. One can conclude that the limited (1.7 < H ≤ 2.0) and accelerated (H > 2.0) growth domains take part of a common growth process responsible for the TOA species evolution from clusters to nanoparticles.

III.3.4 Fractal dimension of TOA in n-propanol

The analysis of the fractional dimension of the particles during the induction stages was carried out based on Soloviev et al. [163] and Rivallin et al. [107]. They investigated at the starting clusters and growth nanoparticles and condensation by aggregation in the induction stages during the sol-gel reaction of the TTIP. The total mass (M) is constant during the process and in case that one particle with radius R has mass m, the total number of particles is $N_i = \frac{M}{m}$. Because the intensity scattered a particle under Rayleigh conditions is squared $i \infty m^2$, the total intensity of the scattered light (I_D) by the whole of the particles in suspension in the solution is:

$$I_D \propto N_i m^2 \propto \frac{M}{m} m^2 = Mm \propto m \qquad \textit{Equation III-2}$$

A fractal particle has mass m and fractal dimension D_f has a hydrodynamic radius R, so $I \infty R^{D_f}$.

Figure III-6b shows a logarithmic plot I(R) of the experimental data in Figure III-6a. As it has been previously shown [94, 95], the light intensity scattered by the interacting nanoparticles (I) is related to their radius (R) as

$$I \propto R^{d_f} \qquad \textit{Equation III-3}$$

where d_f is the fractal dimension of the associates. We obtained a low fractal dimension close to 1 of the growing TOA species in n-propanol, which is characteristic of quasi-linear chains. Complementarily to previously published results in isopropanol solvent, the new data show a continuity in the linear association of clusters (H < 2.0) and nanoparticles (H ≥ 2.0) as two parts of the common process kinetics. Indeed, the linear lines in Figure III-6b correspond to the cluster association at R < 2 nm and nanoparticles association at R ≥ 2 nm.

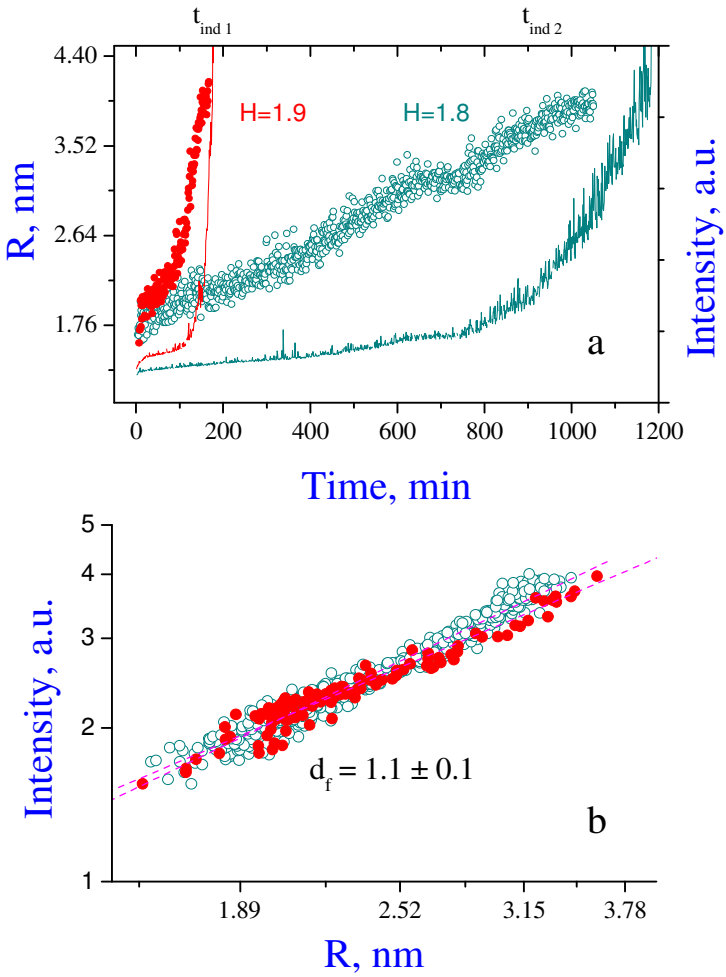

Figure III-6: (a) Induction kinetics R(t) (●, ○) and I(t) (solid lines) and (b) plot I(R) in logarithmic frame for H=1.8 (●) and 1.9 (○) in n-propanol (C_{Ti} = 0.292 mol/l, T = 20.0 °C,

Re ≈ 6000). The dotted line in (b) is least-squares fit of the experimental data with Equation III-3.

III.3.5 Particle sizes of TOA in different solvents

The kinetics of TOA clusters and nanoparticles in n-propanol and isopropanol solvents support the growth model of Refs [94, 95, 108]. As Figure III-4 shows, the reaction rate is strongly affected by solvents and that in n-propanol is much slower. Our results show that solvents also affect the nanoparticle size. The hydrodynamic sizes of TOA species in n-propanol and isopropanol solvents are shown respectively in Figure III-7a and Figure III-7b for different H between 1 and 4. In both solvents, clusters with a radius R = 1.6 nm appear in the very beginning of the process and convert to nanoparticles, which hydrodynamic radii are different in n-propanol R = 1.9 nm and isopropanol R = 2.6 nm. This suggests a strong sensitivity and adaptability of these TOA species to the environment, in a general agreement with refs [151, 164, 165]. In contrast, the small clusters possess a strong energetic stability, which permits conserving their structure in different liquid environments. We assume that this stronger stability of smaller units compared to larger ones reflects the hierarchy of oxo-alkoxy species, which also manifests itself in the growth process kinetics. In fact, the limited growth of TOA clusters can be easily observed at small $H \leq 2$ (Figure III-6) while it is difficult to distinguish as a part of the kinetic curves at large H (Figure III-4), which can be explained by the rapid kinetics controlled by a large amount of free water in the solution.

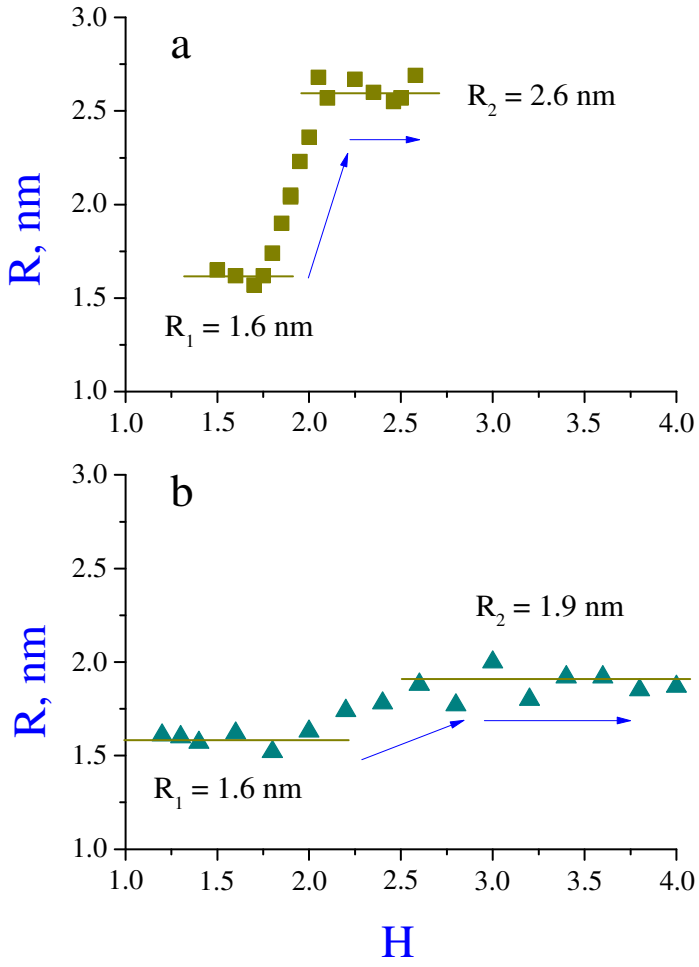

Figure III-7: Particles radius evolution with H in (a) isopropanol (b) n-propanol solvent (C_{Ti} = 0.146 mol/l, T=20.0 °C, Re = 6000).

In small-H domain (H ≤ 2), the cluster size and reaction kinetics are almost not sensitive to the solvents. In contrast, in the large-H domain (H>2), where the basic structural unit becomes nanoparticle and the process kinetics is governed by reactions between nanoparticles, both size and reaction rate are sensitive to the nature of solvent. The observed relative stability of the smallest structural oxo-alkoxy units (clusters) in different solvents in a broad range of water and precursor concentrations requires further clarification of the common features of the oxometallate species restructuring.

III.3.5.1 TOA species growth in isopropanol

For the concentration TTIP = 0.292 M in isopropanol, the particle sizes TOA in the evaluation growth seem to be bigger than 0.146 M with the difficulty of measurements and

as an example of the nucleation with the evaluation growth of particles is shown in Figure III-8.

The particles are nucleation immediately after injection and then growth in sometimes. As in Figure III-8a, the size was R_0 = 2.5 nm in line (1) when it is plotted only with the linear data at the beginning. But if it is plotted in general, it should be above R_0 = 3.0 nm as line (2) in Figure III-8a. The general mechanism should be similar to Figure III-8b. It is rapid at the beginning and then become normal linear growth up to aggregation.

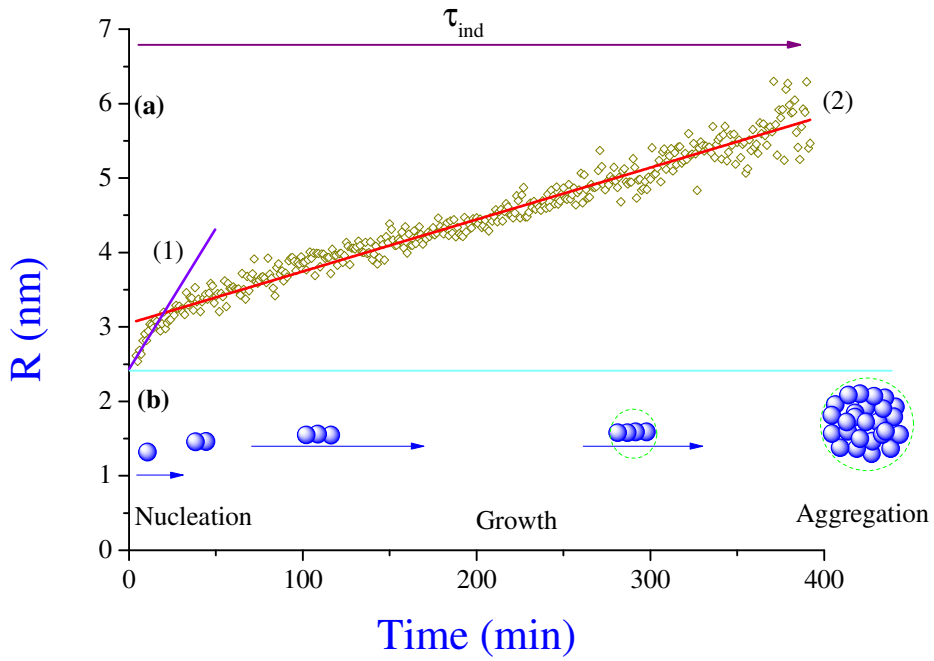

Figure III-8: Evolution of TOA particles radius in isopropanol (H = 1.8) solvent (C_{Ti} = 0.292 mol/l, T = 20.0 °C, Re ≈ 6000). (a) For the selected fitting at the beginning (1) and general fitting (2) and (b) for the general representative mechanism of nucleation and growth.

The intensity of the induction stage increased quickly and induction time is selected at the intensity five times bigger than the beginning. As in Figure III-9, then induction time is around 3.6 h.

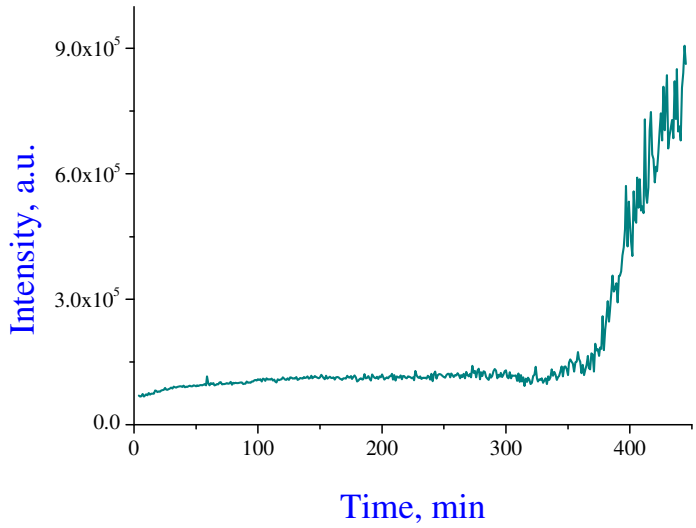

Figure III-9: The scattering intensity of TOA particles in isopropanol (H = 1.8, C_{Ti} =0.292 mol/l, T = 20.0 °C, Re ≈ 6000).

III.3.5.2 TOA particle size in n-propanol

Figure III-10 shows TOA particle sizes in n-propanol at 0.292 M TTIP different hydrolysis ratios. They are quite similar to that at twice lower precursor concertation of 0.146 M in the range of relatively low hydrolysis ratios.

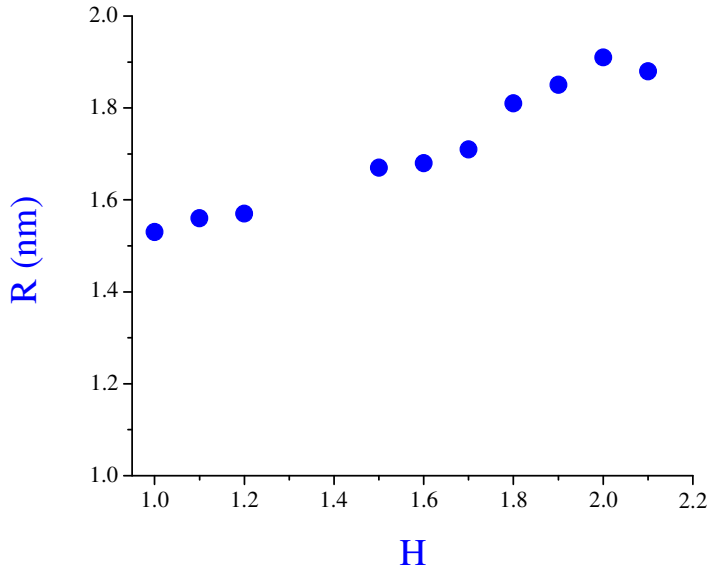

Figure III-10: Particle sizes of TOA in n-propanol as the concentration 0.292 M (T = 20.0 °C, Re ≈ 6000).

III.4 Nucleation and growth kinetics of ZTOA nanoparticles

III.4.1 Particles polydispersity

The point-like reaction conditions attained with the micromixing reactor permit nucleating monodispersed ZOA and TOA nanoparticles. This conclusion, however, cannot be undoubtedly extrapolated to the mixed oxide ZTOA nanoparticles, because of eventually different chemical activities of the precursors. We therefore checked the particles monodispersity with the DLS method. An example of the measured autocorrelation function (ACF) of the ZTOA nanoparticles for equimolar concentrations of zirconia and titania precursors ($C_{Zr} = C_{Ti} = 0.146$ mol/l, $x = 0.5$) with H = 1.25 in n-propanol solution is shown in Figure III-11. One can see no appreciable deviation of the experimental points from the single exponential decay, which signifies quasi perfect monodispersity of the nucleating nanoparticles with the mean radius of 2.08 nm and standard deviation of the experimental points ~1%. Based on the measured ACF data, we concluded about point-like reaction conditions and, consequently, regime of low Damköhler numbers in sol-gel solutions under study. The size of ZTOA nanoparticles suggests comparable reactivates of both precursors. Indeed if one of Zr or Ti would dominate, the correspondent species evolves advantageously in the reaction conditions with equivalent local hydrolysis ratio $h_{eq} = 2.5$, which leads to the nucleus size of 1.9 nm (TOA) or 1.8 nm (ZOA), which are significantly different from then those measured, R = 2.08 nm. Both precursors, therefore, undergo simultaneous hydrolysis condensation reactions after the micromixing, forming composite oxo-alkoxy species.

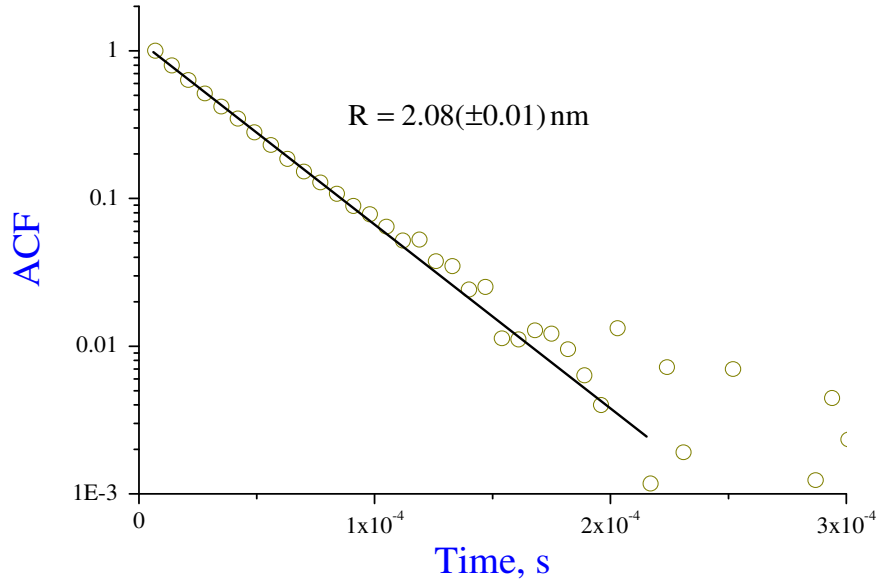

Figure III-11: Characteristic ACF of ZTOA nanoparticles in n-propanol($C_{pr} = 0.292$ M $x = 0.5$, $H = C_{H_2O}/C_{pr} = 1.25$, *T = 20 °C, Re ≈ 6000).*

III.4.2 Induction kinetics versus hydrolysis ratio

More investigation of the induction kinetics was carried out with the composition x = 0.5 at different hydrolysis ratios. In the range of H = 1.25-1.50, the particle size was stable with R = 2.1 nm and the induction time is infinite. Different from this, the particle size was changed to be bigger to R_0 = 2.6 nm from H = 1.55 as shown in Figure III-12. Also we observed the kinetics about how it grew. To get the induction time, the intensity was assumed five times higher than the initial values. Table III-2 showed the induction time, the detail of initial radius particle sizes with standard deviations in different hydrolysis ratios.

Table III-2: Initial radius of nano-composites (R_0) and induction times for different hydrolysis ratios H ($C_{Zr} = C_{Ti} = 0.146$ M, T = 20 °C).

H	R_0 (nm)	ΔR (nm)	t (ind) (min)
1.25	2.08	0.02	infinite
1.30	2.11	0.04	infinite

1.40	2.06	0.06	infinite
1.50	2.06	0.03	infinite
1.55	2.50	0.04	infinite
1.60	2.45	0.06	175
1.65	2.65	0.04	100
1.70	2.78	0.08	43
1.75	2.69	0.04	23
1.80	2.71	0.08	12.5

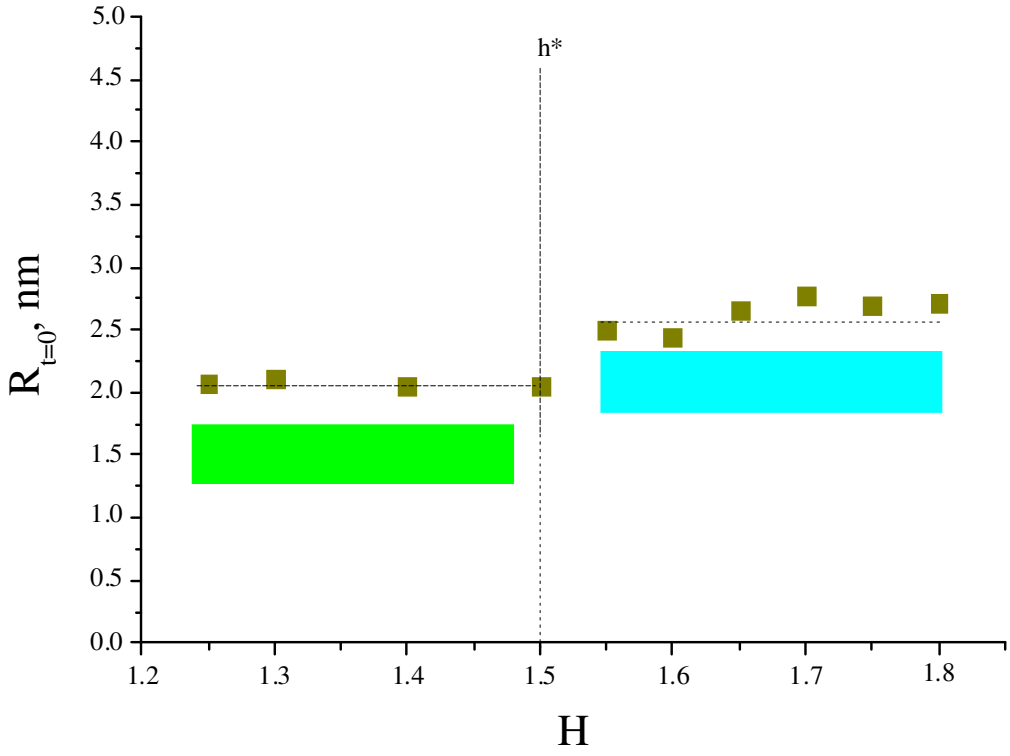

Figure III-12: Initial radius of mixed ZTOA (R_0) for different hydrolysis ratios H ($C_{pr} = 0.292$ M, $x = 0.5$, T = 20 °C, $Re \approx 6000$).

The ZTOA nanoparticles prepared at low hydrolysis ration, as e.g. those presented in Figure III-13, form stable colloids. In contrast, at higher H the characteristic induction period of the sol-gel process can be observed, during which the nanoparticles grow by agglomeration [149] and precipitate at the end. The precipitation corresponds to the formation of large particles which strongly scatter the incident light. This can be monitored

by the SLS measurements presented in Figure III-13 for a fixed precursor concentration and $1.6 \leq H \leq 1.8$, which label *I*(t) curves. The particle growth accelerates with an increase of water concentrations in the solution. As Rivallin et al [108] have shown, the induction kinetics can be represented by induction rate (in s^{-1}) equivalently expressed in terms of the inverse induction time and slope of *I*(t) curves:

$$r_{ind} = \tau_{ind}^{-1} \propto dI / dt \qquad \textit{Equation III-4}$$

It can be also shown that the intensity scattered by the ensemble of colloidal nanoparticles can be expressed as:

$$I \propto \mu_2(t) = \int_{m^*}^{\infty} m^2 F(m,t)\,dm \qquad \textit{Equation III-5}$$

where m_2 is the second momentum of the particle mass (m) distribution F(m,t). We checked the equivalence hypothesis of equation III-4 and confirmed that it holds in case of the ZTOA nanoparticles growth. We therefore assumed that the basic mechanism of the particles agglomeration is common for simple metal oxide, TOA and ZOA, and mixed oxide ZTOA nanoparticles.

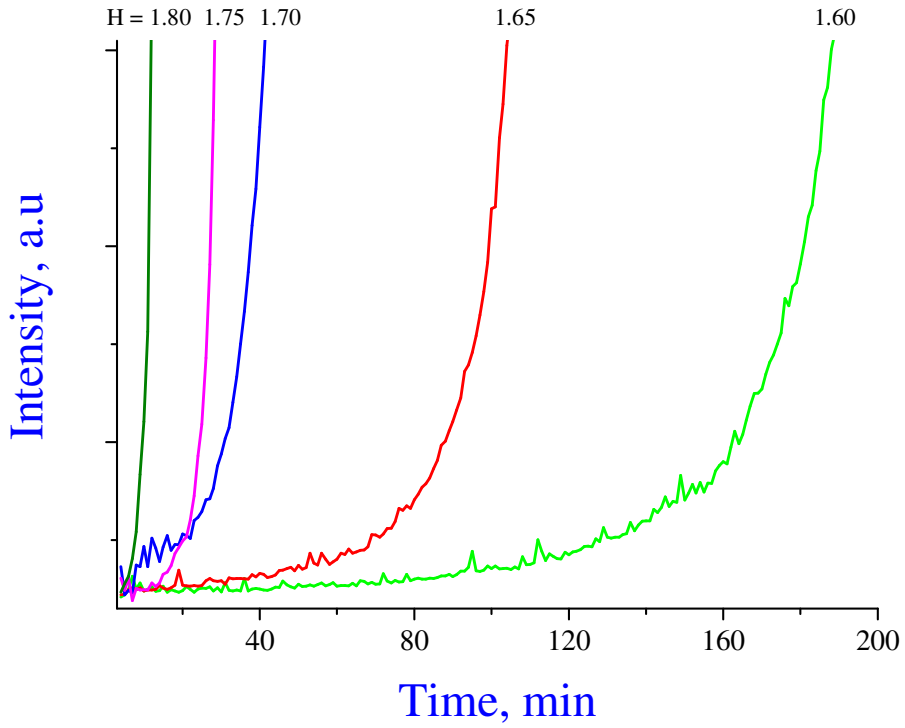

Figure III-13: The temporal evolution of the scattered light intensity during induction period of mixed ZTOA in n-propanol for different hydrolysis ratios H, ($C_{pr} = 0.292\,\mathrm{M}, x = 0.5$, *T = 20 °C, Re ≈ 6000).*

The particle radius dependence on H is shown in Figure III-12 and table III-2. We notice that R_0 = 2.08 nm at low H ≤ 1.5 corresponds to the stable colloids, while it suddenly changes to R_0 = 2.6 nm at H > 1.5. The last one represents the initial radius of ZTOA nanoparticles in the beginning of the induction period. In agreement with earlier studied TOA species [102], we ascribed smaller species to sub-nucleus units - clusters and larger units to nucleated nanoparticles, which grow by mutual aggregation during so-called induction stage. The ratio of their respective volumes assuming spherical shapes is 2, which suggests the formation of nucleus by coalescence of two clusters. In case that the plotting the rate ($1/t_{ind}$) versus hydrolysis ratios was done, the relation was exponential as shown in Figure III-14.

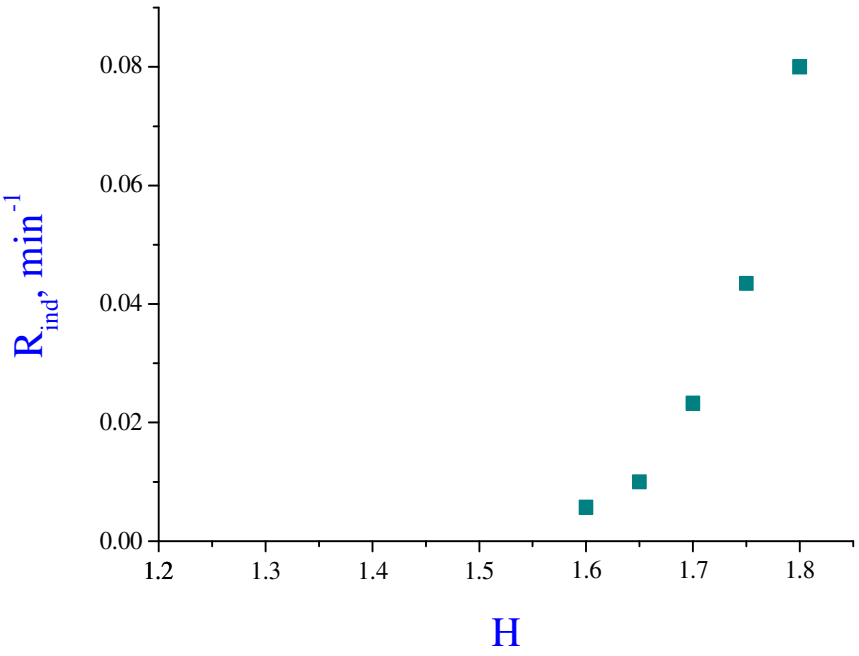

Figure III-14: Dependence of induction time on the hydrolysis ratios ($C_{pr} = 0.292\,M, x = 0.5$, T = 20 °C, Re ≈ 6000).

The dependence of the induction rate t_{ind}^{-1} on hydrolysis ratio H, according to experimental data of Figure III-12, is shown in Figure III-13. The colloid stability was confirmed for H ≤ 1.5, while H > 1.5 enables the induction period. The sol-gel process rate (equation III-4) can be expressed as [94]:

$$r_{ind} = kC_{pr}^{a}(C_{H_2O} - C_{H_2O}^{*})^{b} = kC_{pr}^{a+b}\left(H - h^{*}\right)^{b} \qquad \textit{Equation III-6}$$

where k, C_{pr}, C_w and h^* are respectively reaction constant, precursor, water molar concentrations, and critical hydrolysis ratio accounted for the nuclei formation, above which the nuclei aggregation becomes possible. The coefficients a and b in equation III-6 describe the reaction order related to zirconium and titanium precursors and water molecules, which is generally higher than 1. In order to experimentally evaluate critical h^* of the ZTOA sol-gel growth, r_{ind} was plotted versus H as shown in Figure III-15. The best fit by the power law resulted in $h^* = 1.45 \pm 0.05$ and $b = 4.0 \pm 0.4$. The obtained h^* is similar to that previously reported for TOA and ZOA species [102, 105], which signifies the common onset of the condensation process between surface hydroxyls. At the same time, the reaction order b is smaller compared to that of TOA (b = 5) and ZOA (b = 6.6) species. In agreement with the proposed model [108], this indicates different critical numbers of surface hydroxyls making the condensation process irreversible.

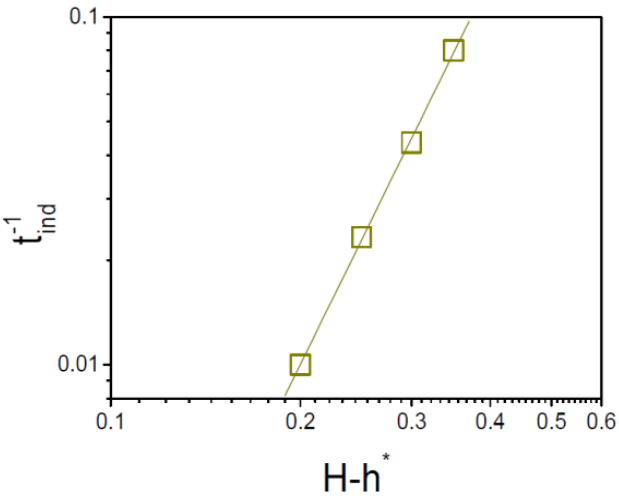

Figure III-15: Dependence of the induction rate on the hydrolysis ratio excess a critical value h = 1.45 ($C_{pr} = 0.292\text{M}, x = 0.5$, T = 20 °C, Re ≈ 6000).*

We also checked the relation of the slope with the induction rate. It was linear with the value of $\frac{dR/dt}{R_{ind}} = 1.36 \pm 0.13$ and Figure III-16 is shown for this relation.

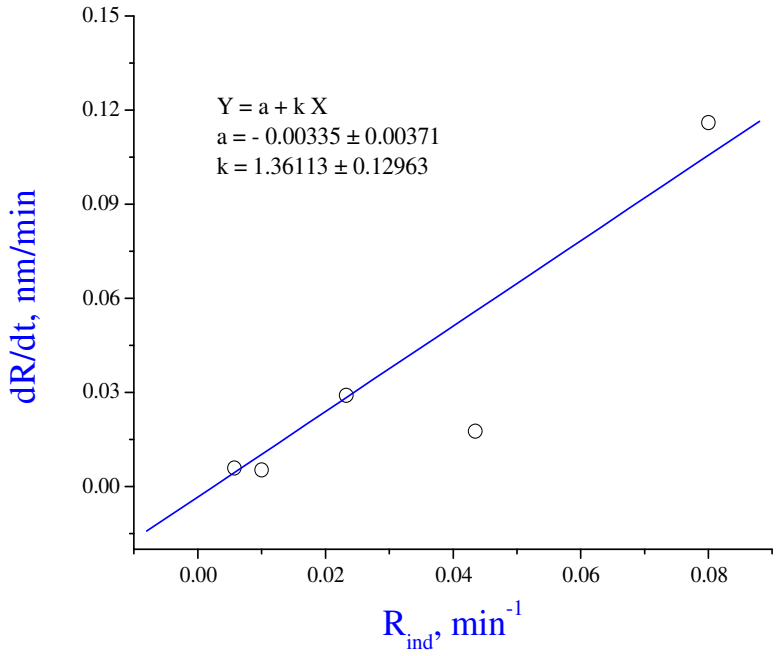

Figure III-16: Slope of I(t) curves versus induction rate ($1/t_{ind}$) during the induction period of the ZNP–TNP–n-propanol sol–gel process for different hydrolysis ratios H ≥ 1.6 ($C_{pr} = 0.292\text{M}, x = 0.5$, *T = 20 °C, Re ≈ 6000).*

III.4.3 Nucleus size for different ZTOA compositions

The size of ZTOA nanoparticles is sensitive to the elemental composition *x* as evidences Figure III-17. In agreement with previous observations, all colloids prepared with a fixed precursor concentration $C_{Zr} + C_{Ti}$ = 0.292 mol/l and H = 1.25 were stable. The particles radii of pure TOA and ZOA species (respectively *x* = 0 and 1 in our notations) correspond to those earlier measured in TTIP/n-propanol, R = 1.6 nm [159], and ZNP/n-propanol, R = 1.8 nm [105], solutions. On the other hand, the radii of species with intermediate compositions progressively increase with an addition of the second element, Zr for x > 0 and Ti for x < 1, into host matrixes, respectively TOA and ZOA. The particles radius attains a plateau of 2.08 ± 0.05 nm for the compositions 0.3 ≤ x ≤ 0.7. We assume that stable particles of this size are different from TOA and ZOA nanoparticles, being, at the same time, characteristic of the mixed oxide ZTOA nucleus. Moreover since the variation of the elemental composition does almost not affect the ZTOA nucleus size, we suppose an existence of the "soft" solid solutions of a variable composition that this nucleus adopts.

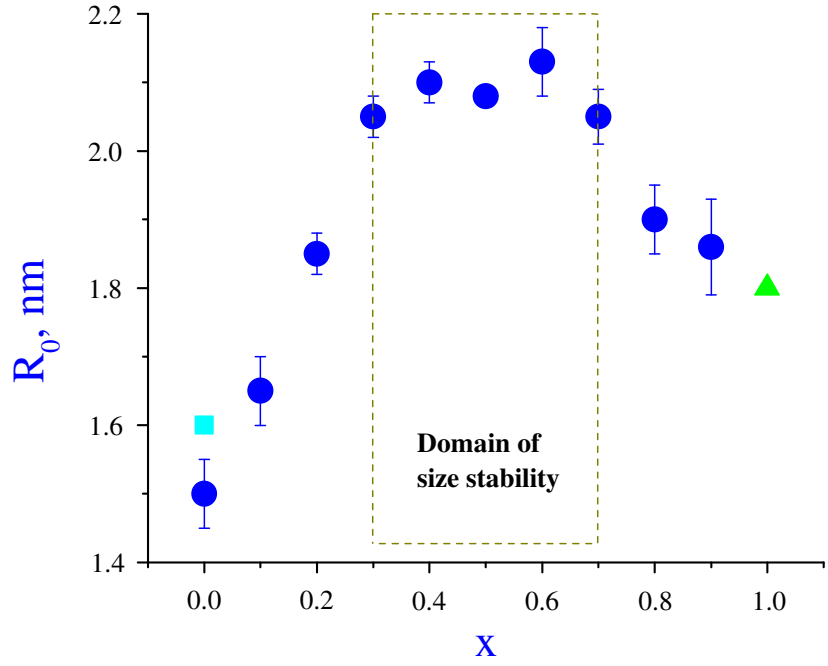

Figure III-17: Radii of ZTOA nanoparticles (●) of difference compositions x (C_{pr} = 0.292 M, H = 1.25, T = 20 °C, Re ≈ 6000). Sizes of reference TOA (■) [159]and ZOA (▲) [105] species prepared in similar conditions are included.

III.5 Conclusion

In conclusion, we performed a comparative study of the nucleation-growth kinetics of titanium oxo-alkoxy nanoparticles in n-propanol and isopropanol solvents. A common feature of the both systems is the appearance of stable clusters with the hydrodynamic radius 1.6 nm in the very beginning of the sol-gel process after an ultra-rapid mixing of the reacting fluids containing titanium precursor and water. The cluster size is stable in a large parametric domain (C_{Ti} and H) of the sol-gel process and is not sensitive to the solvents. At large hydrolysis ratios (H > 2) the basic colloid unit becomes nanoparticle; in this domain both size and reaction kinetics are sensitive to the solvents. In particular, the hydrodynamic radius of the TOA nanoparticles in n-propanol and isopropanol solvents is 1.9 nm and 2.6 nm respectively. Our results suggest that the stability of the growing TOA species decreases with an increase of their size, supporting the hierarchical model of the sol-gel growth. Our analysis confirms the critical hydrolysis ratio h^* = 1.5, which enables the growth of TOA species forming quasi-linear chains of the associating clusters and nanoparticles.

For the concentration 0.146 M, the growth particle TOA in n-propanol solvent is slow with hydrolysis ratio up to 4 (≈ 5 min induction time) while in isopropanol the maximum hydrolysis ratio just only 3 (≈ 4 min induction time). At the concentration of 0.146 M TTIP precursor, the critical *h** (hydrolysis ratio) was possible with 2 and 1.5. But it was 1.7 and 1.5 when the concentrations were double (0.292 M). Anyway, the best fit of rate (1/t) verse with H-*h** was at *h** = 1.5 that is correct to Soloviev's suggestion of aggregation after higher this hydrolysis ratio. In n-propanol with the concentration 0.292 M TTIP, the fractal dimensions were very nice with low values $d_f = 1.1 \pm 0.1$, which are exact quasi-linear chains reactions.

The monodispersed mixed oxide ZTOA nanoparticles of different compositions $0.0 \leq x \leq 1.0$ were successfully synthesized in n-propanol solvent in a sol-gel reactor with ultra-rapid micromixing. At the hydrolysis ratio H = 1.25, the particle size was 2.08 nm for the compositions of $0.3 \leq x \leq 0.7$. The nucleus size progressively decreases to that to ZOA (1.8 nm) for $x \geq 0.8$ and to that of TOA (1.6 nm) for $x \leq 0.2$. The equimolar mixture of zirconium(IV) propoxide and titanium(IV) isoprooxide precursors was used to study the effect of the hydrolysis ratio on the particle size: ZTOA nanoparticles have radius 2.1 nm hydrolysis ratio $H \leq 1.5$ that increases to 2.6 nm for higher hydrolysis ratio. In the same time, mixed oxide ZTOA nanoparticles were stable at $H \leq 1.5$ and underwent an accelerated growth at higher H values showing a common induction period of the sol-gel process. The obtained value of the critical hydrolysis ratio h^* is similar to that previously reported for TOA and ZOA species, which signifies a common onset of the condensation process between surface hydroxyls enabling particles aggregation. The reaction order *b* (equation III-7) is smaller compared to that of TOA (*b*=5) and ZOA (*b*=6.6) species. In agreement with the proposed model by Rivallin, this indicates different critical numbers of surface hydroxyls making the condensation process irreversible.

Notations

TOA	titanium oxo-alkoxide
ZOA	zirconium oxo-alkoxide
ZTOA	zirconium titanium oxo-alkoxides
R	radius of particles (nm)
R_0	initial radius of particles (nm)
H	hydrolysis ratio
*h**	critical hydrolysis ratio
TTIP	titanium tetraisopropoxide
C_{TTIP}	concentration of titanium tetraisopropoxide (mol/L)
C_{Ti}	concentration of titanium (mol/L)
C_{Zr}	concentration of zirconium (mol/L)
C_{H_2O}	concentration of water (mol/L)
C_{pr}	concentration of precursors ($C_{pr} = C_{Zr} + C_{Ti}$) (mol/L)
x	composition of zirconium content compared to concentration of precursors
T	temperature (°C or K)
k_B	Boltzmann constant ($1.38064852 \times 10^{-23}$ m^2 kg s^{-2} K^{-1})
q	scattering vector
θ	angle (°)
n	refraction index
Re	Reynolds numbers
ACF	autocorrelation function
ZNB	zirconium n-butoxide
ZNP	zirconium n-propoxide
DLS	dynamics light scattering
SLS	static light scattering
SAXS	small angle x-ray scattering
TEM	transmission electron microscopy
I	scattering light intensity (Hz)
Q	fluid rate ($m^3 s^{-1}$)
d	diameter (m)
Da	Damköhler numbers

ppm	part per millions
k	rate constant
r_{ind}	rate at the induction time ($\min^{-1}$)
EXAFS	extended x-ray absorption fine structure
m	mass of particle
a and b	order reaction of mixed Zr and Ti precursors
V_{Ti}	size volume of TOA
V_{Zr}	size volume of ZOA
$V_{\mathrm{Ti+Zr}}$	size volume of ZTOA
R_{Ti}	radius of TOA
R_{Zr}	radius ZOA
$R_{\mathrm{Ti+Zr}}$	radius of ZTOA
Symbols	
ρ	density ($\mathrm{kg.m^{-3}}$)
η	dynamic viscosity (Pa.s)
τ_{ind}	induction time (min)
α	order reaction of precursor
β	order reaction of hydrolysis ratio
d_f	fractal dimension
λ	wavelength (nm)

Chapter IV: ZTOA phase transitions and microstructure of $Zr_xTi_{1-x}O_2$

The observed peculiarities of the ZTOA species nucleation in chapter III permit concluding about the homogeneity of the elemental composition at the nanoscale, which is a prerequisite for the preparation of the single phase crystalline $Zr_xTi_{1-x}O_2$ solids. In the following, we consider their crystalline structure and morphology as a function of the elemental composition x.

In this part we will describe about the measurement and characterization results of thermal analysis TGA/DTA, X-ray diffraction, ICP-OES analysis, TEM, Band gaps measurement and BET surface area.

IV.1 TGA-DTA analysis

The differential thermal analysis (DTA) and thermogravimetric analysis (TGA) of ZTOA nanopowders obtained after drying procedure are presented in Figure V-1 and Figure V-3. Two kinds of exothermic peaks were observed in DTA experiments (Figure V-1 and Figure V-3): at low 210-250 °C (T_l) and high 380-680 °C (T_h) temperatures. At the sample time, the mass loss of these samples is almost terminated at temperatures ~400 °C (Figure V-2). Since the high temperature DTA peaks are not accompanied by the mass loss, they were assigned to crystallization. Accordingly, at low temperatures ZTOA nanoparticles undergo structural reorganization by loosing surface alkoxy and hydroxy groups becoming amorphous composite metal oxide nanoparticles:

$$ZTOA \xrightarrow{T_l = 210-250\ ^\circ C} amorphous - Zr_xTi_{1-x}O_2 \qquad \textit{Equation IV-1}$$

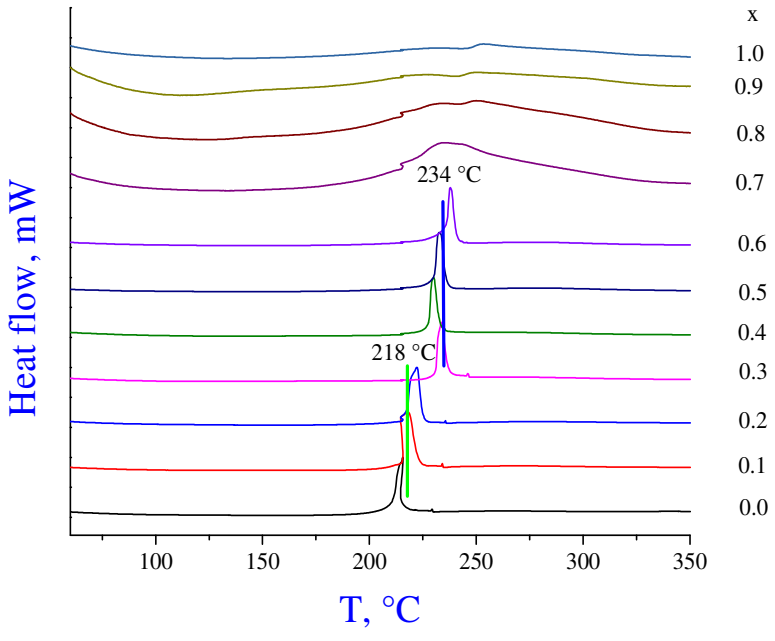

Figure IV-1: Characterization of decomposed organic residues by thermal analysis (DTA) of $Zr_xTi_{1-x}O_2$ nanoparticles with different elemental compositions $0 \leq x \leq 1$.

This structural transformation appeared to be sensitive to the elemental composition x of ZTOA species. Indeed, three groups of samples can be distinguished in Figure V-1: (x1) $0 \leq x \leq 0.2$ with relatively narrow exothermic peak at T = 218 °C, (x2) $0.3 \leq x \leq 0.6$ with relatively narrow exothermic peak at T = 234 °C and (x3) $0.7 \leq x \leq 1$ with an extremely broad double maxima exothermic peak in the temperature range between 225 and 255 °C and a inflection point at ~240 °C. These three groups can be perfectly identified in TGA curves of Figure V-2, where the sudden mass loss of groups x1 at 218 °C and x2 at 234 °C can be identified, while group x3 corresponds to a smooth variation of mass loss curves, which become flat at the DTA inflection point ~240 °C. The identified groups of the structural transformation, presented by equation IV-1, correlate with ZTOA particle radius evolution, R(x). Indeed as Figure III-22 in chapter 3 shows, particles size firstly increases with an increase of x>0 (x1), followed by a broad plateau, where it does almost not change (x2), and concluded by a decrease when x approaches 1 (x3). The exothermic peak around 250 °C has been previously observed during $TiZrO_4$ membranes preparation by sol-gel method and assigned to the decomposition of alkoxides and combustion of isopropanol [37]. We assumed in our study that the elimination of organics from the particle surface is connected to the strength of chemical bonds, which depend on the material nature and not particle size, since the size strongly changes in zones x1 and x2 while DTA peak positions and TGA curved do not. Then, the ZTOA particle size is not an independent parameter but also a consequence of the elemental composition.

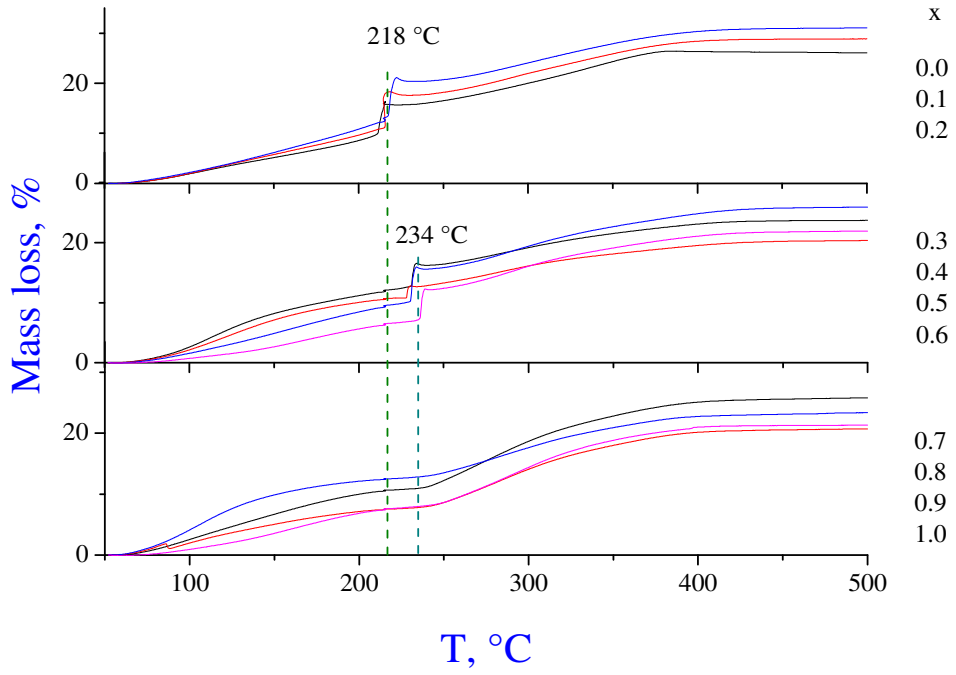

Figure IV-2: Thermogravimetric analysis (TGA) of $Zr_xTi_{1-x}O_2$ nanoparticles with different elemental compositions $0 \leq x \leq 1$.

In contrast to the low temperature peaks ($T \leq 250$ °C), the high temperature DTA peaks in Figure V-3 exhibit a strong variation with x, which has no straightforward correlation with the three material groups x1, x2 and x3. However, groups x1 and x2 are in the range of a strong variation $T_h(x)$ while group x3 is in the turning region with the maximum $T_h = 678$ °C at $x = 0.5$. In agreement with previous studies [37], pure TiO_2 ($x = 0$) and ZrO_2 ($x = 1$) metal oxides crystallize at the lowest temperatures of 378 and 387 °C, while an addition of the second element leads to a significant increase in the crystallization temperatures. According to Figure IV-2, this process terminates at temperatures ~400 °C and the high temperature DTA peaks are not accompanied by any significant mass loss. The general transitions from amorphous to crystalline are in IV-3.

$$amorphous - Zr_xTi_{1-x}O_2 \xrightarrow{T_h = 380-680\ ^\circ C} crystallin\,e - Zr_xTi_{1-x}O_2 \qquad \textit{Equation IV-2}$$

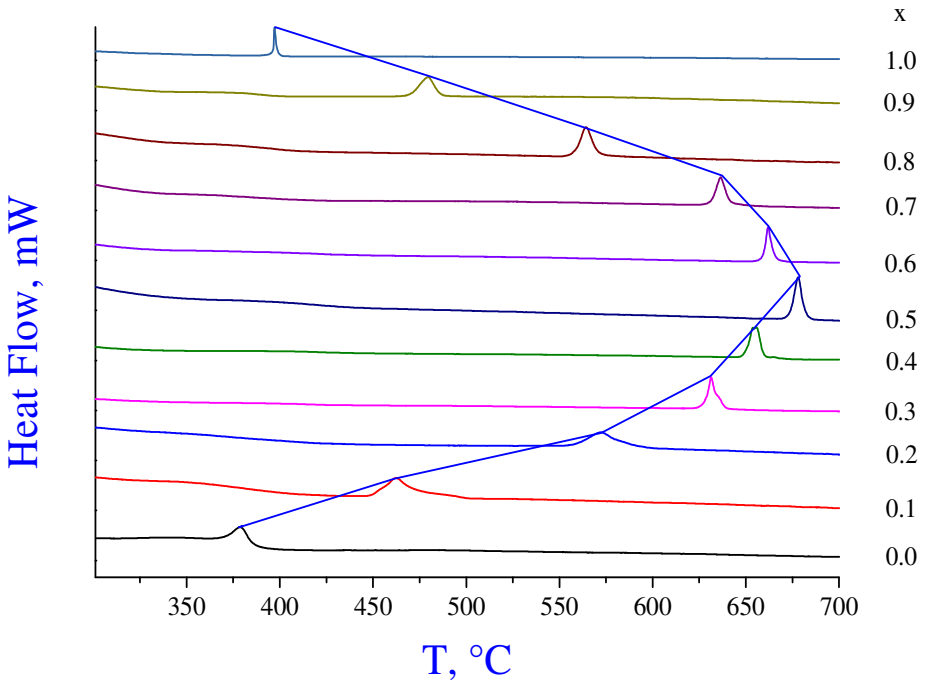

Figure IV-3: The characterization of crystalline transition temperatures by thermal analysis (DTA) of $Zr_xTi_{1-x}O_2$ nanoparticles with different elemental compositions $0 \leq x \leq 1$.

IV.2 X-ray diffraction analysis

From the investigations by thermal analysis DTA-TGA, the nano-powders materials were treated at the post transition temperatures for studies by X-ray diffraction. The selected calcinations are in table IV-1.

Table IV-1: The selected temperatures of each composition for mixed $Zr_xTi_{1-x}O_2$ to do calcinations

Compositions, x	0.0	0.1	0.2	0.3	0.4	0.5	0.6	0.7	0.8	0.9	1.0
$T_{calcination}$, °C	410	500	600	650	680	700	690	670	590	510	430

The analysis of the crystalline structure of $Zr_xTi_{1-x}O_2$ nanopowders was performed after XRD measurements of the heat treated samples at temperatures $T_h(x)$ obtained from the DTA data in Figure IV-3 and the detail temperatures are in table IV-1. The recorded XRD patterns are presented in Figure IV-4. The pure TiO_2 (x = 0) and ZrO_2 (x = 1)

materials were crystallized in respectively anatase and mixed monoclinic/tetragonal phases. By varying the elemental composition of $Zr_xTi_{1-x}O_2$, XRD peaks exhibit significant variation in position and intensity, indicating continuous deformation of the crystalline cell by insertion of Zr atoms into TiO_2 matrix. To rationalize these observations, after the careful determination of the Caglioti parameters using a standard LaB6 powder, Rietveld refinement was performed using MAUD (Material Analysis Using Diffraction) software [166]. The pattern fitting was performed using a standardized procedure, allowing a free variation of the respective amounts of each phase, and, considering the nonstoichiometric composition of some phases, the lattice parameters were considered as variables. The Crystallographic Information Files (CIF) were retrieved from the PDF4 database, using the file reference number 5000223 [167], 1008790 [168], 9009919 [169] and 1010912 [170] for anatase-TiO_2, orthorhombic $ZrTiO_4$, tetragonal ZrO_2 and monoclinic ZrO_2 respectively. Other phases (rutile TiO_2, brookite TiO_2, cubic ZrO_2, etc.) were also tried but zero volume fractions were always obtained. In a final step, to optimize the quality of the Rietveld pattern refinement and obtain the amounts of different phases, arbitrary texture option was used. The result of this fitting procedure on example of $Zr_{0.5}Ti_{0.5}O_2$ nanopowder is shown in Figure IV-5, which undoubtedly evidences the formation of the orthorhombic phase of $ZrTiO_4$. Despite an apparent continuity in the evolution of diffraction patterns in Figure IV-4 and large flexibility allowed in the Rietveld refinement due to a possible free evolution of both lattice parameters and texture, strong discontinuities revealed between anatase phase of TiO_2 for $0 \le x \le 0.2$, orthorhombic phase of $ZrTiO_4$ for $0.3 \le x \le 0.6$, and biphasic monoclinic/tetragonal ZrO_2 for $0.7 \le x \le 1$. Our analysis showed that the experimental patterns were not compatible with any mixture of phases neither in the Ti-rich nor in the Zr-rich regions.

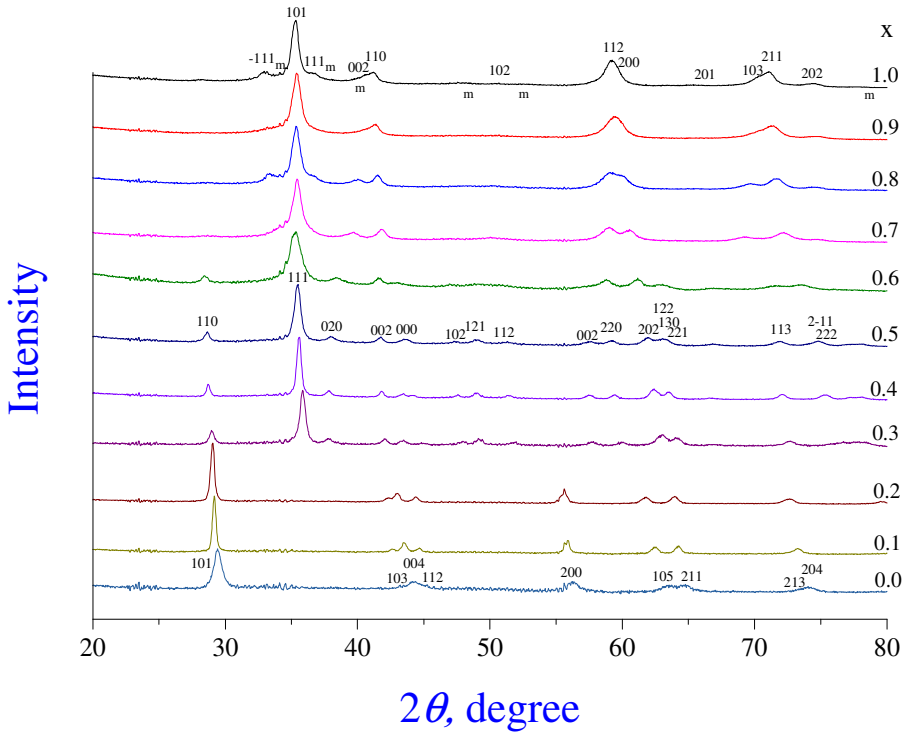

Figure IV-4: XRD patterns of $Zr_xTi_{1-x}O_2$ nanopowders with different elemental compositions $0 \leq x \leq 1$, heat treated at temperatures $T_h(x)$ of the exothermic peaks in DTA curves. The peaks of anatase, orthorhombic and tetragonal / monoclinic phases are respectively indexed in diffractograms x=0, x=0.5 and x=1 (peaks of monoclinic phase are complimentary labeled with m; the very weak peaks are only labeled).

Based on this modeling, the crystalline phase and cell parameters of prepared $Zr_xTi_{1-x}O_2$ materials were obtained as depicted in table IV-2. Consequently, XRD patterns in Figure IV-4 were assigned to different single phase materials:

- in the range $0 \leq x \leq 0.2$, anatase TiO_2 is preserved;
- in the range $0.3 \leq x \leq 0.6$, orthorhombic $Zr_xTi_{1-x}O_2$ appears;
- in the range $0.7 \leq x \leq 1$, mixed monoclinic and tetragonal ZrO_2 coexist with the percentage of tetragonal phase decreasing with an increase of x.

These composition domains of the appearance of these different phases perfectly fit those x1, x2 and x3 defined after DLS analysis of ZTOA nanoparticles in chapter 3 and DTA/TGA analysis of ZTOA nanopowders transformation to $Zr_xTi_{1-x}O_2$. We observed that by insertion of Zr atoms into TiO_2 host matrix, the crystalline cell progressively deforms by conserving the phase until it switch to a more stable structure. Consequently, anatase TiO_2

can adopt up to 20 % Zr atoms and monoclinic/tetragonal ZrO_2 can adopt up to 30 % Ti atoms in their respective structures. Pure orthorhombic phase of $Zr_xTi_{1-x}O_2$ appears to be stable in the broad range of compositions $0.3 \le x \le 0.6$. Our results suggest an important correction of the low temperature phase diagram earlier proposed by Xu et al. [157]: one has to extend the domain of the anatase TiO_2 phase stability and exclude single phase tetragonal ZrO_2 by including it into orthorhombic $Zr_xTi_{1-x}O_2$ phase stability domain. An extrapolation of the TiO_2-ZrO_2 phase diagram obtained at relatively high temperatures to low temperatures seems not to be straightforward because of the slow kinetics and starting material heterogeneity (TiO_2 and ZrO_2 powders) [171]. This underlines an importance of a careful design of the elaboration process and, more particularly, attracts attention to micromixing conditions in order to enable homogeneous elemental dispersion into the composite solids.

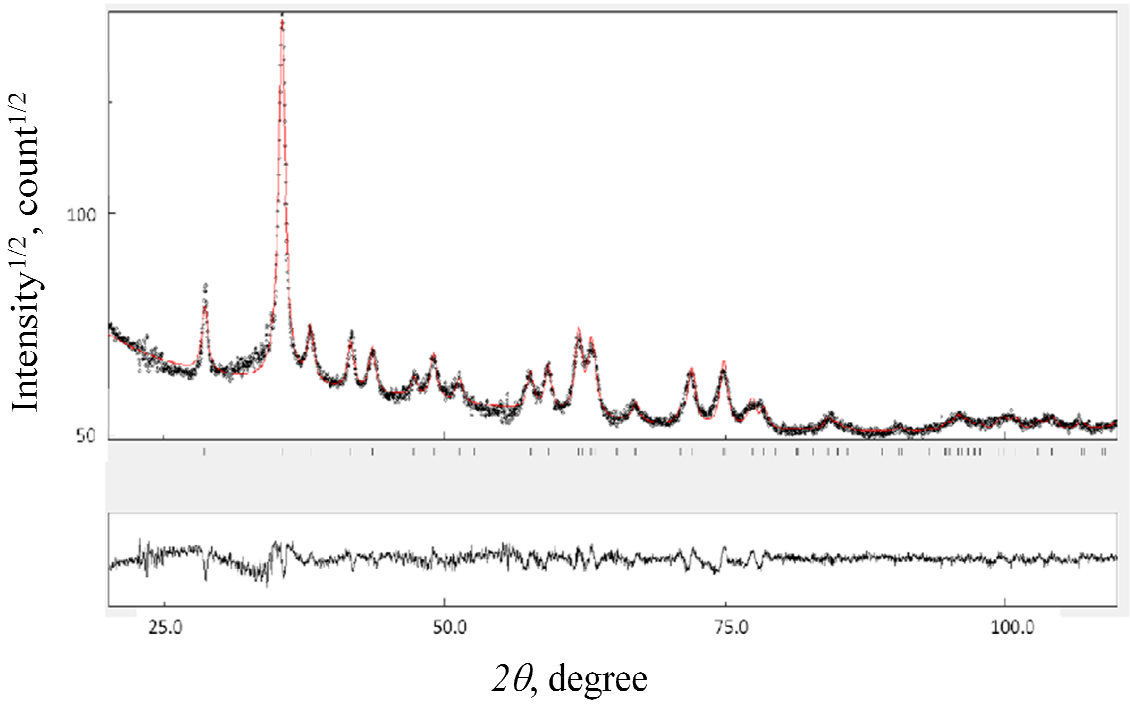

Figure IV-5: Least squares fit of XRD pattern of $Zr_{0.5}Ti_{0.5}O_2$ nanopowder with orthorhombic structure.

The crystalline cell size parameters of orthorhombic $Zr_xTi_{1-x}O_2$ vary with x, as shown in table IV-2. At the same time, we can conclude that our cell parameters obtained for x = 0.5 composition: a = 4.8103 Å, b = 5.4919 Å and c = 5.0291 Å (table IV-2) are in a good agreement with earlier published results. Indeed, the crystalline cell parameters of $ZrTiO_4$ orthorhombic structure with the space group Pnab (no. 60) have been previously

reported in number of works: *a* = 4.80 Å, *b* = 5.49 Å and *c* = 5.03 Å [172], *a* = 4.8042(2) Å, *b* = 5.4825(3) Å, *c* = 5.0313(2) Å [168] or *a* = 4.8087(1) Å, *b* = 5.3630(1) Å and *c* = 5.0301(1) Å [173]. The sensitivity of solid solutions to the compositional heterogeneity and difficulties of obtaining the elemental homogeneity low temperature synthesis, may account for some discrepancy in the earlier reported data. On the other hand in the high temperature domain, Troitzsch et al [174] have reported on the orthorhombic cell parameters increase with x with the values at x = 0.5: *a* = 4.8069(2) Å, *b* = 5.4785(2) Å, *c* = 5.0339(2) Å and cell volume 132.57 $Å^3$, which obviously agree with our data and V = 132.85 $Å^3$. One has to be careful by comparing high and low temperature data since pure single-metal oxide phases are not the same (e.g. rutile against anatase in TiO_2).

Table IV-2: The crystalline parameters, phase transitions and sizes of different composites $Zr_xTi_{1-x}O_2$

		TiO_2 anatase			$Zr_xTi_{1-x}O_2$ orthorhombic			
Compositions, x		0.0	0.1	0.2	0.3	0.4	0.5	0.6
Crystalline parameters	a	3.791	3.819	3.833	4.683	4.760	4.810	4.900
	b	3.791	3.819	3.833	5.524	5.523	5.492	5.433
	c	9.603	9.655	9.774	4.996	5.017	5.029	5.044
	Size, nm	20	52	42	27	39	23	12

		ZrO_2							
		Tetragonal				Monoclinic			
Compositions, x		0.7	0.8	0.9	1.0	0.7	0.8	0.9	1.0
Crystalline parameters	%	85.0	83.2	85.2	71.2	15.0	16.8	14.8	28.9
	a	3.545	3.573	3.587	3.601	4.964	5.105	5.148	5.189
	b	3.545	3.573	3.587	3.601	5.485	5.293	5.195	5.126
	c	5.263	5.215	5.171	5.175	5.220	5.331	5.291	5.339
	beta					86.64	84.62	84.72	80.94
	Size, nm	13	14	14	19	17	8	12	10

According to table IV-2, the cell parameters of all crystalline phases exhibited a regular modification, when Zr progressively replaces Ti in the oxide matrix. In TiO_2, both parameters *a* and *b* increase with an increase of x. In $Zr_xTi_{1-x}O_2$, *a* parameter increases strongly while *c* parameter increases barely and *b* parameter decreases. The distortion also appears in ZrO_2 phases with the increase of two parameters (*a* and *c* for tetragonal and *a* and *b* for monoclinic zirconia) and decrease of the third parameter (*b* for tetragonal and *c* for monoclinic zirconia). Despite of these complex modifications, the crystalline cell volumes increase with x for each of the observed phases, as shown in Figure IV-6. In case of the mixed tetragonal and monoclinic phases ($x \geq 0.7$), the weighted average of monoclinic and

tetragonal phases was used as a representative of the $Zr_xTi_{1-x}O_2$ cell evolution. This global increase of the lattice volume is apparently connected to a greater size of the substitutional element Zr^{2+}, which is 86 pm against 74.5 pm for Ti^{2+}. As for the crystalline grain size (see table IV-2), no significant trend can be found within each of the three x domains. We however notice its progressive decrease from one domain to the next one, with an average diameter of 38 nm for anatase TiO_2, 25 nm for orthorhombic $ZrTiO_4$ and 15 and 12 nm for respectively tetragonal and monoclinic ZrO_2.

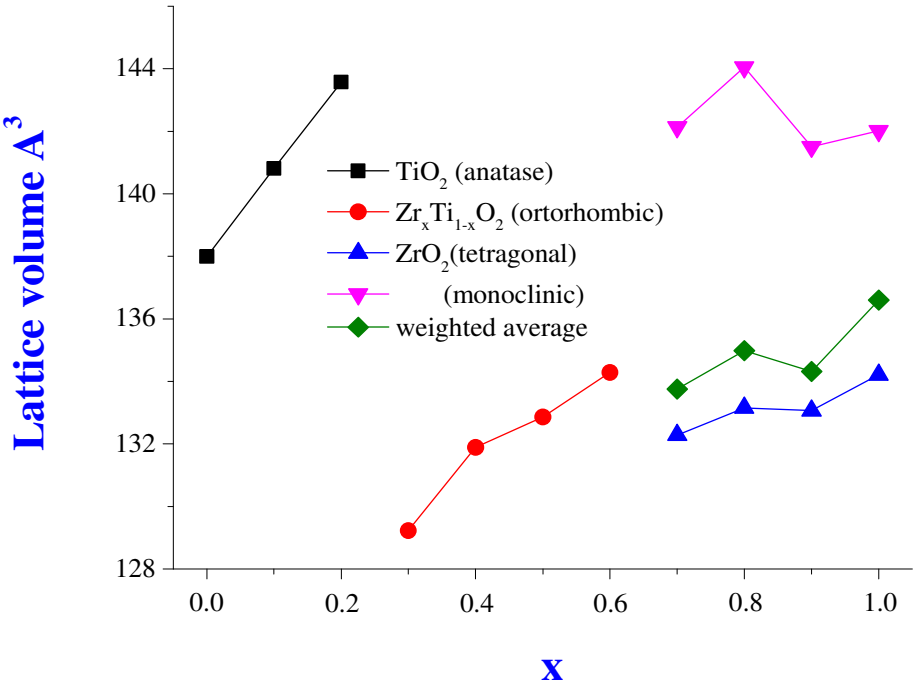

Figure IV-6: Lattice volumes (A^3) in different phases and compositions of crystalline $Zr_xTi_{1-x}O_2$ nanoparticle.(The lattice volume of t-$Zr_xTi_{1-x}O_2$ were multiplied by 2 due to this compound containing two metal elements).

Based on the above discussion of structural transformations ZTOA → $Zr_xTi_{1-x}O_2$, we conclude that the elemental composition x of a ZTOA nucleus accounts for a profound modification of the material electronic structure, which defines the particles size, strength of the surface bonds and crystalline structure of the final material $Zr_xTi_{1-x}O_2$. As a result of the homogeneous dispersion of titanium and zirconium elements at the atomic level, single-phase solid scan be obtained.

IV.3 TEM analysis

The TEM analysis of $Zr_xTi_{1-x}O_2$ nanopowders confirms homogeneous elemental distribution of Zr and Ti elements at nanoscale. The first example of the mixed oxide material with x = 0.5 after the heat treatment at 680 °C is shown in Figure IV-7. The energy filtered TEM images of Ti (d) and Zr (e) maps perfectly recover in the area of the relevant material absorbance (c). An interesting result concerns the nanoscale morphology of the calcined powders. In fact, the powder consists of well crystallized particles with size ~100 nm as shows Figure IV-7a. This particle is a monocrystal and, after a proper alignment, crystalline planes with the interplane distance d = 0.27 nm can be observed in Figure IV-7b. The electron diffraction pattern, given in inset of Figure IV-7b, supports this conclusion about the monocrystalline character of particles. At the same time, inset in Figure IV-7b evidences nanoporosity of the particles, with the mean pore size about 4 nm. We believe that the reason of this phenomenon lies in the monodispersed nature of the original ZTOA nanoparticles that compose the powder. Indeed, the crystallization is a kinetically rapid process and it begins in the contact area between particles in a powder, in contrast to single nanoparticles [175]. For temperatures close to the phase transition onset, the nucleation frequency of a new phase is sufficiently low, which favors initiation of crystallization of an aggregate from one constituting nanoparticle. In these conditions, the crystallization can expand all over the aggregate making the first nucleus a template for the new phase growth resulting in the formation of a monocrystal. The statistical analysis of TEM images showed that some submicronic nanoparticles may consist of more than one monocrystal. This can be explained by fluctuations resulting in instantaneous appearance of two and more nucleus of a new phase in the same aggregate. In such case of the multiple nucleations, several centers of a new phase growth would lead to a polycrystalline particle. We assume that in our calcined powders, the mean particles size of ~100 nm favours single nucleation site of a new phase.

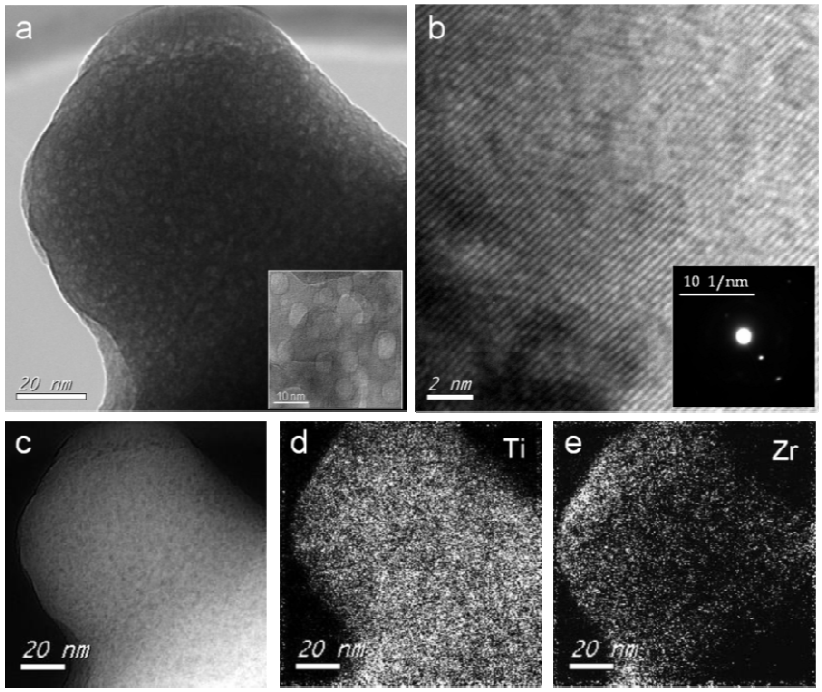

Figure IV-7: TEM image (a, b), electron absorption (c), elemental mapping of Ti (d) and Zr (e) and electron diffraction (inset b) of $Zr_{0.5}Ti_{0.5}O_2$ nanoparticles.

We have performed an analysis of the amorphous material. The image are shown in Figure IV-8a together with Ti and Zr mapping (Figure IV-8b and c) and electron diffractions pattern (Figure IV-8d).

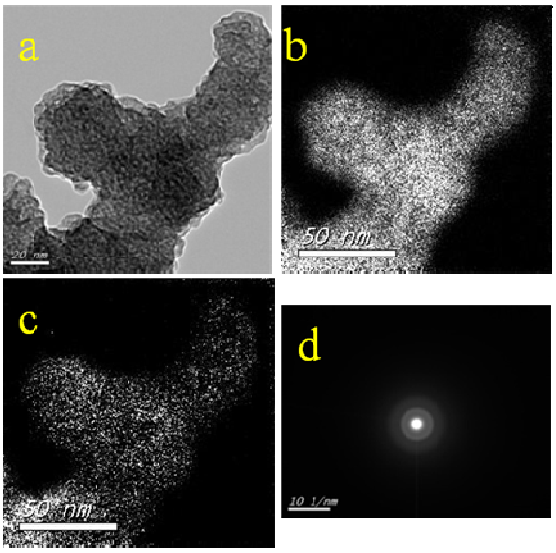

Figure IV-8: The amorphous of mixing Zr and Ti at x = 0.5 (a) image, (b) maping Ti (c) maping Zr and (d) diffraction.

In order to additionally validate the preparation method, we performed a comparison of the composition x: imposed by the synthesis conditions (EXP) and obtained from EFTEM measurements of the precipitated ZTOA and crystallised $Zr_xTi_{1-x}O_2$ materials, as shown in Figure IV-9. We obtained that xsyn = xEFTEM by analysing ZTOA materials, while a dispersion of xEFTEM data takes place in the crystallised $Zr_xTi_{1-x}O_2$ materials for elemental compositions $0.4 \leq x \leq 0.7$. Since the new orthorhombic phase appears the same range of x, the smaller Zr content in the crystallised material may be related to the stability of the respective solid solutions.

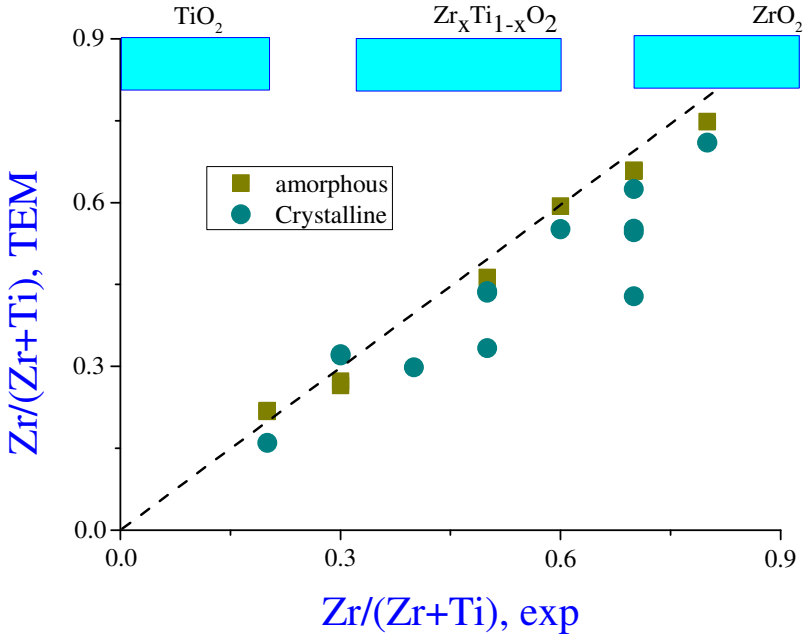

Figure IV-9: The comparison the compositions from experimental with EELS of TEM results.

IV.4 ICP-OES analysis

Preparation for analysis: The amorphous powders were balanced and then dissolved in concentrated nitric acid with heat at 60 °C for one hour. The solutions were diluted with distillated water by keeping nitric concentration around 6 M. The diluted samples (between 1 to 10 ppm) were kept elements (Zr and Ti) concentrations in the range of standard solution and LOD of instrument.

Results: The complementary analysis of macroscopic samples with a mass ~2 mg obviously evidenced an excellent agreement between the final material and its synthesis conditions. For example, ICP measurements of $Zr_xTi_{1-x}O_2$ nanopowders prepared with x = 0.30, 0.50 and 0.70 respectively provided x_{ICP} = 0.30, 0.48 and 0.68. We concluded that small deviations of the local elemental composition from the bulk average may exist in the domain of the orthorhombic solid solutions.

IV.5 Band gap energy measurements

In view of a smooth variation of the crystalline structure with composition x, one can expect a smooth variation of the electronic band structure of the prepared mixed metal oxide materials. Such variation opens a way to band gap engineering that serve to be an important element of possible applications in photocatalytic [13]. In the present work, we measured absorption spectra of the prepared $Zr_xTi_{1-x}O_2$ composites in a broad composition range $0 \leq x \leq 1$. The quartz plates transparent in the UV spectral range unto 200 nm, were dip coated with monodispersed ZTOA colloids, dried and calcinated at temperatures slightly above the crystallization onset obtained from TGA/DTA measurements in Figure IV-3. The photos of plates before after coated films are shown in Figure IV-10. The film thickness was about 100 nm. The absorption spectra of the prepared coatings on quartz plates were measured using Jasco V-660 double-beam spectrophotometer in the Institute of Physics of Tartu University. The band gap energy was obtained from Tauc plot for direct allowed transitions.

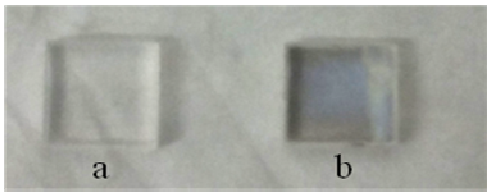

Figure IV-10: The photos of quartz (a) before and (b) after coating (with calcinations) with ZTOA.

The observed band gap enetgies of $Zr_xTi_{1-x}O_2$ films of different compositions x are shown in Figure IV-11. The lowest energy 3.14 eV (x=0) corresponds to that of anatase titanium dioxide and the highest one 5.4 eV (x=1) to zirconium dioxide.

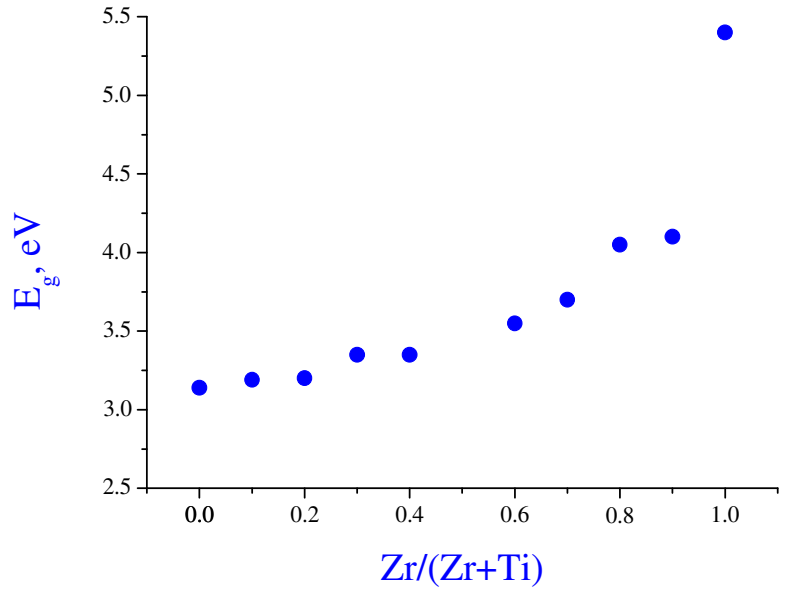

Figure IV-11: Band gaps of different compositions of composite $Zr_xTi_{1-x}O_2$.

The energy evolution with x looks indeed continuous. However, we can notice some peculiarities of this evolution. (i) Band gap drops down quickly from 5.4 to to 3.7 eV with a small Ti element addition to ZrO_2 matrix ($0.7 \leq x \leq 1$). (ii) There is no significant variation of band gap energy with a small addition of Zr element to TiO_2 matrix ($0 \leq x \leq 0.2$): the measured energies are 3.14, 3.19 and 3.2 respectively for x = 0, 0.1 and 0.2. (iii) There is a smooth variation of the energy in the range of intermediate compositions $0.3 \leq x \leq 0.6$. Taking into account our structural analysis of the prepared material (Chapter IV-2), one can conclude about stable band gap energy of anatase TiO_2 despite of the substantial crystalline cell deformation by Zr insertion (see Table IV-2 and Figure IV-6). These materials can be considered for photocatalysis applications under UVA light illumination.

IV.6 Specific surface area (BET)

The measured specific surface area of $Zr_xTi_{1-x}O_2$ crystalline solids is shown in Figure IV-12. The nanopowders were well crystallized after the heat treatment at temperatures slightly above that of the DTA exothermic peak in Figure IV-3, as confirmed by TEM and X-ray diffraction analyses. The surface area strongly increased after adding a small amount of zirconium element and attains a maximum at x = 0.05, after which it decreased reaching a plateau at $x \geq 0.5$. We notice that BET surface area 25 m^2/g of pure TiO_2 nanopowders was

different from that in our previous studies ~50 m^2/g. This may be related to different solvents (n-propanol vs iso-propanol) and heat treatments. A low specific surface area of the heat treated ZOA nanopowders has been previously reported [160]. This effect does not concern polydispersed nanoparticles and was observed only in monodispersed nanoparticles. It has been explained by a strong surface retention of carbonaceous species that induces the particles sintering at heat treatment, thus reducing the surface area. This effect may also concern mixed-oxide $Zr_xTi_{1-x}O_2$ nanopowders with a high Zr content.

.

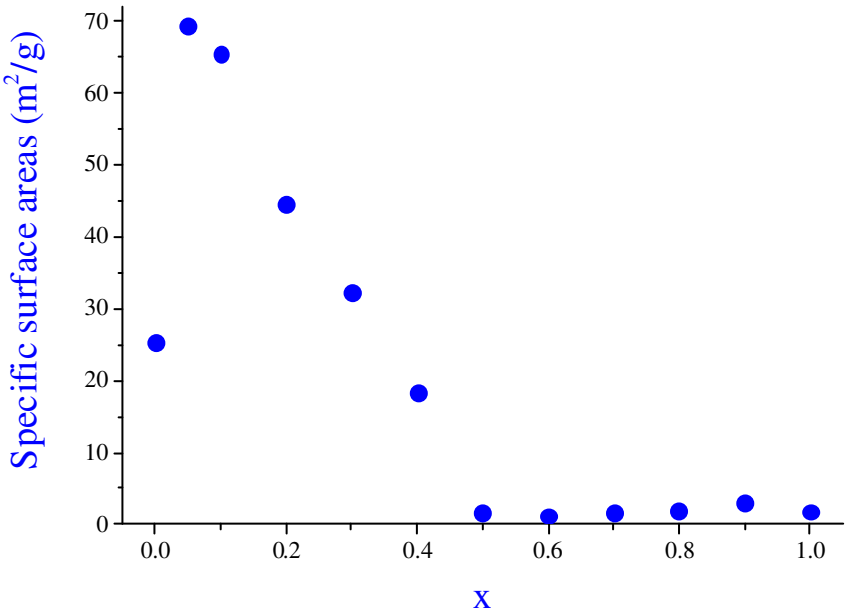

Figure IV-12: Specific surface areas (BET) of nanoparticulate $Zr_xTi_{1-x}O_2$ solids ($0 \leq x \leq 1$).

BET surface area of mixed ZrO_2-TiO_2 materials of different compositions has been measured previously and often peaked at the composition x = 0.5 [18-20, 38, 40, 176-178], which however belong to not well or non crystalline materials. Indeed, the heat treatment were done at temperatures lower than that of the amorphous-crystalline 650 °C (according to thermal (DTA) and X-ray diffraction analyses): e.g. 400 °C [18], 402 °C [176], 500 °C [38] or 550 °C [19, 20]. To get well crystalline all compositions should be done calcinations the same as table IV-1. Zou et al [40] have found the highest surface area at x = 0.5 of this binary oxides heat treated at 450 °C (amorphous) and 800 °C (crystalline); however, the homogenous materials were not confirmed in this study. Other compositions with the highest BET surface have been reported: x = 0.25 at 500 °C [51] and x = 1 at 600 °C [74].

Finally, a smaller zirconium content than titanium has been also reported to result in an increased BET surface: e.g. 5% ZrO_2 - 95% TiO_2 (x = 0.05) [24, 25, 118]. These last findings are similar to our measurements in this work. This large discrepancy of the obtained results can be attributed to different material preparation conditions.

IV.7 Conclusion

We applied the micromixing technique to nucleate monodispersed mixed metal oxides oxo-alkoxy nanoparticles ZTOA of different elemental compositions $0 \le x = C_{Zr} / (C_{Zr} + C_{Ti}) \le 1$ and, on this base prepared $Zr_xTi_{1-x}O_2$ crystalline solid, which conserve the highly homogeneous elemental dispersion of the original ZTOA nanoparticles.

The structural transformation of the nanoparticles takes place in two temperatures ranges: 210-250 °C and 380-680 °C, which sensitively depends on the elemental composition. The crystallization temperature of ZTOA nanopowders attains its maximum of 680 °C at x = 0.5 and decreases with either following increase or decrease of x.

The obtained crystalline materials were assigned to three different single phase materials: for $0 \le x \le 0.2$, anatase TiO_2 is preserved, for $0.3 \le x \le 0.6$, orthorhombic $Zr_xTi_{1-x}O_2$ appears and for $0.7 \le x \le 1$, mixed monoclinic and tetragonal phases of ZrO_2 coexist. The crystalline cell size of all three phases underwent a continuous variation with x and the cell volumes increased with x in agreement with the larger size of the substitution ion Zr^{2+} compared to host Ti^{2+}. The TEM images evidenced the nanoporous structure of the submicronic mixed oxide monocrystals with the mean pore size about that of ZTOA nanoparticle. Based on these results, we conclude that the elemental composition x induces a profound modification of the material electronic structure, which defines the size of ZTOA nuclei, strength of the surface bonds and crystalline structure of the final material $Zr_xTi_{1-x}O_2$. As a result, single-phase solids can be obtained after homogeneous mixing of titanium and zirconium elements at the atomic level.

In agreement with structural modifications, the band gap energy of the composite materials increased continuously with x starting from 3.14 eV for $x = 0$ (100% Ti) to 5.4 eV for $x = 1$ (100% Zr). Most strong band gap variation from 5.4 to 4.1 eV takes place at a small ~10% addition of Ti element in zirconia. In contrast, at a small Zr element addition ≤20%, no appreciably modification of the band gap energy was observed. The specific

surface area (BET) of crystalline nanopowders attains a maximum at x=0.05 and decreases with the following increase of x.

The measurements of band gap energy and specific surface area suggest considering $Zr_xTi_{1-x}O_2$ nanoparticulate coatings with compositions $0 \leq x \leq 0.2$ for applications in photocaralysis under UVA light illumination.

Notation

ZTOA	zirconium titanium oxo-alkoxide
TGA	thermogravimetric analysis
DTA	differential thermal analysis
ICP-OES	inductively coupled plasma-optical emission spectroscopy
TEM	transmission electron spectroscopy
XRD	x-ray diffraction
BET	Brunauer–Emmett–Teller
DTA	differential thermal analysis
DLS	dynamic light scattering
T_l	low temperature (°C)
T_h	high temperature (°C)
T	temperature (°C)
θ	angle (°)
a, b and *c*	crystalline parameters (Å)
LOD	limit of detection
t-	tetragonal
ppm	part per million
Symbols	
λ	wavelength (nm or Å)

Chapter V: Photocatalytic activity of $Zr_xTi_{1-x}O_2$ nanocoatings and powders

This chapter will be discussed about photocatalytic applications of mixed composite $Zr_xTi_{1-x}O_2$ by using micromixing reactor with producing monodisperse nanaoparticles and high homogenous composite. It will be described about the general procedures of preparing and coating process, photocatalysis procedures, photocatalysis activity of different compositions and calcinations, the influence photocatalysis activity by lamps powers and x-ray diffraction results. The real amount of coating and compositions were also analyzed by ICP-OES. The ethylene was chosen as pollutant in gaseous phase, and methylene blue and phenol were chosen as pollutants liquid phases.

V.1 Introduction

TiO_2 have been known and used in past decades to do photocatalyst for water and air purification because it is low cost, long time stability in the photocatalysis process and safety material [127, 179]. Moreover, to improve the catalysis and photocatalytic activities, the composites of TiO_2 mixed with other oxides and doping with some foreign metal ions have been interested so far [13], e.g, the photocatalytic activity was better than pure TiO_2 when it was mixed with ZrO_2 [131] and doped with iron in our team recently [128].

Normally, the factors that are considered to account for the improved photocatalytic activity of binary oxide nanoparticles TiO_2–ZrO_2 over pure ZrO_2 and TiO_2 are; the high surface area, high content of anatase phase TiO_2 and monoclinic phase of ZrO_2, small particle size, the presence of high OH groups [74] and the stronger adsorption in the ultraviolet region [139]. Another factor should be from recombination of electrons and holes. It was confirmed that adding some small amount ZrO_2 to TiO_2 could be increased the time of recombination between electrons and holes from 15.94 ms for pure TiO_2 to 21.69 ms for mixed ZrO_2-TiO_2 [180]. If it is true all the compositions, this would be another important factor of improving photocatalysis activity from this composite and it may have activity strong or weak depending on the compositions of each element contents. As an example, the enhanced photocatalyst activity of composite titanium-zirconium oxides ($Ti_xZr_{1-x}O_2$) was recently believed from the lower rate of charge recombination electron and hole after photoinduced [66]. For heterogeneous composite ZrO_2-TiO_2, one of those factors that are believed to improve photocatlysts is that the electron transfer from the surface states of ZrO_2 to CB of TiO_2, which acts as electron trap lowers the photogenerated charges recombination, demonstrating mechanism by Neppolian et al [57] as Figure I-25 in the introduction chapter, leading to an enhancement of the photocatalytic activity of this

composite. However, it is possible to change the composition and mechanism or better quality activity in case that the materials are at high homogenous level. As an experience, we found that the amount iron doping into TiO_2 in high homogeneity by using micromixing reactor to be improved photocatalysts was very different from other methods [128].

There were some researches about photocatalysis degradation the pollutants from mixed TiO_2-ZrO_2 but there was no documentaries so far about this monodispersed and homogenous composite that was well investigated at the beginning by sol-gel method. The difficulties for mixed TiO_2-ZrO_2 to prepare photocatalysts with high efficiency caused by: inhomogeneity, agglomeration of particles and rapid photogenerated charges recombination. One method used to minimize these phenomena is to prepare this hybrid photocatalyst from quasi monodisperse nanoparticles by using microreactor**,** which produces more homogenous materials than other methods. The microreactor involves in injecting the reagents through a T-mixer, which is the point-like reaction conditions in the regime of low Damköhler numbers, with the environmental temperature and gas control and in very short time, in the timescale less than ten milliseconds [110]. This is allowed to obtain the homogeneous composites with high homogeneity quasi-mono-dispersed particles and would be better in photocatalytic applications compared to traditional manual methods. Therefore, using micromixing reactor to mix this composite with monodispersity at the beginning and high homogeneity would be interested to be investigated for factors to improve photocatalysis activity.

In the photocataltic benefit of researching so far, the mixed composite TiO_2–ZrO_2 could be used to decompose trichloroethylene [54], VOCs removal, oxidation of methylcyclohexane [181] and acetone vapors [55, 182], removal of methyl orange [56, 183], degradation of 4-chlorophenol [57, 184], degradation of methylene blue [138, 185-187] and water spitting [14], degradation of formaldehyde [137], photodegradation of ethylene [130, 188] and trichloromethane [133], photocatalytic oxidation ethylene [189], degradation NO_x [51], degradation of *p*-chlorophenol [139], photooxidation of salicylic acid and photoreduction of Cr(VI) [190], photodegradation of phenoxyacetic acid, 2,4-dichlorophenoxyacetic acid and 4-chlorophenol [191], ethanol photo-oxidation [132], elimination of methanol [192], degradation of paraquat dichloride [193], degradation rhodamine B (RhB) [72, 134, 135, 140, 187, 194, 195], decomposing alizarin cyanine green (ACG) [196], oxidation of aliphatic alcohols [197], for treatment of olive mill wastewater

[198], removal methyl orange [199], photodecomposition of salicylic acid and 2-chlorophenol [67], resazurin redox dye [200], treatment of textile effluent [201], degradation of pesticide quinalphos [202], reduction of 4-nitro-phenol to 4-aminophenol [203] and degradation of azo-dye[204] and dyes [205] etc. In those photocatalysis activities, some finding of this composite was improved the photocatalysis activity in efficiency as examples in refs [67, 68, 130, 133, 137, 200]. In case of study geometries from this composite, the activity of degradation rates depended on the geometries of material in the order: fiber < film < network < powder [183].

Recently, we were just succeeded to be well mixed composite $Zr_xTi_{1-x}O_2$ all serous eleven compositions [206]. The materials were mono-dispersed as the ZTOA particles in the nucleation stages of the aqueous phase and high homogenous materials in the solid phase. The anatase form of this composite was kept at the compositions of x = 0.0-0.2, which is considered as photocatalysis domain to be further investigated for the application.

In this part, we report about the enhanced photocatalysis activities of mixed nano-composite $Zr_xTi_{1-x}O_2$ from micromixing reactor, which can produce mono-dispersed materials and high homogenous to well decompose ethylene pollutant in gas phase. In the optimum of composition $Zr_{0.0425}Ti_{0.9575}O_2$ with optimum calcinations, which is high BET surface area and porosity material, the activity of photocatalyst was improved up to two times compared to pure TiO_2.

V.2 Experimental setup

V.2.1 Photocatalyst preparation

The prepared and coated composite $Zr_xTi_{1-x}O_2$ on borosilicate beads were carried out in modifying from ref [207]. For pre-prepared photocatalysis experiment, the borosilicate glass beads with 1 mm diameter were put and kept in concentrated sulfuric acid (95-98%) over night and then filtered to remove acid and cleaned with distilled water until pH almost 7. After that they were well dried in the oven (at 8O °C around overnight). These dried borosilicate glass beads were coated in 10 min (very slow stirring with spatula in few cycles at the minute 3 th and 6 th) with colloidal particles after the solutions had been mixed by micromixing reactor around 5 min. The coated beads were filtered with filter papers and dried with flowing nitrogen gas around 0.1 bars to prevent of moistures and oxygen molecules penetrating into the films of alkoxide oxo-composite. The whole procedure of the

process from mixing to calcinations is shown in Figure V-1. The films of mixed oxo-composite on beads were done calcinations in 4 hours at different temperatures between 400 and 650 °C from 50°C by rate 2°C/min. The calcinations were carried out in the furnace that allowed air flowing.

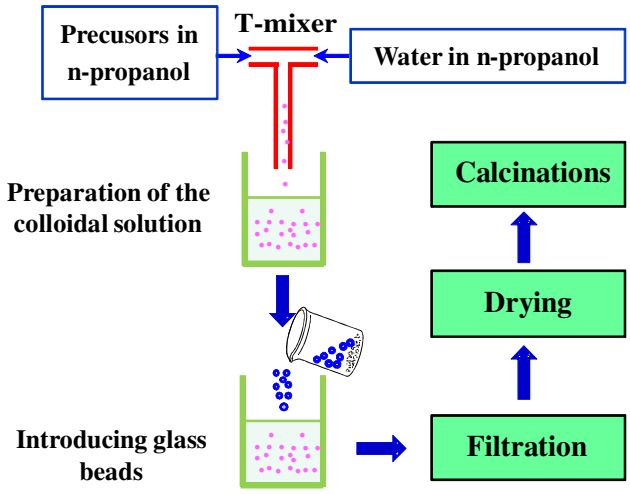

Figure V-1: Diagram of the coated beads with mixed oxo-nanocoposite $Zr_xTi_{1-x}O_2$ and treatment process.

The selected compositions of x = 0.0-0.2 for photocatalysis activities were decided from pictures of monodispered particle sizes in titanium domains measuring by dynamic light scattering, phase transitions of crystalline anatase by X-ray diffractions and thermal treatments, band gaps measurements, high homogenous materials by TEM [206] and high BET surface areas. From the range of selected compositions, they were chosen by double increased concentrations of zirconium content into anatase titanium oxide by x = 0.000, 0.025, 0.050, 0.100 and 0.200 for preparations. The real compositions and amounts of nano-composite on coated borosilicate beads are possible to be the same or differences from what they were prepared and depending on how the homogeneity of materials was. To know well how homogenous they were and the amount of each composition, all oxo-nanoparticles $Zr_xTi_{1-x}O_2$ films on beads were digested with concentrated nitric acid and then analyzed by ICP-OES.

V.2.2 Photocatalytic process

The general photocatalytic experiments to evaluate the activity of nano-composite $Zr_xTi_{1-x}O_2$ were carried out in the same as diagram in Figure V-2. In short, the percentages of mixing gas in tubes were controlled by MFC1 and MFC2 for air and ethylene (the initial concentration was 300 ppm) respectively. They were mixed and homogenized at mixer and then allowed to pass through the chromatography oven and then photoreactor. After the degradation in the photoreactor, the ethylene pollutant was analyzed by Gas Chromatography-Flame Ionization Detector (GC-FID).

GC-FID conditions:

- Oven temperature : 50 °C
- Injector temperature : 225 °C (with spit mode injection)
- Detector temperature : 300 °C
- Column : Zebron capillary GC column, ZB-624 programming at 50 °C
- Mobile phase : Nitrogen gas carrier with hydrogen supported detector

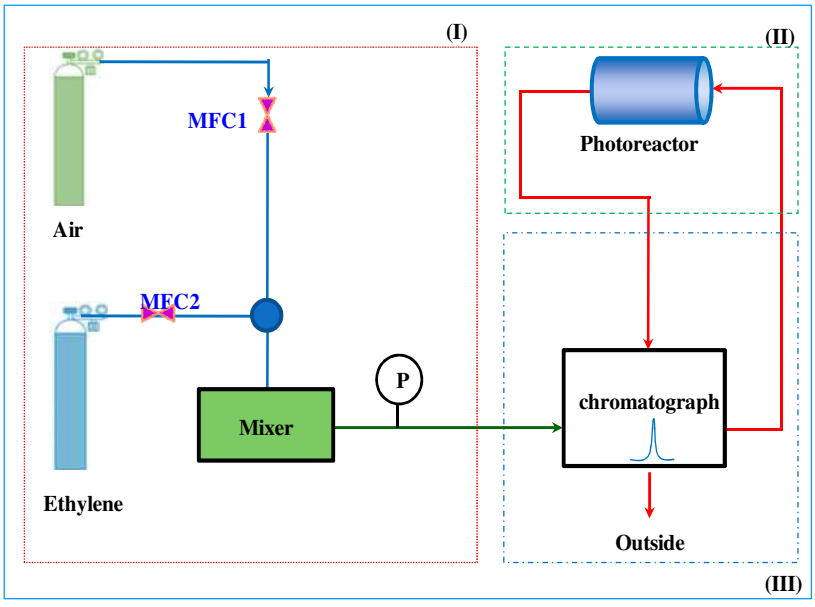

Figure V-2: Diagram of photocatalytic process of decomposing ethylene by $Zr_xTi_{1-x}O_2$ materials [101].

V.2.3 Photocatalytic reactor

The bed reactor that was made and set up in the laboratory with allowing continuous gas flow was used to be carried out to do the photocatalytic investigations [208]. The UVA-lamp irradiation conditions with the reactor 6 mm diameter tube surrounding from two to six lamps of each 8-W emitting at λ = 362 ± 11 nm in the well organized reactor geometry were used to decompose the pollutant. The geometry of bed photocatalysis reactor for set up the lamps is in Figure V-3a and the result of light measurement is in Figure V-3b.

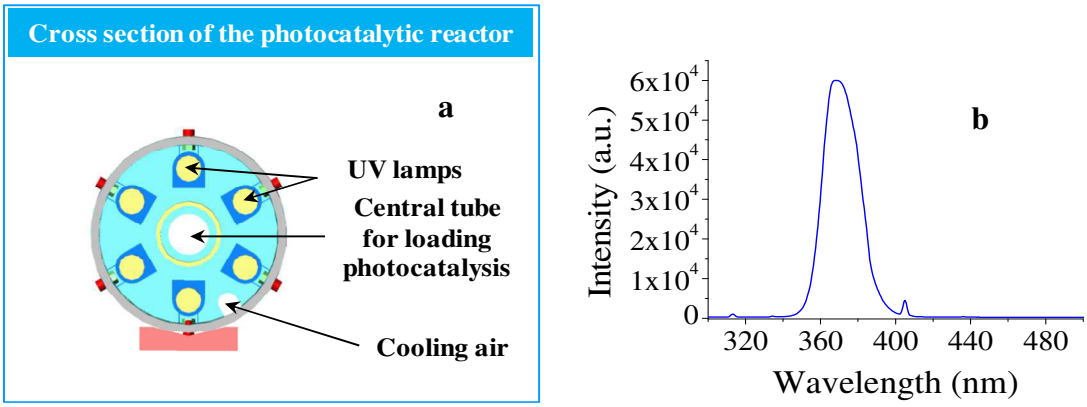

*Figure V-3: (**a**)UV lamps preparations for controlling photocatalytic application and (**b**) Intensity of the lamps being used to do photocatalyst with the best irradiations of 362±11 nm [101].*

A model pollutant ethylene had the concentrations between 60 to 300 ppm in air (containing 20% of O_2 and 80% of N_2). The flow rate of the mixed pollutant with air to change concentrations of ethylene was fixed at the flow rate of 75 mL/min through 5 cm coated borosilicate glass beads coating by the films of mixed composite $Zr_xTi_{1-x}O_2$. Gas chromatography (Varian CP 3800) – flame ionization detector (FID) was used to analyze this sample by namely C_{in} for before and C_{out} for after the photocatalytic reactor. This GC-FID was equipped with two injection loops that allowed doing in continuous mode measurements. For the yield of ethylene decomposition, it was calculated by the formula: $\eta(\%) = \left(C_{in} - C_{out} / C_{in} \right) \times 100\,\%$. The general procedure of photocatalysis experiments is in the Figure V-2 and beads in bed reactor are in Figure V-4.

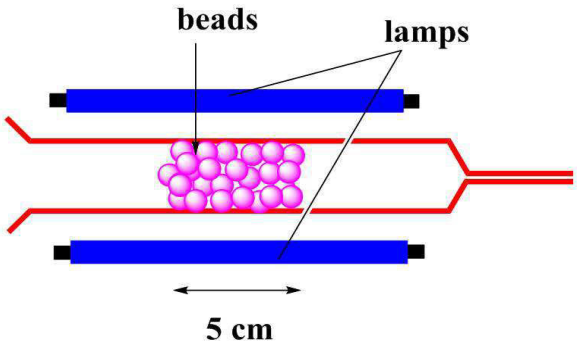

Figure V-4: Representative of prepared beads in the photocatalysis bed reactor.

The photocatalyst activity can be expressed as $\ln(C_{in}/C_{out})$, which is valid in case of first order reaction kinetics. Indeed, by integrating over the reactor volume V_0 the right and left parts of the usual differential equation describing the evolution of the pollutant concentration

$$\frac{dC}{dt} = -KC \qquad \textit{Equation V-1}$$

we can obtain respectively (standard rate definition)

$$Rate = \int_{V_0} \frac{dC}{dt} dV = \int_{V_0} dC \cdot v \cdot S = W(C_{in} - C_{out}) \qquad \textit{Equation V-2}$$

and

$$\int_{V_0} KCdV = K\int_{V_0} CdV = KN_0 \qquad \textit{Equation V-3}$$

where N_0 is the total number of the remaining pollutant molecules in the reactor volume. We than obtain

$$Rate = KN_0 \qquad \textit{Equation V-4}$$

On the other hand, known solution of equation V-1 is

$$\ln\left(\frac{C_{in}}{C_{out}}\right) = K\tau \qquad \textit{Equation V-5}$$

where τ is the pollutant residence time in the continuous-flow reactor. Equation V-4 shows an equivalence of both approaches. In the same time, using equation V-5 directly addresses the material activity, while *Rate* in equation V-2 addresses the photocatalytic reactor performance. Indeed, when C_{out} becomes small compared to C_{in} the left part of equation V-4 saturates in agreement with equation V-2, which does not allow comparing performances of

the effective photocatalysts. Consequently, the activity of the pollutant decomposition, $\ln(C_{in}/C_{out})$, was used in this work to compare photocatalysts with different elemental compositions x, providing the reactor geometry, lamp intensity and pollutant residence time were kept constant.

V.3 Results and discussion

V.3.1 Structural characterisation of photocatalyst nanocoatings

The prepared coatings consist of ZTOA nanoparticles, which size (2R) depends on the elemental composition. In particular, it increases from 3.2 nm to 3.6 nm when x increases from 0 to 0.2, than passing through a plateau of ~4.2 nm ($0.3 \leq x \leq 0.7$) it again decreases to 3.6 nm for x=1. After the heat treatment, these ZTOA nanoparticles undergo structural reorganization (i) becoming first amorphous ZTOA → *a*-$Zr_xTi_{1-x}O_2$ at T_1=210-250 °C following by crystallization *a*-$Zr_xTi_{1-x}O_2$ → *crystalline*-$Zr_xTi_{1-x}O_2$ at T_2=380-680 °C [34], where both temperatures T_1 and T_2 were strongly sensitive to the elemental composition x. We have observed that in the range of the elemental composition $x \leq 1$, $Zr_xTi_{1-x}O_2$ conserves anatase crystalline phase. The XRD patterns of three solids with x=0, 0.1 and 0.2 shown in Figure V-5 evidence a shift of Bragg diffraction peaks indicating an increase of distances between the crystalline planes. The smooth modification of the crystalline cell parameters accompanies Ti substitution by Zr in the oxide matrix. The Rietveld refinement using MAUD software with CIF file 5000223 from the PDF4 database [209] indicated a continuous increase of the anatase lattice volume from 138 $Å^3$ to 144 $Å^3$ with the increase of x.

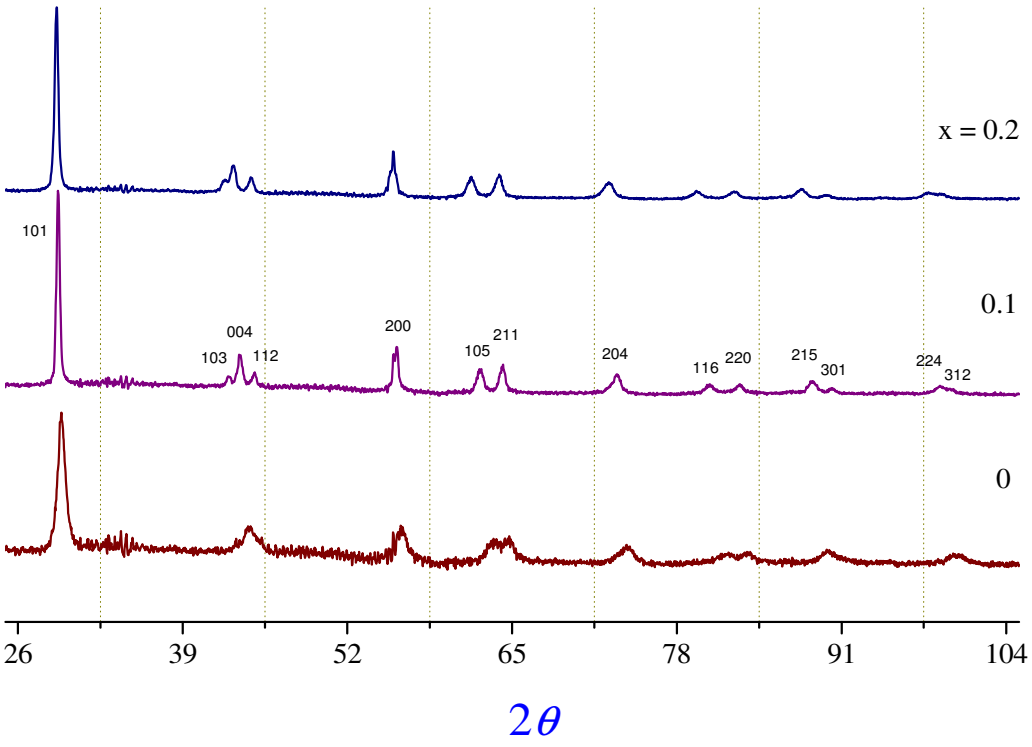

Figure V-5: XRD patterns of nanoparticulate $Zr_xTi_{1-x}O_2$ solids with Zr content x≤0.2 heat treated during 4 hours at temperatures correspondent to the crystallisation onset (Table IV-1).

An excellent Zr dispersion in the titania anatase matrix demonstrate XRD patterns of $Zr_{0.05}Ti_{0.95}O_2$ nanopowders heat treated below 1200 °C in Figure V-6. In bulk TiO_2 at atmospheric pressure anatase to rutile transformation takes place at temperatures ~600 °C [53]. An addition of Zr to the anatase matrix shifts phase transitions to high temperatures. For example in $Zr_{0.2}Ti_{0.8}O_2$, we observed at 600 °C crystallization of anatase TiO_2 with no signs of rutile. According to Figure V- 6, anatase phase conserves in $Zr_{0.05}Ti_{0.95}O_2$ up to 900 °C while rutile phase appears at 1000 °C with the complete transformation achieved at 1100 °C. This result is in agreement with observation of anatase phase at 800 °C at 10% Zr insertion into titania [51].

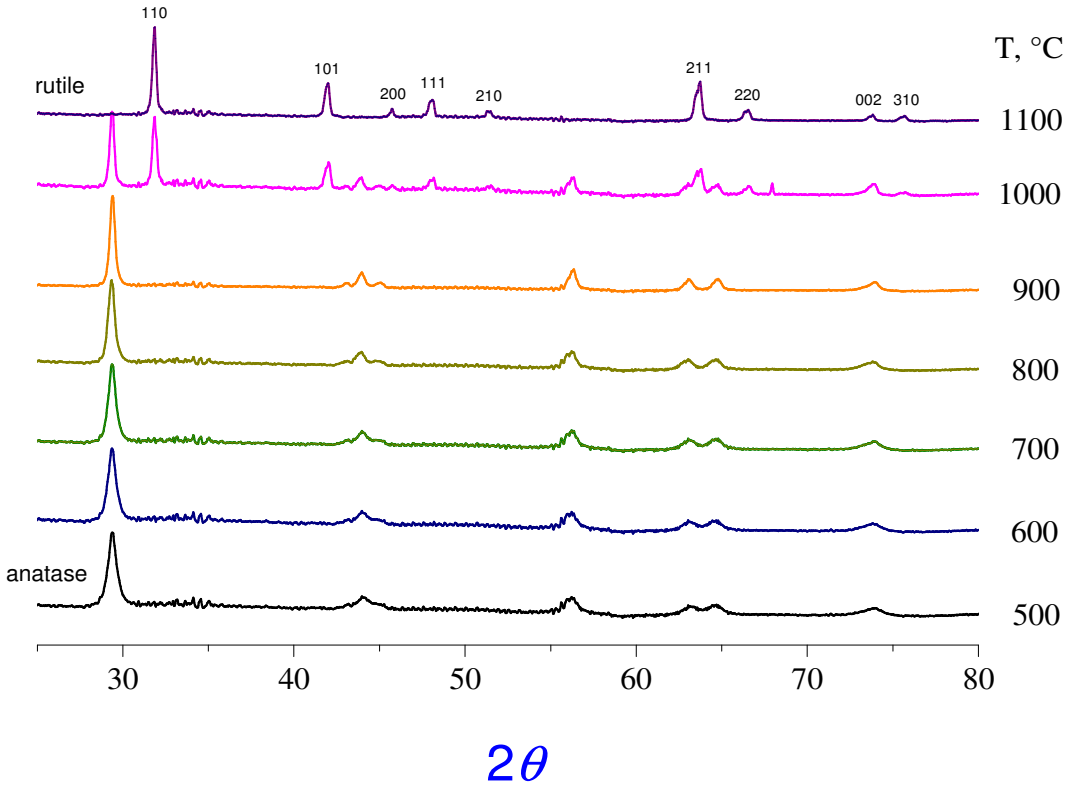

Figure V-6: XRD patterns of nanoparticulate $Zr_{0.05}Ti_{0.95}O_2$ solids heat treated during 4 hours at temperatures between 500 and 1100 °C.

The structural changes affect the interband transition energy. In general, one could expect the band gap variation in this binary oxide from well known 3.2 eV of anatase TiO_2 to 5.1 eV of ZrO_2 [210]. Our spectral measurements presented in Figure IV-11 show a smooth variation of the band gap energy: from 3.16 to 3.35 eV when x increases from 0 to 0.4 and much stronger at higher Zr contents $x \geq 0.6$. The blue shift of the band bap energy is accompanied by a decrease of absorbance of UVA photons. This tendency is in a general agreement with previous publications [48, 177, 184]. Because of a weak light absorption, the compositions with $x>0.5$ were considered by us as not appropriate for photocatalysis with UV-A light activation ($\lambda \approx 360$ nm).

The BET measurements presented in Figure IV-12 indicated a significant increase of the specific surface area of $Zr_xTi_{1-x}O_2$ solids in the range of small Zr addition $0<x<0.4$ with a maximum at $x=0.05$. On the other hand, the compositions with stronger Zr content show rather low specific surface area ~2 m^2/g. Previous studies have shown that an addition of Zr increases the specific surface area of TiO_2. That of $Zr_xTi_{1-x}O_2$ solids often peaked at $x=0.5$

[18-20, 38, 40, 176], which however referred to amorphous or non-crystalline materials, since heat treatment temperatures applied were lower than that of crystallization: $T_c(x=0.5)$=650 °C [206] : 550 °C [19, 20], 400°C [18], 500 °C [38] and 402 °C [176] . Other compositions heat treated with $T>T_c(x)$ have shown the highest surface areas at x=0.5 [40] and x=0.25 [51]. The difference in the reported specific area data can be explained by the material preparation method. Indeed, as it has been recently shown a strong retention of carbon on the surface of smallest 3.6 nm ZOA nanoparticles (x=1 in our notations) induces their sintering at heat treatment, thus reducing the surface area [160]. Apparently, this effect concerns mixed-oxide $Zr_xTi_{1-x}O_2$ nanopowders with a high Zr content, while small Zr addition to anatase titania increases its specific surface area.

The high specific surface area could be explained by the material porosity. A TEM image of $Zr_{0.05}Ti_{0.95}O_2$ particles in Figure V-7a evidences nanoporous morphology of the prepared solids. The mean pores size is close to the particle size indicating a weak powder compaction in our heat treatment conditions. Moreover, the nucleation frequency of a new phase is low and the crystallization appeared at one site propagates over the entire nanoparticulate aggregate, which can be confirmed by a macroscopic alignment of crystalline planes in Figure V-7b.

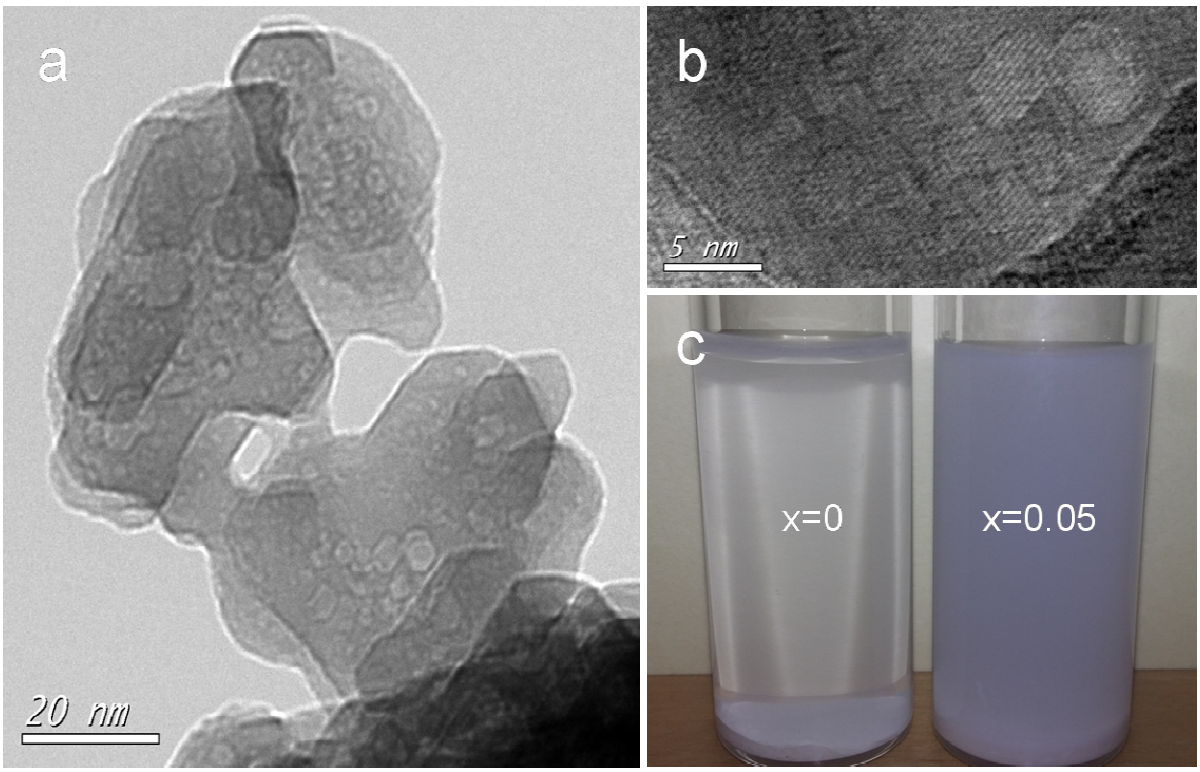

Figure V-7: TEM (a) and HR-TEM (b) images of nanoparticulate $Zr_{0.05}Ti_{0.95}O_2$ solids and photographic images of $Zr_xTi_{1-x}O_2$ nanopowder with x=0 and 0.05 (c).

The higher porosity of $Zr_{0.05}Ti_{0.95}O_2$ compared to TiO_2 particles demonstrates their stability in aqueous solutions. In this experiment, a mass of 200 mg of each nanopowder was introduced in 5 mL of ethanol and treated by ultrasound for 30 min forming two suspensions, the photographic images of which are shown in Figure V-7c after 1 hour resting. The suspension x=0.05 remains stable while that x=0 sediment rapidly after a couple of minutes, indicating its lower mass density.

The $Zr_xTi_{1-x}O_2$ nanocoatings with $x \in [0, 0.2]$ selected for the evaluation of the photocatalysis activity were additionally analyzed by ICP-OES to check possible deviations of their elemental compositions. The compositions of chemical synthesis and of the prepared photocatalyst as well as the mean thickness of coatings are listed in table V-1. We found a good agreement between the engaged and obtained values, although a small decrease by ~10% of the Zr concentration can be noticed. An accuracy of this method was confirmed by an almost complete (92%) recovery of zirconium and titanium. The thickness of the prepared coatings was ~8.5 nm (±10%), which was close to the double layer of deposited ZTOA nanoparticles. Since quasi-monolayer coatings prepared of size-selected nanoparticles were suggested to be the best solution for realization of an efficient catalyst with the highest active area [160], we concluded about successful coating method conserving the material compositions on glass supports. In the following, we will use the corrected photocatalyst compositions from table V-1.

Table V-1: Composition (prepared and after ICP measurements) and thickness of nanocoatings

x (prepared), %	Ti+Zr (measured, ICP), µmol	x (ICP), %	Coating thickness, nm
glass beads	0.2	-	0.15
0.0	13.2	0.04	9.3
2.5	10.9	2.14	7.8
5.0	11.9	4.25	8.5
10.0	11.3	9.51	8.1

20.0	12.1	16.9	8.8

V.3.2 Photocatalytic activity in gas phase

The characteristic reactor performance using $Zr_xTi_{1-x}O_2$ photocatalyst with x=0.0425 is presented in Figure V-8. Two illumination cycles are shown. The ethylene decomposition begun after UVA lamps switched on and stopped after the lamps switched off. The stationary reactor performance with the decomposition yield η=66.5% was attained after a short transient time after the beginning of each illumination. This transient time was equal to the UVA lamps warm up time ~3 min, which was observed in the second and subsequent illumination cycles. However, the first transient time was significantly longer ~10 min, which may indicate a modification of the photocatalyst interface. Indeed, we have previously observed such effect in iron doped titania [128] and assigned to accumulation of non-volatile reaction by-products of ethylene decomposition on the photocatalyst surface. The fact that the transient time in present experiments was significantly shorter can be explained by a negligible humidity, which was 35% in the previous studies. No photocatalyst deactivation was observed over several hours of the reactor performance.

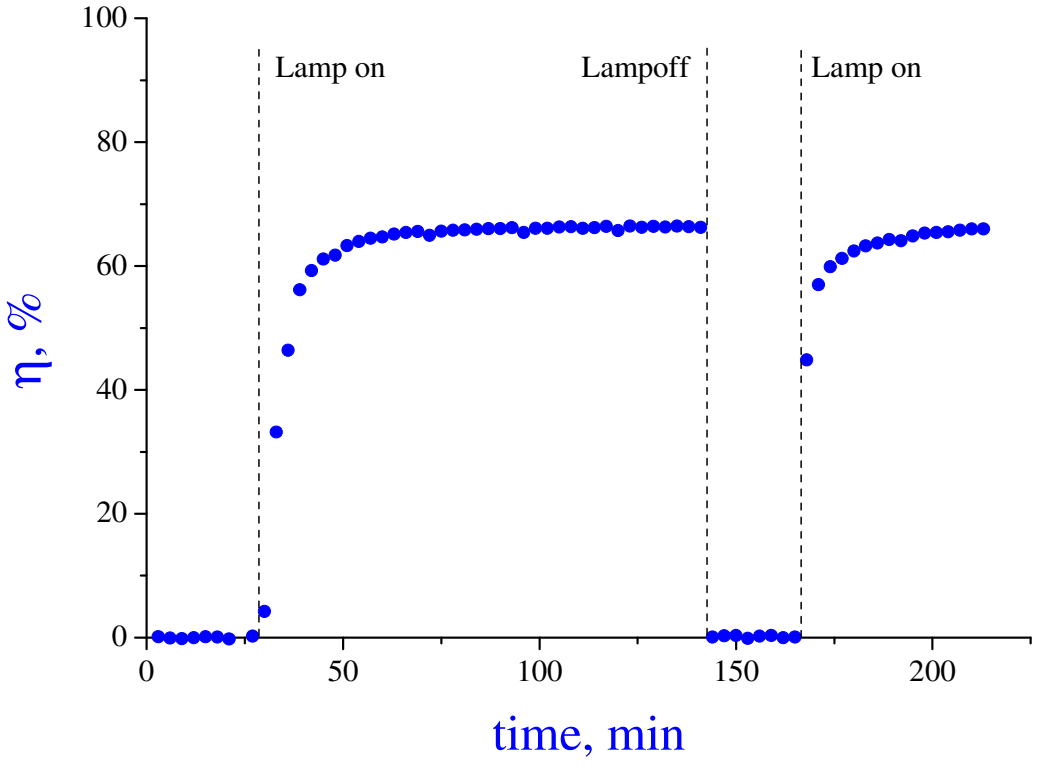

Figure V-8: Ethylene decomposition yield η as function of time using $Zr_xTi_{1-x}O_2$ photocatalyst (x=0.0425) (C_{in}=120 ppm).

V.3.2.1 Influence of pollutant concentration

The photocatalytic activity of $Zr_xTi_{1-x}O_2$ (x=0.0425) photocatalyst in the reactor versus input ethylene concentration in the range between 60 and 300 ppm is shown in Figure V-9. These experimental data allow estimating the reaction order of the photocatalytic process. For this estimation, Emeline et al [211] have proposed an empirical expression $(dC/dt)=kC^n$ with the reaction order n varying between 0 and 1. Applying this expression to a continuous-flow reactor of length L, one can obtain

$$\ln\left(\frac{C_{\text{in}}}{C_{\text{out}}}\right)=\frac{\ln\left(1-(1-n)kL/C_{\text{in}}^{1-n}\right)^{-1}}{1-n} \qquad \textit{Equation V-6}$$

The least-squares fit of the experimental data with expression (6) is shown by solid line in Figure V-9 providing the reaction order n=0.6 in the range of ethylene concentrations 60-300 ppm.

Alternatively, the Langmuir–Hinshelwood model can be used to explain the photooxidation kinetics [211]. The following processes can be considered:

$$S+hv\rightarrow S*$$

$$S*\xrightarrow{\tau^{-1}}S$$

$$C\xleftrightarrow{k_d/k_a}C_{\text{ads}}$$

$$C_{\text{ads}}+S*\xrightarrow{k_r}p$$

where S, S^*, C, C_{ads} and p are the ground-state and activated surface sites, pollutant and adsorbed pollutant concentrations, and product concentrations. τ, k_a, k_d and k_r are excited state lifetime, adsorption, desorption and reaction constants. Applying to the continuous-flow reactor, the following expression can be obtained [128]:

$$\frac{a}{b}\ln\left(\frac{C_{in}}{C_{out}}\right)+\frac{1}{b}(C_{in}-C_{out})=L \qquad \textit{Equation V-7}$$

where constants *a* and *b* depends on adsorption/desorption and reaction constants, number density and lifetime of the available photocatalytically active sites and illumination UVA light power. The reaction order 1 or 0 corresponds to the dominance of the first or second term in the left part of equation V-7. A careful analysis of the photocatalytic process using equation V-7 showed that the reaction order can vary along the pollutant flow in the reactor tube and the overall process kinetics progressively changes from pure first order for $C_{in} \leq 100$ ppm to zero order, first at the reactor input propagating towards the reactor output with an increase of the ethylene concentrations above 100 ppm [212].

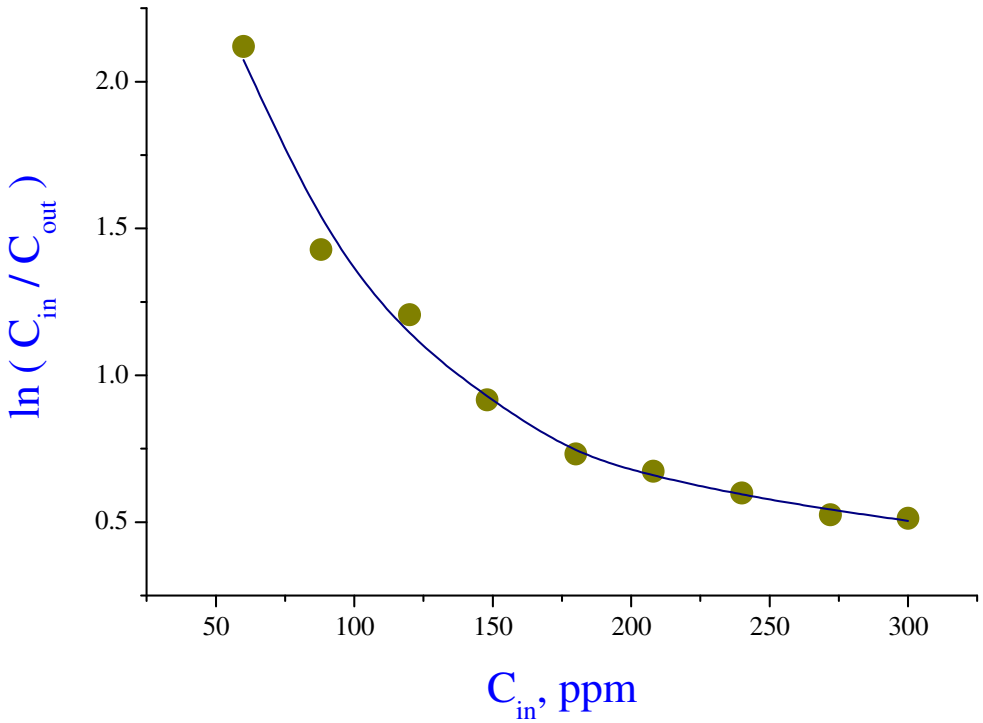

Figure V-9: Photocatalytic activity of $Zr_xTi_{1-x}O_2$ (x=0.0425) for ethylene decomposition versus input concentration. The fit with equation V-6 is shown by solid line.

V.3.2.2 Influence of lamp intensity

The photocatalytic performance of $Zr_xTi_{1-x}O_2$ photocatalyst with x=0.0425 was further investigated with different UV-A lamps power. The comparison was done by irradiating with 3, 4 and 6 lamps in respectively trigonal, tretragonal and hexagonal geometries placed around the reactor tube filled with coated beads (m=1.29 g) on 5 cm length. The light power (P, mW) was measured by a photometer (THORLABS) through an

orifice diaphragm placed at the distance 10 cm from the photocatalysis reactor, which guarantees a satisfactory light field averaging. Figure V-10 shows the result of these measurements in a frame of $\ln(C_{in}/C_{out})$ and P. The observed linear dependence supports the conclusion about first order reaction kinetics at the input ethylene concentration C_{in}=120 ppm. Indeed, according to equation V-5 the relationship between the pollutant decomposition and light power (included in k_r) would be $\ln(C_{in}/C_{out}) \propto P$ and $(C_{in} - C_{out}) \propto P$ in case of first and zero order reaction kinetics. Obviously, the second expression does not agree with the experimental data. Moreover, this linear dependence indicates a negligible e^-/h^+ effect of the photoinduced charges concentration on recombination rate in the photocatalyst, which can be explained by an effective photoinduced charges separation, transfer and trapping at the catalyst surface.

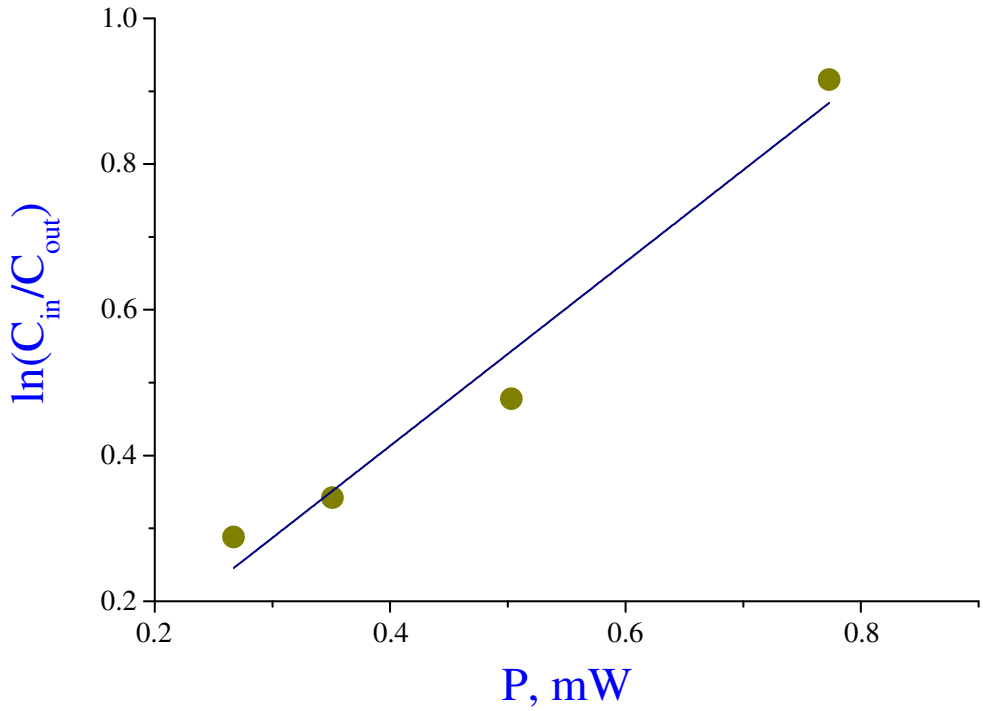

Figure V-10: Photocatalytic activity of $Zr_xTi_{1-x}O_2$ (x=0.0425) for ethylene decomposition versus lamp power (C_{in}=120 ppm).

V.3.2.3 Influence of elemental composition

The first order reaction kinetics permits to compare activities of $Zr_xTi_{1-x}O_2$ photocatalysts with different Zr content, by using equation V-5. To show an importance of

the heat treatment, we evaluated the activities of photocatalysts calcinated at different temperatures in the range between 400 and 650 °C. The measurements of $\ln(C_{in}/C_{out})$ realised at the ethylene concentration C_{in}=120 ppm are shown in Figure V-11.

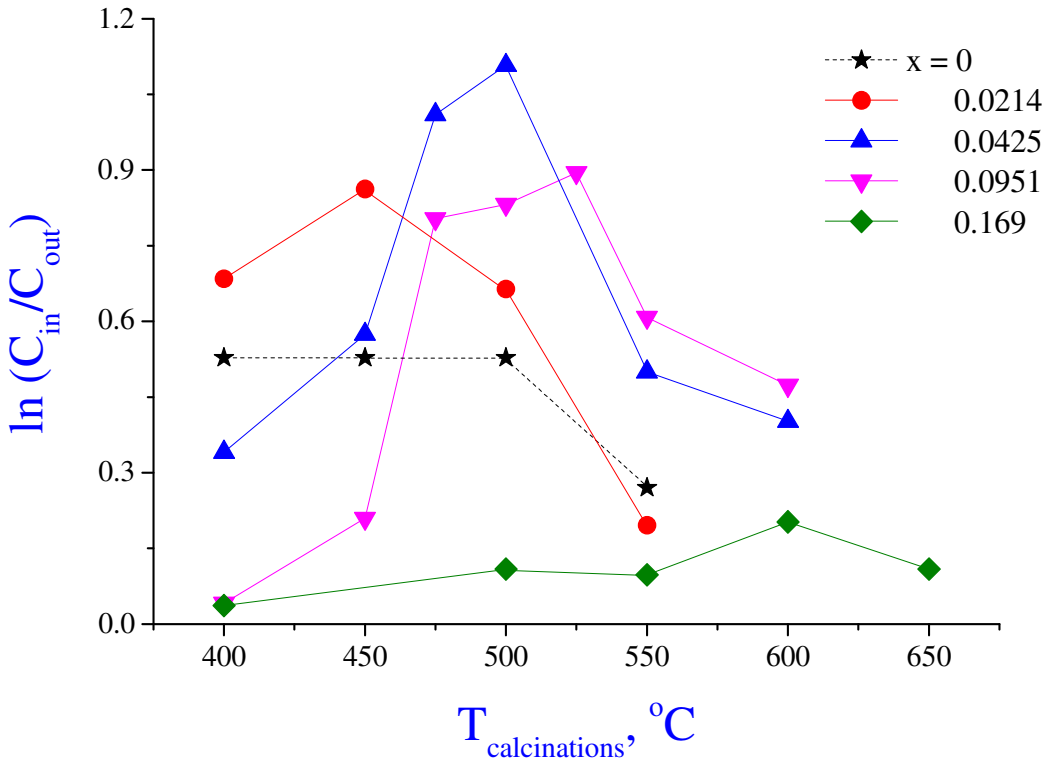

Figure V-11: Photocatalytic activity of $Zr_xTi_{1-x}O_2$ ($0 \leq x \leq 0.2$) for ethylene decomposition (C_{in}=120 ppm). The photocatalysts were calcinated at temperatures between 400 and 650 °C according to table IV -1.

According to the obtained results, the best photocatalysts were prepared after calcinations temperatures indicated in table V-1, which correspond to the crystallisation onset. A weak activity of the amorphous material prepared after calcination below the crystallisation onset is expected according to Ohtani et al [213], who has explained it by a structural disorder inherent to amorphous TiO_2 facilitating recombination of photoinduced electron-hole pairs. A decrease of the photocatalyst activity with an increase of the heat-treatment temperature above that of the crystallisation onset may be related to the grains coarsening, which prohibits an access of the photoinduced charges to the photocatalyst surface. A direct correlation between $Zr_xTi_{1-x}O_2$ nanoparticulate photocatalysts and its specific surface area is shown in Figure V-12. The best activity is attained by the material

with x=0.0425 also exhibiting the largest specific surface area of 69.3 m^2/g. This result is in a general agreement with the lowest x values reported in literature and disagree with others from table I-4. However, since our study is the first one directly addressing the composition homogeneity of this photocatalyst, we definitely conclude on this point providing a receipt to the photocatalyst synthesis.

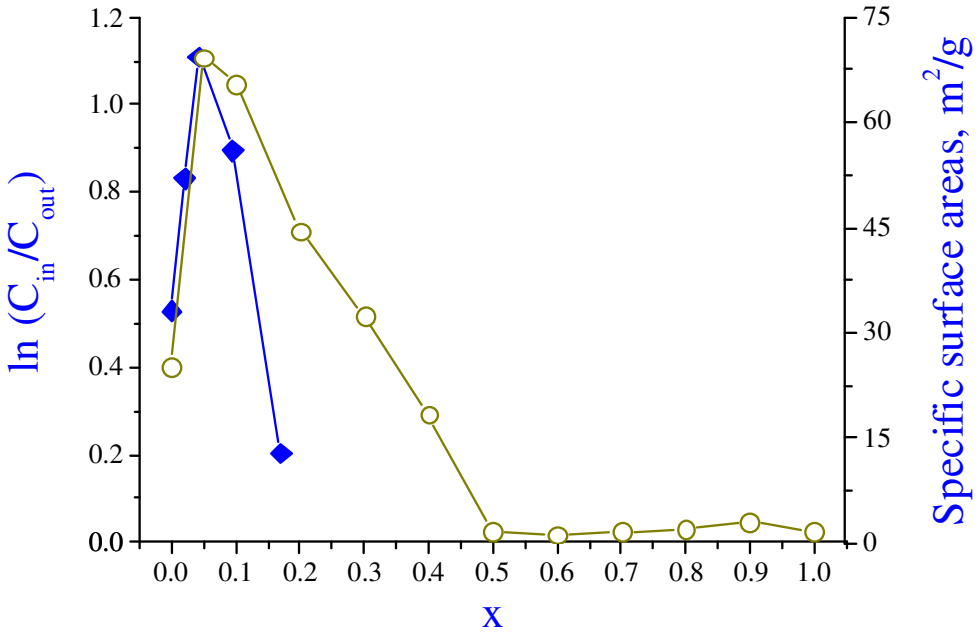

Figure V-12: Photocatalytic activity (♦) and specific surface area (○) of $Zr_xTi_{1-x}O_2$ nanoparticulate photocatalysts (ethylene pollutant, C_{in}=120 ppm).

A tentative model can be discussed at this point relating photocatalytic activity of the prepared coatings to their specific surface area. All materials with compositions 0≤x<0.2 correspond to anatase phase that permits a comparison. The photocatalytic activity defined as $\ln(C_{in}/C_{out})$ is proportional to the photocatalyst mass delivering photoinduced charges to the surface sites $m_{act} = S\rho\delta$, where S is the catalyst surface, ρ is the mass density and δ is the shortest charge (e^- or h^+) localization distance. The photocatalytic activity can be expressed as the ratio between the active m_{act} and total m masses of a photocatalyst. Since the coating thickness is small, all material volume is exposed to UVA illumination and one can write:

$$m_{act}/m = \rho_{b,x} S\delta/m = \rho_{b,x}\sigma\delta \qquad \textit{Equation V-8}$$

where σ is the specific surface area. The $Zr_xTi_{1-x}O_2$ ($0 \le x \le 0.2$) anatase mass density varies as $\rho_{b,x} = \rho_{b,0}(1+0.9x)/(1+0.2x)$, where $\rho_{b,0}$=3.9 g/cm^3 is the mass density of anatase TiO_2 (x=0), (1+0.2x) describes relative changes of the lattice volume [206] and replacement of Ti by Zr increases the relative cell weight by a factor $m_{Zr}/m_{Ti} \cdot x + (1-x) = 1+0.9x$. We can rewrite equationV-8 as

$$\ln(C_{in}/C_{out})/\sigma\rho_{b,x} \propto \delta \qquad \textit{Equation V-9}$$

This normalized photocatalytic activity expressed by the left part of equation V-9 as a function of elemental composition x is shown in Figure V-13, which is expected to be constant when the material structure is not changed significantly. Apparently, this state is maintained at a small Zr content $x \le 0.05$, which corresponds to the calcinations temperatures below 500 °C. With an increase of the heat treatment temperature the photocatalyst grains coarsen. The photocatalyst activity drops when the grains size becomes larger than the charge localization length δ. At this point an excluded material volume appears, from which photoinduced charges cannot attain the photocatalyst surface and trig reactions.

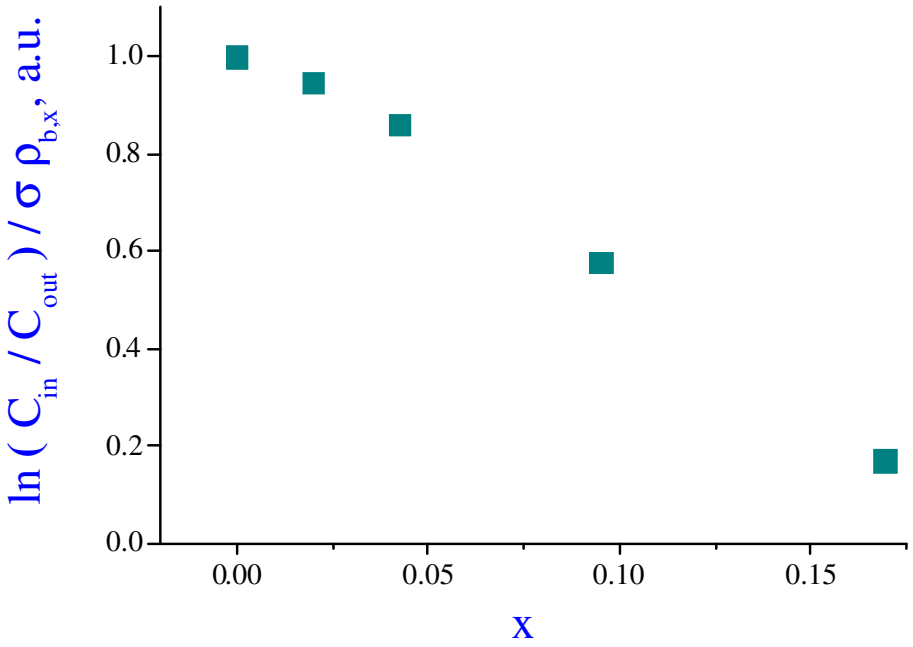

Figure V-13: Normalised photocatalytic activity of $Zr_xTi_{1-x}O_2$ nanoparticulate photocatalysts according to equation V-9.

V.4 Photocatalysis in aqueous phase

It is widely recognized that the photocatalyst activities in the gas and liquid phases differ, which is explained by the underlying reaction and mass transport mechanisms. Consequently, we decided to check the activity of the prepared mixed metal oxide photocatalyst in aqueous solutions.

V.4.1 Experimental conditions

For these measurements we used the composite $Zr_xTi_{1-x}O_2$ in form of powders at x = 0.05 and 0.10 to be performed the photocatalytic experiments of degradation methylene blue (MB) and phenol (PH) to be compared with pure TiO_2 activities. The selected compositions and calcinations were referred to the most active in gaseous phase. The photocatalytic nanopowders were synthesized via the procedure described in chapters III and IV. MB with concentrations between 4 and 7 ppm in the volume of 400 mL were mixed with composite $Zr_xTi_{1-x}O_2$ nanopowders of mass m ≈ 400 mg and compositions x=0.00 and 0.10 in aqueous solution. UVA illumination at a wavelength λ = 365 nm was used to trig photocatalytic degradation of MB during 80 min and then irradiation was continued with a UV-C lamp at λ=254 nm for 140 min of total time. The sampling was made periodically during the irradiation cycle for an analysis of the remaining pollutant in the solutions using SECOMAN UViline 9400 spectrophotometer.

In a supplementary series, activities of pure TiO_2 and composite $Zr_{0.05}Ti_{0.95}O_2$ catalysts were compared. The schema of this experiment is depicted in Figure V-14. MB pollutant of a volume 80 mL and concentration 7 ppm in beaker was diluted from stock solution of concentration 70 ppm. $Zr_xTi_{1-x}O_2$ nanopowder with concentration 0.6 g/L was added to the solutions under magnetic stirring. Air-flow pump (Airwia 3) brought continuously gaseous oxygen into solutions. The solution was illuminated with three 8-W UVA lamps at 365 nm. The solution sampling was made periodically during the irradiation cycle: an analysis of the remaining pollutant was performed after centrifugation at 80000/min for 7 min using UV/Vis spectrometer Shimadzu UV-2700 at 663 nm that corresponds to the maximum MB absorption.

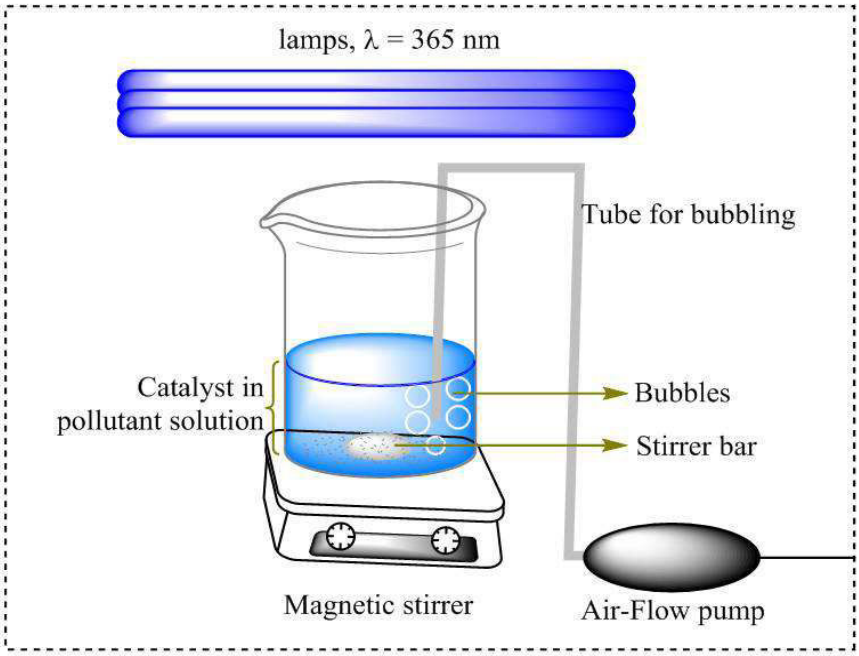

Figure V-14 : Schema of photocatalytic test in aqueous phase.

The photocatalytic decomposition of PH was carried in the same installation as of MB with the pollutant concentrations of 25 ppm and 2 g/L of catalysts loading. Concentrations of the remaining PH in the solution were measured by the samples absorbance at 270 nm that corresponds to the maximum of PH absorption.

V.4.2 Comparison of photocatalysts

Methylene blue (MB) pollutant. The conclusion drawn about $Zr_xTi_{1-x}O_2$ catalyst activities in gas phase were confirmed by experiments in aqueous solutions. The composite with compositions $0<x\leq0.1$ has shown a higher activity than pure TiO_2: for example, at x=0.1 the decomposing of MB was up to 45 % and 53 % for calcinations at 400 and 500 °C respectively after 80 min UVA illumination. The stronger degradation at 500 °C treatment can be explained by a better crystallinity of the material. For the same illumination time, pure TiO_2 heat treated at 500 °C decomposed 26 % of MB. The photographs of the MB aqueous solutions after illumination with UVA/UVC lamps are shown in Figure V-15.

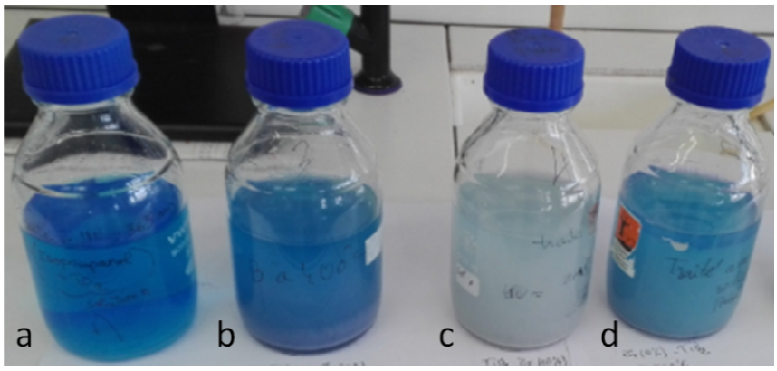

Figure V-15: MB solutions after illumination with UVA (80') and UVC (60') lamps: no-photocatalyst (a), $Zr_{0.1}Ti_{0.9}O_2$ heat treated at 400 °C (b) and 500 °C (c) and pure TiO_2 heat treated at 500 °C (d).

One can notice a negligible decomposition of MB with no photocatalyst (a), a week one induced by an amorphous composite $Zr_{0.1}Ti_{0.9}O_2$ (b) and pure crystalline TiO_2 (d) materials, while crystalline $Zr_{0.1}Ti_{0.9}O_2$ nanopowder strongly decomposes MB (c). We notice that the photocatalytic MB degradation under UVC lamp illumination was stronger compared to UVA as shown in Figure V-16 for the composition with x=0.1.

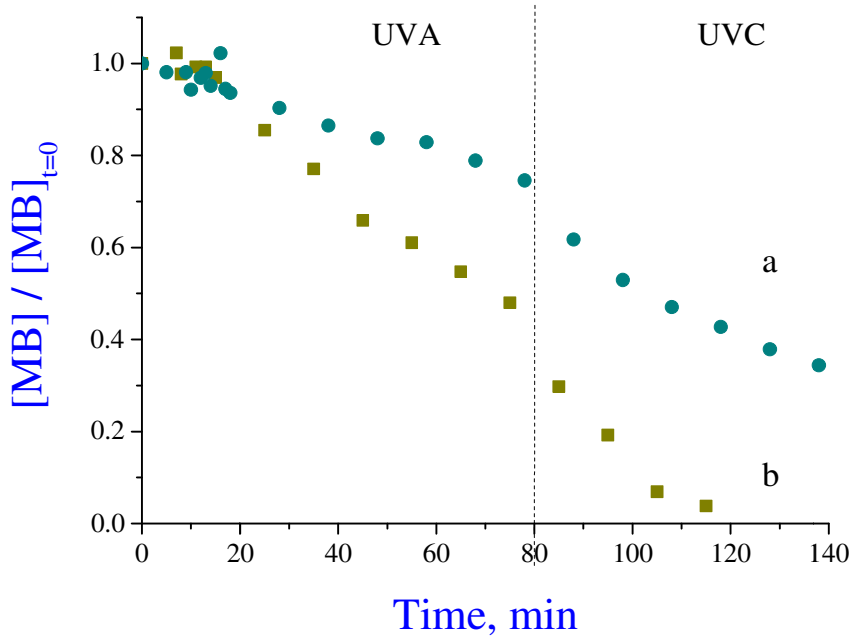

Figure V-16: Photocatalytic decomposition of MB in aqueous solution after illumination with UVA (0−80') and UVC (80−120') light, using TiO_2 (a) $Zr_{0.1}Ti_{0.9}O_2$ nanopowders heat treated at 500 °C (b).

In overall, during 140 min 74.8 and 96.2 % of MB was degraded in presence of $Zr_{0.1}Ti_{0.9}O_2$ nanopowder respectively calcinated at 400 and 500 °C, while pure TiO_2 decomposed only 65.6 % MB. The results of these photocalytic tests are summarized in Table V-2.

Table V-2: Conditions and conversion results of composite $Zr_xTi_{1-x}O_2$

Powders	**$Zr_{0.1}Ti_{0.9}O_2$**	**$Zr_{0.1}Ti_{0.9}O_2$**	**TiO_2**
Treatment temperatures (°C)	400	500	500
Amount of using catalysts (mg)	400	398	320
Initial pollutant concentrations	6.27	4.19	4.64
Final concentrations (ppm)	1.58	0.16	1.60
Conversion (%)	74.8	96.2	65.6

Further comparison was made between $Zr_{0.05}Ti_{0.95}O_2$ and TiO_2 nanopowders on photocatalytic decomposition of MB. The composite photocatalyst exhibited much higher activity compare to pure TiO_2 as shown in Figure V-17.

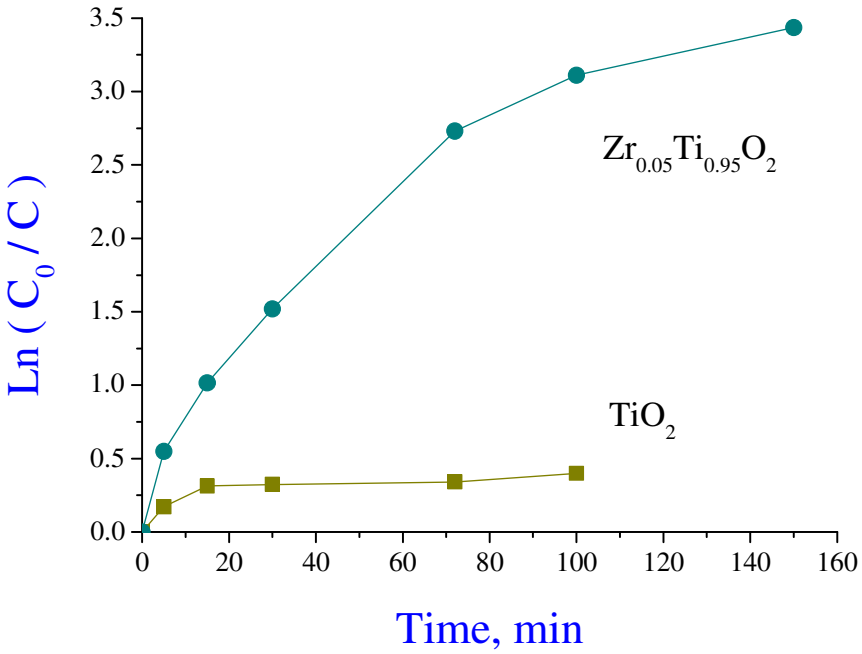

Figure V-17: Photocatalytic decomposition of MB in aqueous solutions using $Zr_{0.05}Ti_{0.95}O_2$ and TiO_2 nanopowders.

The kinetics constant defined by the initial slope of the curves was increased in $Zr_{0.05}Ti_{0.95}O_2$ more than 2.5 times. Although the decomposition process showed complex reaction order with efficiency decreasing with time, almost 97% of MB was decomposed by the composite photocatalyst after 160 min of UVA illumination, while pure TiO_2 showed much lower decomposition ~40% with a clear tendency to saturation. Figure V-18 demonstrates changes of color of the MB solutions in the photocatalytic process by using $Zr_{0.05}Ti_{0.95}O_2$ catalyst.

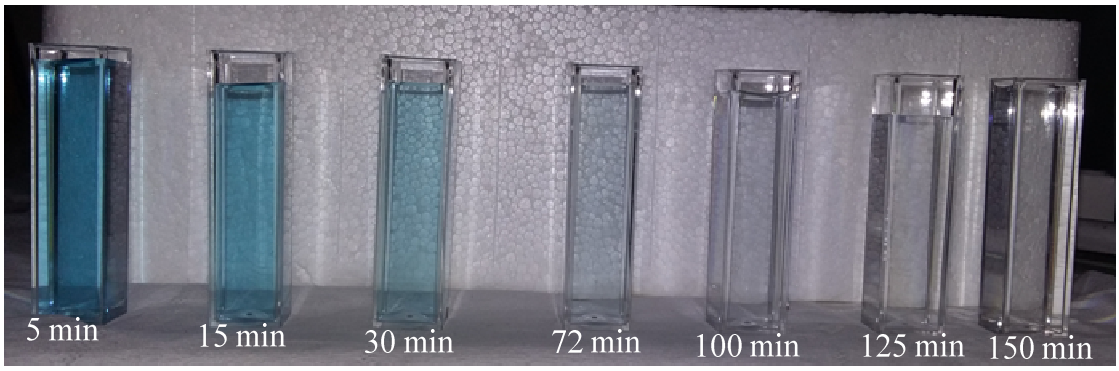

Figure V-18: The changing methylene blue color by time during photodegradation.

We notice that the blanc text made in the same experimental conditions without any photocatalyst evidenced negligible MB photolysis after 3 hours of UVA illumination.

Phenol (PH) pollutant. Decomposing PH is harder to achieve than MB. The decomposition kinetics is complex. However, results of our tests shown in Figure V-19 clearly evidenced a higher activity of $Zr_{0.05}Ti_{0.95}O_2$ compared with TiO_2.

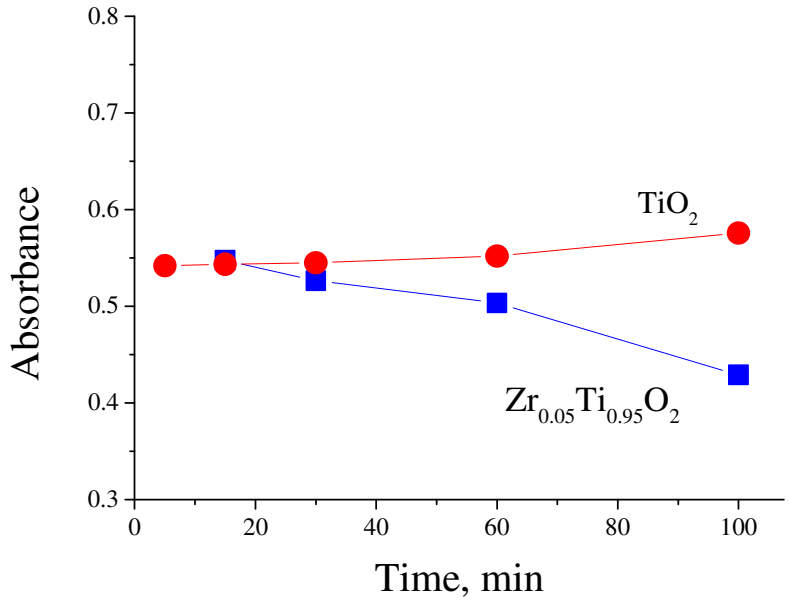

Figure V-19: Photocatalytic decomposition of PH in aqueous solutions using $Zr_{0.05}Ti_{0.95}O_2$ and TiO_2 nanopowders.

V.5 Conclusion

The mixed composite $Zr_xTi_{1-x}O_2$ was succeeded synthesis using micromixing reactor to mix for producing monodesperse particles with high homogenous and this composite was used to do photocatalyst to decompose ethylene pollutant as an application. The materials were well coated as colloid films on borosilicate beads with the sickness around 8 nm. Confirming from the ICP-OES, the compositions with good enough quantity were almost the same between preparations and real on borosilicate glass beads. The enhance activity of this composite depended on compositions and treatment temperatures. At optimum composition of x = 0.0425 and treatment temperature at 500 °C, the activity could be improved up to two times compared to pure TiO_2. The materials were very strong absorbed UV photocatalysis light that could decompose the pollutant in linear relationship of powers verse decomposing concentrations of ethylene.

The optimum composition and calcinations as powder preparations had high BET sure face area with porosity materials by TEM with low density. The modelling was developed to be discussed. At x = 0.05 preparations, the anatase phase could be kept up to higher than 900 °C and some changes at 1000 °C with completely changed to rutile at 1100 °C.

This composite of the small amount ZrO_2 content is not just only active in the gaseous phase, but it was also active in the aqueous phase to decompose methylene blue and phenol as representative pollutants. At x = 0.1 with calcinations at 500 °C as powder preparations, it has better activity about 50 % than pure titanium dioxide for the same treatment temperature for decomposing methylene blue in both UV-A and UV-C irradiation lights. For $Zr_{0.05}Ti_{0.95}O_2$ powder at 500 °C treatment temperature, its activity is even much better activity than pure TiO_2 at least two times for decomposing both methylene blue and phenol.

Notation

ICP-OES	inductively coupled plasma-optical emission spectroscopy
VOC	volatile organic compounds
GC-FID	Gas Chromatography-Flame Ionization Detector
UV	ultraviolet
C_{in}	gaseous pollutant concentration in before degradation in photocatalytic reactor
C_{out}	gaseous pollutant concentration after degradation in photocatalytic reactor
TEM	transmission electron microscopy
BET	Brunauer–Emmett–Teller
SD	standard deviation
T	temperature (°C)
ppm	part per million
S	ground state
S^*	activated surface site
S_0	available active sites
L	length of photocatalysis reactor
τ	activated stated lifetime
k_a	adsorption constant
k_d	desorption constant
k_r	reaction constant
k	rate constant
C	concentration of pollutant
C_{ads}	adsorption concentration
p	product
n	order reaction
C_0	initial pollutant concentration in liquid form
C	remaining pollutant concentration in liquid form
Symbols	
λ	wavelength (nm)
η	ratio of the decomposing pollutant

General conclusions and perspectives

General conclusions

The design of a robust fabrication process of size selected nanoparticles and bulk nanostructured materials on this base is of high demand in the field of nanotechnology and nanomaterials. In our studies, we considered sol-gel process and find out conditions for nucleation of macroscopic properties of monodispersed metal oxide nanoparticles. Previous studies of simple metal oxides TiO_2, ZnO, ZrO_2 were extended in the present study to a more complex system of composite metal oxides. This PhD work was devoted to the nucleation-growth process of the composite metal oxide solid containing Ti and Zr elements. We followed the formation of the bulk solid from nanometric nucleus in a chemical reactor with ultarapid micromixing of reacting fluids in a turbulent flow, gaseous atmosphere and temperature control. The reactor provides point-like reaction conditions in the regime of low Damköhler numbers. The size and growth kinetics of nanoparticles were monitored *in situ* by an original fiber optical probe using dynamic and static light scattering DLS/SLS method. The structural and functional properties of the obtained nanomaterials were correlated with the nucleus size and composition.

In order to obtain reliable information on the reference system of TiO_2, we performed a comparative study of the nucleation-growth kinetics of titanium oxo-alkoxy nanoparticles in n-propanol and isopropanol solvents. A common feature of the both systems is the appearance of stable units with the hydrodynamic radius 1.6 nm in the very beginning of the sol-gel process after an ultra-rapid mixing of the reacting fluids containing titanium precursor and water. Their size was stable in a large parametric domain (C_{Ti} and H) of the sol-gel process and is not sensitive to the solvents. At large hydrolysis ratios (H>2) the basic colloid unit becomes nanoparticle; in this domain both size and reaction kinetics are sensitive to the solvents. In particular, the hydrodynamic radius of the TOA nanoparticles in n-propanol and isopropanol solvents is 1.9 nm and 2.6 nm respectively. Our results suggest that the stability of the growing TOA species decreases with an increase of their size, supporting the hierarchical model of the sol-gel growth. Our analysis confirms the critical hydrolysis ratio h^*=1.5, which enables the growth of TOA species forming quasi-linear chains of the associating clusters and nanoparticles. The obtained results are of importance since they permit to revise the general picture of the nucleation and assign the smallest units of 1.6-nm radius to nucleus, which serves to be a bulding block of bulk solids.

We applied the micromixing technique to nucleate monodispersed mixed metal oxides nanoparticles of different elemental compositions $0 \le x = C_{Zr} / (C_{Zr} + C_{Ti}) \le 1$ and, on this base

to prepare $Zr_xTi_{1-x}O_2$ crystalline solid, which conserve the highly homogeneous elemental dispersion of the precursor nanoparticles. The zirconium-titanium oxo-alkoxy (ZTOA) nanoparticles were prepared via sol-gel process using zirconium (IV) propoxide and titanium (IV) isopropoxide precursors. ZTOA nanoparticles with the radius 2.1 nm appear at the hydrolysis ratio H=1.25 and $0.3 \leq x \leq 0.6$, which is different from that of pure titanium-oxo-alkoxy (TOA, x=0) and zirconium-oxo-alkoxy (ZOA, x=1) with respective radii 1.6 and 1.8 nm. The mixed oxide nanoparticles were stable at $H \leq 1.5$ and underwent an accelerated growth at higher H values during a common induction period of the sol-gel process. The structural transformation of ZTOA nanoparticles takes place at a temperature in the range 210-250 °C, which sensitively depends on the elemental composition. This transformation is accompanied by the departure of organics from the surface of a nanoparticle and leads to its amorphisation. The crystallization takes place at higher temperatures, which attain maximum of 680 °C at x=0.5 and decrease with either following increase or decrease of x. The obtained solids were assigned to three different pure phase materials: for $0 \leq x \leq 0.2$, anatase TiO_2 is preserved, for $0.3 \leq x \leq 0.6$, orthorhombic $Zr_xTi_{1-x}O_2$ appears and for $0.7 \leq x \leq 1$, mixed monoclinic and tetragonal phases of ZrO_2 coexist. The crystalline cell size of all three phases underwent a continuous variation with x and the cell volumes increased with x in agreement with the larger size of the substitution ion Zr^{4+} compared to host Ti^{4+}. The TEM images evidenced the nanoporous structure of the submicronic mixed oxide monocrystals with the mean pore size about that of ZTOA nanoparticle. Based on these results, we conclude that the elemental composition x induces a profound modification of the material electronic structure, which defines the size of ZTOA nuclei, strength of the surface bonds and crystalline structure of the final material $Zr_xTi_{1-x}O_2$.

Based on the size-selected ZTOA nanoparticles with the controlled elemental composition at nanoscale, $Zr_xTi_{1-x}O_2$ nanoparticulate photocatalyst coatings were prepared. The nanoparticles were deposited on borosilicate glass beads and heat treated to obtain crystalline nanocoatings with different elemental compositions x. The band gap of $Zr_xTi_{1-x}O_2$ shifts to higher energies with an increase of Zr content, making the material with $x \in [0, 0.2]$ appropriate for UVA photocatalysis: this material conserves anatase phase of titania strongly distorted by an addition of Zr. The photocatalytic activity of the prepared materials was evaluated on ethylene gas decomposition in a continuous-flow fix-bed reactor under UVA illumination, equiped with an automatic

chromatography measurements of the pollutant concentrations at its input C_{in} and output C_{out}. The photocatalytic activity defined as $A = \ln(C_{in} / C_{out})$ permitted the photocatalysts comparison in the regime of first order reaction kinetics, which were rigurously verified. The best activity showed a composition with x=0.0425 heat treated at 500 °C, which was twice higher comared to pure anatase TiO_2. We relate this enhanced activity to the material open porosity and explain its variation with x and T (°C).

The conclusions about $Zr_xTi_{1-x}O_2$ nanoparticulate photocatalysts obtained with in gas phase cannot be directly extrapolated to liquid phase, since underlying mechanisms of the photocatalutic processes differ. Therefore we completed the photocatalytic test in the aqueous phase. The photocatalyst with the optimal elemental composition exhibited also an enhanced activity towards decomposition of MB and phenol pollutants, which was much higher compared to that of pure anatase TiO_2 nanocoatings. Moreover, it also showed much weaker tendency to deactivation by secondary reaction products (phenol test).

Summing up, in this work we proposed an approach to the preparation of functional composite metal oxide materials with reproducible functional properties, which is based on preformed size-selected metal oxo-alkoxy nanoparticles with controlled elemental composition.

Perspectives

1. The applied method of the material preparation can be extended to other composite materials, like Ti-V oxides. Kinetics of the nucleation-growth process has to be studied in the micromixing reactor that will shed light on the sol-gel growth of solids. Despite more complexity of the last system, it may offer band gap engineering in the visible spectral range, which is of high demand in environmental photocatalysis.

2. The nanoparticulate $Zr_xTi_{1-x}O_2$ coatings can be studied in practical environmental photocatalysis in liquid phase with emphasize of the reaction pathways and emerging by-products.

3. It would be interesting to test nanoparticulate $Zr_xTi_{1-x}O_2$ materials in catalysis process, such as converting isopropanol to propence, acetone and isopropylether (see ref [18]).

4. Doping of the nanoparticulate $Zr_xTi_{1-x}O_2$ with metal (Pt, Pd, etc) and inclusion of other metal oxides (V_2O_5, B_2O_3, etc) can be studied to further increase the catalytic activity (see ref [13]).

Publications and conferences

Publications

1. G. D. Fanou, B. Yao, K. Cheng, O. Brinza, M. Traoré, A. Kanaev, K. Chhor, Elaboration of Novel NanoparticulateTiO2-P25@n-TiO2 Composite for Photocatalysis**, International Journal of Advanced Applied Physics Research, 3 (2016) 19-25.**
2. K. Cheng, K. Chhor, A. Kanaev, Solvent effect on nucleation-growth of titanium-oxo-alkoxy nanoparticles, Chemical Physics Letters, 672 (2017) 119-123.
   Chosen for journal cover page.
3. K. Cheng, K. Chhor, A. Kanaev, chosen for Advances in Engineering: Highlight on publication "Solvent effect on nucleation-growth of titanium-oxo-alkoxy nanoparticles", published 30 June 2017.
   https://advanceseng.com/applied-physics/solvent-effect-nucleation-growth-titanium-oxo-alkoxy-nanoparticles/.
4. K. Cheng, K. Chhor, O. Brinza, D. Vrel and A. Kanaev, From nanoparticles to bulk crystalline solid: Nucleation, growth kinetics and crystallisation of mixed oxide $Zr_xTi_{1-x}O_2$ nanoparticles, CrystEngComm, 19 (2017) 3955-3965.
5. K. Cheng, K. Chhor, A. Kanaev, Elaboration and enhanced activity of the mixed oxide $Zr_xTi_{1-x}O_2$ nano-photocatalyst, Chemical Engineering Transactions, vol.60 (2017) 37-42.
6. K. Cheng, K. Chhor, A. Kanaev, "Photocatalytic nanoparticulate $Zr_xTi_{1-x}O_2$ coatings with controlled homogeneity of elemental composition", submitted.

Conferences

1. **K. Cheng,** C. Khay, A. Kanaev; Elaboration of mixed oxide Zr/Ti and V/Ti functional nanoparticles, the 19 th sol-gel conference, 03-08 September 2017, Liège, Belgium.

References bibliography

References

[1] J. Muscat, V. Swamy, N.M. Harrison, First-principles calculations of the phase stability ofTiO_2, Physical Review B, 65 (2002).

[2] A. Fujishima, X. Zhang, D.A. Tryk, TiO_2 photocatalysis and related surface phenomena, Surface Science Reports, 63 (2008) 515-582.

[3] R. Kaplan, B. Erjavec, G. Dražić, J. Grdadolnik, A. Pintar, Simple synthesis of anatase/rutile/brookite TiO_2 nanocomposite with superior mineralization potential for photocatalytic degradation of water pollutants, Applied Catalysis B: Environmental, 181 (2016) 465-474.

[4] J. Zhang, P. Zhou, J. Liu, J. Yu, New understanding of the difference of photocatalytic activity among anatase, rutile and brookite TiO_2, Physical Chemistry Chemical Physics, 16 (2014) 20382-20386.

[5] O. Carp, Photoinduced reactivity of titanium dioxide, Progress in Solid State Chemistry, 32 (2004) 33-177.

[6] M. Pelaez, N.T. Nolan, S.C. Pillai, M.K. Seery, P. Falaras, A.G. Kontos, P.S.M. Dunlop, J.W.J. Hamilton, J.A. Byrne, K. O'Shea, M.H. Entezari, D.D. Dionysiou, A review on the visible light active titanium dioxide photocatalysts for environmental applications, Applied Catalysis B: Environmental, 125 (2012) 331-349.

[7] E. P. Meagher, G. A. Lager, Polyhedral thermal expansion in the TiO2 polymorphs: Refinement of the crystal structures of rutile and brookite at high temperature, 1979.

[8] S. Kumar, S. Bhunia, A.K. Ojha, Effect of calcination temperature on phase transformation, structural and optical properties of sol–gel derived ZrO_2 nanostructures, Physica E: Low-dimensional Systems and Nanostructures, 66 (2015) 74-80.

[9] J.D. McCullough, K.N. Trueblood, The crystal structure of baddeleyite (monoclinic ZrO2), Acta Crystallographica, 12 (1959) 507-511.

[10] C. Gautam, J. Joyner, A. Gautam, J. Rao, R. Vajtai, Zirconia based dental ceramics: structure, mechanical properties, biocompatibility and applications, Dalton Transactions, 45 (2016) 19194-19215.

[11] R.H. French, S.J. Glass, F.S. Ohuchi, Y.N. Xu, W.Y. Ching, Experimental and theoretical determination of the electronic structure and optical properties of three phases of ZrO_2, Physical Review B, 49 (1994) 5133-5142.

[12] R.E. Chhin, Ceramography: Preparation and Analysis of Ceramic Microstructures, (2002) 50.

[13] B.M. Reddy, A. Khan, Recent Advances on TiO_2-ZrO_2 Mixed Oxides as Catalysts and Catalyst Supports, Catalysis Reviews, 47 (2007) 257-296.

[14] A.S. Yasin, M. Obaid, M.H. El-Newehy, S.S. Al-Deyab, N.A.M. Barakat, Influence of $Ti_xZr_{(1-x)}O_2$ nanofibers composition on the photocatalytic activity toward organic pollutants degradation and water splitting, Ceramics International, 41 (2015) 11876-11885.

[15] J. Zhang, L. Li, Z. Xiao, D. Liu, S. Wang, J. Zhang, Y. Hao, W. Zhang, Hollow Sphere TiO_2–ZrO_2 Prepared by Self-Assembly with Polystyrene Colloidal Template for Both Photocatalytic Degradation and H_2 Evolution from Water Splitting, ACS Sustainable Chemistry & Engineering, 4 (2016) 2037-2046.

[16] J. Zhang, L. Li, J. Zhang, X. Zhang, W. Zhang, Controllable design of natural gully-like TiO_2-ZrO_2 composites and their photocatalytic degradation and hydrogen production by water splitting, New Journal of Chemistry, 41 (2017) 9113-9122.

[17] S. Chattopadhyay, S. Mondal, G. De, Hierarchical $Ti_{1-x}Zr_xO_{2-y}$ nanocrystals with exposed high energy facets showing co-catalyst free solar light driven water splitting and improved light to energy conversion efficiency, Journal of Materials Chemistry A, 5 (2017) 17341-17351.

[18] M.E. Manríquez, T. López, R. Gómez, J. Navarrete, Preparation of TiO_2–ZrO_2 mixed oxides with controlled acid–basic properties, Journal of Molecular Catalysis A: Chemical, 220 (2004) 229-237.

[19] K.-T. Li, C.-K. Wang, I. Wang, C.-M. Wang, Esterification of lactic acid over TiO_2–ZrO_2 catalysts, Applied Catalysis A: General, 392 (2011) 180-183.

[20] I. Wang, W.-F. Chang, R.-J. Shiau, J.-C. Wu, C.-S. Chung, Nonoxidative dehydrogenation of ethylbenzene over TiO_2-ZrO_2 catalysts, Journal of Catalysis, 83 (1983) 428-436.

[21] H. Tiainen, G. Eder, O. Nilsen, H.J. Haugen, Effect of ZrO_2 addition on the mechanical properties of porous TiO_2 bone scaffolds, Materials Science and Engineering: C, 32 (2012) 1386-1393.

[22] J. Si, J. Zhang, S. Liu, W. Zhang, D. Yu, X. Wang, L. Guo, S.G. Shen, Characterization of a micro-roughened TiO_2/ZrO_2 coating: mechanical properties and HBMSC responses in vitro, Acta biochimica et biophysica Sinica, 46 (2014) 572-581.

[23] B.-W. Kwak, B.-S. Kim, I.-J. Shon, Enhanced mechanical properties and fast consolidation of a nanostructured Ti–ZrO_2 composite by pulsed current activated heating, Ceramics International, 42 (2016) 4621-4626.

[24] A. Kitiyanan, S. Ngamsinlapasathian, S. Pavasupree, S. Yoshikawa, The preparation and characterization of nanostructured TiO_2–ZrO_2 mixed oxide electrode for efficient dye-sensitized solar cells, Journal of Solid State Chemistry, 178 (2005) 1044-1048.

[25] A. Kitiyanan, S. Yoshikawa, The use of ZrO_2 mixed TiO_2 nanostructures as efficient dye-sensitized solar cells' electrodes, Materials Letters, 59 (2005) 4038-4040.

[26] I.M.A. Mohamed, V.-D. Dao, N.A.M. Barakat, A.S. Yasin, A. Yousef, H.-S. Choi, Efficiency enhancement of dye-sensitized solar cells by use of ZrO_2-doped TiO_2 nanofibers photoanode, Journal of Colloid and Interface Science, 476 (2016) 9-19.

[27] M. Dürr, S. Rosselli, A. Yasuda, G. Nelles, Band-Gap Engineering of Metal Oxides for Dye-Sensitized Solar Cells, The Journal of Physical Chemistry B, 110 (2006) 21899-21902.

[28] V. Paranthaman, S.p. Muthu, P. Alagarsamy, H.n. Ming, R. Perumalsamy, Influence of zirconium dioxide and titanium dioxide binders on the photovoltaic performance of dye sensitized solar cell tungsten carbide nanorods based counter electrode, Electrochimica Acta, 211 (2016) 375-384.

[29] K. Tsougeni, P. Zerefos, A. Tserepi, A. Vlahou, S.D. Garbis, E. Gogolides, TiO_2-ZrO_2 affinity chromatography polymeric microchip for phosphopeptide enrichment and separation, Lab on a Chip, 11 (2011) 3113-3120.

[30] Q. Wu, D. Wu, Y. Guan, Hybrid Titania–Zirconia Nanoparticles Coated Adsorbent for Highly Selective Capture of Nucleosides from Human Urine in Physiological Condition, Analytical Chemistry, 86 (2014) 10122-10130.

[31] J. Choi, A. Ide, Y.B. Truong, I.L. Kyratzis, R.A. Caruso, High surface area mesoporous titanium-zirconium oxide nanofibrous web: a heavy metal ion adsorbent, Journal of Materials Chemistry A, 1 (2013) 5847-5853.

[32] G.L. Drisko, V. Luca, E. Sizgek, N. Scales, R.A. Caruso, Template Synthesis and Adsorption Properties of Hierarchically Porous Zirconium Titanium Oxides, Langmuir, 25 (2009) 5286-5293.

[33] M.C. Kimling, D. Chen, R.A. Caruso, Temperature-induced modulation of mesopore size in hierarchically porous amorphous TiO_2/ZrO_2 beads for improved dye adsorption capacity, Journal of Materials Chemistry A, 3 (2015) 3768-3776.

[34] A. Sotto, J. Kim, J.M. Arsuaga, G. del Rosario, A. Martinez, D. Nam, P. Luis, B. Van der Bruggen, Binary metal oxides for composite ultrafiltration membranes, Journal of Materials Chemistry A, 2 (2014) 7054-7064.

[35] H. Guo, S. Zhao, X. Wu, H. Qi, Fabrication and characterization of TiO_2/ZrO_2 ceramic membranes for nanofiltration, Microporous and Mesoporous Materials, (2016).

[36] Y. Lu, T. Chen, X. Chen, M. Qiu, Y. Fan, Fabrication of TiO_2-doped ZrO_2 nanofiltration membranes by using a modified colloidal sol-gel process and its application in simulative radioactive effluent, Journal of Membrane Science, 514 (2016) 476-486.

[37] U. Aust, S. Benfer, M. Dietze, A. Rost, G. Tomandl, Development of microporous ceramic membranes in the system TiO_2/ZrO_2, Journal of Membrane Science, 281 (2006) 463-471.

[38] R. Pérez-Hernández, D. Mendoza-Anaya, M.E. Fernández, A. Gómez-Cortés, Synthesis of mixed ZrO_2–TiO_2 oxides by sol–gel: Microstructural characterization and infrared spectroscopy studies of NO_x, Journal of Molecular Catalysis A: Chemical, 281 (2008) 200-206.

[39] J. Xu, C. Lind, A.P. Wilkinson, S. Pattanaik, X-ray Diffraction and X-ray Absorption Spectroscopy Studies of Sol−Gel-Processed Zirconium Titanates, Chemistry of Materials, 12 (2000) 3347-3355.

[40] H. Zou, Y.S. Lin, Structural and surface chemical properties of sol–gel derived TiO_2–ZrO_2 oxides, Applied Catalysis A: General, 265 (2004) 35-42.

[41] V. Vishwanathan, H.-S. Roh, J.-W. Kim, K.-W. Jun, Surface Properties and Catalytic Activity of TiO_2–ZrO_2 Mixed Oxides in Dehydration of Methanol to Dimethyl Ether, Catalysis Letters, 96 (2004) 23-28.

[42] A. Burri, N. Jiang, S.-E. Park, High surface area TiO_2-ZrO_2 prepared by caustic solution treatment, and its catalytic efficiency in the oxidehydrogenation of para-ethyltoluene by CO_2, Catalysis Science & Technology, 2 (2012) 514-520.

[43] D.Q. Xiao, G. He, M. Liu, J. Gao, P. Jin, S.S. Jiang, W.D. Li, M. Zhang, Y.M. Liu, J.G. Lv, Z.Q. Sun, Modification of optical and electrical properties of sol-gel-derived TiO_2-doped ZrO_2 gate dielectrics by annealing temperature, Journal of Alloys and Compounds, 688 (2016) 252-259.

[44] S.J. Pfleiderer, D. Lützenkirchen-Hecht, R. Frahm, Crystallization behaviour of TiO_2–ZrO_2 composite nanoparticles, Journal of Sol-Gel Science and Technology, 64 (2012) 27-35.

[45] T. Noguchi, M. Mizuno, Phase Changes in the ZrO_2-TiO_2 system, BULLETIN OF THE CHEMICAL OF JAPAN, 41 (1968) 2895-2899.

[46] L.Y. Zhu, G. Yu, X.Q. Wang, D. Xu, Preparation, phase transformation and microstructure of ZrxTi1−xO2 (x=0.1–0.9) fine fibers, Journal of Non-Crystalline Solids, 355 (2009) 68-71.

[47] A. Kitiyanan, S. Sakulkhaemaruethai, Y. Suzuki, S. Yoshikawa, Structural and photovoltaic properties of binary TiO_2–ZrO_2 oxides system prepared by sol–gel method, Composites Science and Technology, 66 (2006) 1259-1265.

[48] L. Liang, Y. Sheng, Y. Xu, D. Wu, Y. Sun, Optical properties of sol–gel derived ZrO_2–TiO_2 composite films, Thin Solid Films, 515 (2007) 7765-7771.

[49] C. Gionco, A. Battiato, E. Vittone, M.C. Paganini, E. Giamello, Structural and spectroscopic properties of high temperature prepared ZrO_2–TiO_2 mixed oxides, Journal of Solid State Chemistry, 201 (2013) 222-228.

[50] A. Pasche, B. Grohe, S. Mittler, P.A. Charpentier, Zr-doped TiO_2 nanoparticles synthesized via a sol–gel route and their application in dye-sensitized solar cells for thermo-stabilization, Materials Research Express, 4 (2017) 065501.

[51] J.-Y. Kim, C.-S. Kim, H.-K. Chang, T.-O. Kim, Effects of ZrO_2 addition on phase stability and photocatalytic activity of ZrO_2/TiO_2 nanoparticles, Advanced Powder Technology, 21 (2010) 141-144.

[52] J. Wang, Y. Yu, S. Li, L. Guo, E. Wang, Y. Cao, Doping Behavior of Zr^{4+} Ions in Zr^{4+}-Doped TiO2 Nanoparticles, The Journal of Physical Chemistry C, 117 (2013) 27120-27126.

[53] F. Dachille, P.Y. Simons, R. Roy, Pressure-temperature studies of anatase, brookite, rutile and TiO_2-II, The armerican mineralogist, 53 (1968) 1929-1939.

[54] K.Y. Jung, S.B. Park, Photoactivity of SiO_2/TiO_2 and ZrO_2/TiO_2 mixed oxides prepared by sol–gel method, Materials Letters, 58 (2004) 2897-2900.

[55] M.D. Hernández-Alonso, I. Tejedor-Tejedor, J.M. Coronado, J. Soria, M.A. Anderson, Sol–gel preparation of TiO_2–ZrO_2 thin films supported on glass rings: Influence of phase composition on photocatalytic activity, Thin Solid Films, 502 (2006) 125-131.

[56] B.-T. Lee, J.-K. Han, A.K. Gain, K.-H. Lee, F. Saito, TEM microstructure characterization of nano TiO_2 coated on nano ZrO_2 powders and their photocatalytic activity, Materials Letters, 60 (2006) 2101-2104.

[57] B. Neppolian, Q. Wang, H. Yamashita, H. Choi, Synthesis and characterization of ZrO_2–TiO_2 binary oxide semiconductor nanoparticles: Application and interparticle electron transfer process, Applied Catalysis A: General, 333 (2007) 264-271.

[58] M.E. Manríquez, T. López, D.H. Aguilar, P. Quintana, Phase Structure and Thermal Evolution in Mixed Oxide TiO_2-ZrO_2 Powders Obtained by the Sol-Gel Process, in: T.M. López, D. Avnir, M. Aegerter (Eds.) Emerging Fields in Sol-Gel Science and Technology, Springer US, Boston, MA, 2003, pp. 254-264.

[59] M. Daturi, A. Cremona, F. Milella, G. Busca, E. Vogna, Characterisation of zirconia-titania powders prepared by coprecipitation, Journal of the European Ceramic Society, 18 (1998) 1079-1087.

[60] N. Takahashi, A. Suda, I. Hachisuka, M. Sugiura, H. Sobukawa, H. Shinjoh, Sulfur durability of NO_x storage and reduction catalyst with supports of TiO_2, ZrO_2 and ZrO_2-TiO_2 mixed oxides, Applied Catalysis B: Environmental, 72 (2007) 187-195.

[61] I. Wang, J.-c. Wu, C.-s. Chung, Dehydrogenation of ethylbenzene and ethylcyclohexane over mixed binary oxide catalysts containing titania, Applied Catalysis, 16 (1985) 89-101.

[62] J. Miciukiewicz, T. Mang, H. Knözinger, Raman spectroscopy characterization of molybdena supported on titania-zirconia mixed oxide, Applied Catalysis A: General, 122 (1995) 151-159.

[63] D. Mao, Q. Chen, G. Lu, Vapor-phase Beckmann rearrangement of cyclohexanone oxime over B_2O_3/TiO_2-ZrO_2, Applied Catalysis A: General, 244 (2003) 273-282.

[64] P. Afanasiev, Mixed TiO_2–ZrO_2 support for hydrotreating, obtained by co-precipitation from Zr basic carbonate and Ti oxosulfate, Catalysis Communications, 9 (2008) 734-739.

[65] H. Koohestani, M. Alinejad, S.K. Sadrnezhaad, Characterization of TiO_2-ZrO_2 nanocomposite prepared by co-precipitation method, Advances in Nanocomposite Research, (2015) -.

[66] B. Liu, X. Li, Q. Zhao, J. Ke, J. Liu, S. Liu, M. Tade, Photocatalytic degradation of gaseous toluene with multiphase $Ti_xZr_{1-x}O_2$ synthesized via co-precipitation route, J Colloid Interface Sci, 438 (2015) 1-6.

[67] J.H. Schattka, D.G. Shchukin, J. Jia, M. Antonietti, R.A. Caruso, Photocatalytic Activities of Porous Titania and Titania/Zirconia Structures Formed by Using a Polymer Gel Templating Technique, Chemistry of Materials, 14 (2002) 5103-5108.

[68] M. Li, X. Li, G. Jiang, G. He, Hierarchically macro–mesoporous ZrO_2–TiO_2 composites with enhanced photocatalytic activity, Ceramics International, 41 (2015) 5749-5757.

[69] M. Ghiaci, H. Aghaei, A. Abbaspur, Size-controlled synthesis of ZrO_2–TiO_2 nanoparticles prepared via reverse micelle method: Investigation of particle size effect on the catalytic performance in vapor phase Beckmann rearrangement, Materials Research Bulletin, 43 (2008) 1255-1262.

[70] L. Kokporka, S. Onsuratoom, T. Puangpetch, S. Chavadej, Sol–gel-synthesized mesoporous-assembled TiO_2–ZrO_2 mixed oxide nanocrystals and their photocatalytic sensitized H_2 production activity under visible light irradiation, Materials Science in Semiconductor Processing, 16 (2013) 667-678.

[71] Q. Luo, Q.-z. Cai, X.-w. Li, Z.-h. Pan, Y.-j. Li, X.-d. Chen, Q.-s. Yan, Preparation and characterization of ZrO_2/TiO_2 composite photocatalytic film by micro-arc oxidation, Transactions of Nonferrous Metals Society of China, 23 (2013) 2945-2950.

[72] Y. Huang, Z. Zheng, Z. Ai, L. Zhang, X. Fan, Z. Zou, Core−Shell Microspherical $Ti_{1-x}Zr_xO_2$ Solid Solution Photocatalysts Directly from Ultrasonic Spray Pyrolysis, The Journal of Physical Chemistry B, 110 (2006) 19323-19328.

[73] J.G. Weissman, E.I. Ko, S. Kaytal, Titania-zirconia mixed oxide aerogels as supports for hydrotreating catalysts, Applied Catalysis A: General, 94 (1993) 45-59.

[74] A. Kambur, G.S. Pozan, I. Boz, Preparation, characterization and photocatalytic activity of TiO_2–ZrO_2 binary oxide nanoparticles, Applied Catalysis B: Environmental, 115–116 (2012) 149-158.

[75] A. Ulatowska-Jarza, D. Andrzejewski, K. Maruszewski, H. Podbielska, W. Strek, Advantages of sol-gel technologies for biomedical applications, in, 1999, pp. 50-58.

[76] G.J. Owens, R.K. Singh, F. Foroutan, M. Alqaysi, C.-M. Han, C. Mahapatra, H.-W. Kim, J.C. Knowles, Sol–gel based materials for biomedical applications, Progress in Materials Science, 77 (2016) 1-79.

[77] C.J. Brinker, G.W. Scherer, CHAPTER 4 - Particulate Sols and Gels, in: Sol-Gel Science, Academic Press, San Diego, 1990, pp. 234-301.

[78] C.J. Brinker, D.M. Smith, R. Deshpande, P.M. Davis, S. Hietala, G.C. Frye, C.S. Ashley, R.A. Assink, Sol-gel processing of controlled pore oxides, Catalysis Today, 14 (1992) 155-163.

[79] J. Livage, M. Henry, C. Sanchez, Sol-gel chemistry of transition metal oxides, Progress in Solid State Chemistry, 18 (1988) 259-341.

[80] D.C. Bradley, A Structural Theory for Metal Alkoxide Polymers, Nature, 182 (1958) 1211-1214.

[81] R. Corriu, N.T. Anh, Molecular Chemistry of Sol-Gel Derived Nanomaterials, John Wiley &Sons, Ltd, 2009.

[82] E.G. Seebauer, M.C. Kratzer, Charged Semiconductor Defects : Structure, Thermodynamics and Diffusion, Springer London, 2009.

[83] M. Niederberger, N. Pinna, Metal Oxide Nanoparticles in Organic Solvents : Synthesis, Formation, Assembly and Application, in, Springer London, 2009.

[84] A.C. Pierre, Introduction to Sol-Gel Processing, Kluwer Academic Publishers, 1998.

[85] C.J. Brinker, G.W. Scherer, Sol-gel Science: The Physics and Chemistry of Sol-gel Processing, Academic Press Inc, 1990.

[86] A.E. Danks, S.R. Hall, Z. Schnepp, The evolution of 'sol-gel' chemistry as a technique for materials synthesis, Materials Horizons, 3 (2016) 91-112.

[87] P. Jittiarporn, S. Badilescu, M.N. Al Sawafta, L. Sikong, V.-V. Truong, Electrochromic properties of sol–gel prepared hybrid transition metal oxides – A short review, Journal of Science: Advanced Materials and Devices, 2 (2017) 286-300.

[88] B.M. Pirzada, N.A. Mir, N. Qutub, O. Mehraj, S. Sabir, M. Muneer, Synthesis, characterization and optimization of photocatalytic activity of TiO_2/ZrO_2 nanocomposite heterostructures, Materials Science and Engineering: B, 193 (2015) 137-145.

[89] S. Aghabeygi, N. Farhadyar, K. Jalili, Preparation and Characterization of ZrO_2/TiO_2 Nanocomposite under Ultrasonic Irradiation by Sol-gel Route, International Journal of Bio-Inorganic Hybrid Nanomaterials, 3 (2014) 175-178.

[90] R.F. de Farias, C. Airoldi, Spherical Particles of Zirconia–Titania of Hexagonal Structure from a Neutral Amine Route, Journal of Colloid and Interface Science, 220 (1999) 255-259.

[91] L. Rayleigh, X., On the electromagnetic theory of light, Philosophical Magazine Series 5, 12(73) (1881) 81 - 101.

[92] H.C. Van de Hulst, Light scattering by small particles, WILEY: NY, (1957).

[93] A. Soloviev, Procedé Sol-Gel : Etude par diffusion de la lumière de la cinétique de croissance des particules pendant l'hydrolyse-condensation de l'isopropoxyde de titane (IV), Thèse de doctorat de l'Université Paris 13, (2000).

[94] A. Soloviev, H. Jensen, E.G. Søgaard, A.V. Kanaev, Aggregation kinetics of sol-gel process based on titanium tetraisopropoxide, Journal of Materials Science, 38 (2003) 3315-3318.

[95] M. Rivallin, M. Benmami, A. Gaunand, A. Kanaev, Temperature dependence of the titanium oxide sols precipitation kinetics in the sol–gel process, Chemical Physics Letters, 398 (2004) 157-162.

[96] A. Einstein, Über die von der molekularkinetischen Theorie der Wärme geforderte Bewegung von in ruhenden Flüssigkeiten suspendierten Teilchen, Annalen der Physik, 322(8) (1905) 549-560.

[97] B.J. Berne, R. Pecora, Dynamic Light Scattering: With Applications to Chemistry, Biology, and Physics, (1990).

[98] H.Z. Cummins, Photon Correlation and Light Beating Spectroscopy, in, Plenum Press, 1974, pp. 285-330.

[99] R. Pecora, Dynamic Light Scattering Measurement of Nanometer Particles in Liquids, Journal of Nanoparticle Research, 2 (2000) 123-131.

[100] R.J. Glauber, Coherent and Incoherent States of the Radiation Field, Physical Review, 131 (1963) 2766.

[101] S. TIENG, Elaboration de Fe(III)-TiO_2 pardopage des clusters oxo-TiO_2 dans un réacteur sol-gelà micromélange Application en photocatalyse, Thesis, (2011).

[102] R. Azouani, A. Soloviev, M. Benmami, K. Chhor, J.F. Bocquet, A. Kanaev, Stability and Growth of Titanium-oxo-alkoxy $Ti_xO_y(O^iPr)_z$ Clusters, The Journal of Physical Chemistry C, 111 (2007) 16243-16248.

[103] R. Azouani, S. Tieng, K. Chhor, J.F. Bocquet, P. Eloy, E.M. Gaigneaux, K. Klementiev, A.V. Kanaev, TiO_2 doping by hydroxyurea at the nucleation stage: towards a new photocatalyst in the visible spectral range, Physical Chemistry Chemical Physics, 12 (2010) 11325-11334.

[104] S. Tieng, R. Azouani, K. Chhor, A. Kanaev, Nucleation–Growth of TiO_2 Nanoparticles Doped with Iron Acetylacetonate, The Journal of Physical Chemistry C, 115 (2011) 5244-5250.

[105] S. Labidi, Z. Jia, M.B. Amar, K. Chhor, A. Kanaev, Nucleation and growth kinetics of zirconium-oxo-alkoxy nanoparticles, Physical Chemistry Chemical Physics, 17 (2015) 2651-2659.

[106] J.S. Chappell, L.J. Procopio, J.D. Birchall, Observations on modifying particle formation in the hydrolysis of titanium (IV) tetra-ethoxide, Journal of Materials Science Letters, 9 (1990) 1329-1331.

[107] M. Rivallin, Evolution de sols nanométriques d'oxyde de titane durant l'induction d'une précipitation de type sol-gel en réacteur à mélangeur rapide : Mesures granulométriques in-situ et modélisation, in, Thèse de doctorat de l'Ecole des Mines de Paris, 2003.

[108] M. Rivallin, M. Benmami, A. Kanaev, A. Gaunand, Sol–Gel Reactor With Rapid Micromixing, Chemical Engineering Research and Design, 83 (2005) 67-74.

[109] R. AZOUANI, Elaboration de nouveaux nanomatériaux photocatalytiques actifs sous rayonnement visible Thesis, (2009).

[110] R. Azouani, A. Michau, K. Hassouni, K. Chhor, J.F. Bocquet, J.L. Vignes, A. Kanaev, Elaboration of pure and doped TiO_2 nanoparticles in sol–gel reactor with turbulent micromixing: Application to nanocoatings and photocatalysis, Chemical Engineering Research and Design, 88 (2010) 1123-1130.

[111] K. Oualha, M. Ben Amar, A. Michau, A. Kanaev, Observation of cavitation in exocentric T-mixer, Chemical Engineering Journal, 321 (2017) 146-150.

[112] S. Tieng, O. Brinza, K. Chhor, A. Kanaev, Nucleation and fractal growth of zirconium oxo-alkoxy nanoparticles at the induction stage of sol–gel process, Journal of Sol-Gel Science and Technology, 64 (2012) 145-148.

[113] S. LABIDI, Elaboration des nanoparticules d'oxyde de zirconium par voie sol-gel : Mise en forme et application pour la synthèse de biodiesel, Thesis (2015).

[114] M. Benmami, Evolution de sols nanométriques d'oxydes de titane durant l'induction d'une précipitation de type sol-gel en réacteur à mélangeur rapide: Mesures Granulométriques in-situ et modélisation., (2003, Ecole des mines de Paris.).

[115] H. Hartridge, F.J.W. Roughton, A Method of Measuring the Velocity of Very Rapid Chemical Reactions, Proceedings of the Royal Society of London. Series A, 104 (1923) 376.

[116] Y. Gnatyuk, N. Smirnova, O. Korduban, A. Eremenko, Effect of zirconium incorporation on the stabilization of TiO_2 mesoporous structure, Surface and Interface Analysis, 42 (2010) 1276-1280.

[117] H. Zhang, S. Ruan, C. Feng, B. Xu, W. Chen, W. Dong, Photoelectric Properties of TiO_2-ZrO_2 Thin Films Prepared by Sol-Gel Method, Journal of Nanoscience and Nanotechnology, 11 (2011) 10003-10006.

[118] N. Smirnova, Y. Gnatyuk, A. Eremenko, G. Kolbasov, V. Vorobetz, I. Kolbasova, O. Linyucheva, Photoelectrochemical characterization and photocatalytic properties of mesoporousTiO_2/ZrO_2 films, International Journal of Photoenergy, 2006 (2006) 1-6.

[119] V. Polliotto, E. Albanese, S. Livraghi, P. Indyka, Z. Sojka, G. Pacchioni, E. Giamello, Fifty–Fifty Zr–Ti Solid Solution with a TiO_2-Type Structure: Electronic Structure and Photochemical Properties of Zirconium Titanate $ZrTiO_4$, The Journal of Physical Chemistry C, 121 (2017) 5487-5497.

[120] D.G. Mieritz, A. Renaud, D.-K. Seo, Unusual Changes in Electronic Band-Edge Energies of the Nanostructured Transparent n-Type Semiconductor Zr-Doped Anatase TiO_2 ($Ti_{1-x}Zr_xO_2$; $x < 0.3$), Inorganic Chemistry, 55 (2016) 6574-6585.

[121] Y. Boyjoo, H. Sun, J. Liu, V.K. Pareek, S. Wang, A review on photocatalysis for air treatment: From catalyst development to reactor design, Chemical Engineering Journal, 310 (2017) 537-559.

[122] S.M. Gupta, M. Tripathi, A review of TiO_2 nanoparticles, Chinese Science Bulletin, 56 (2011) 1639-1657.

[123] C. Wu, X. Zhao, Y. Ren, Y. Yue, W. Hua, Y. Cao, Y. Tang, Z. Gao, Gas-phase photo-oxidations of organic compounds over different forms of zirconia, Journal of Molecular Catalysis A: Chemical, 229 (2005) 233-239.

[124] C. Karunakaran, S. Senthilvelan, Photocatalysis with ZrO2: oxidation of aniline, Journal of Molecular Catalysis A: Chemical, 233 (2005) 1-8.

[125] S. Kumar, A.K. Ojha, Oxygen vacancy induced photoluminescence properties and enhanced photocatalytic activity of ferromagnetic ZrO2 nanostructures on methylene blue dye under ultra-violet radiation, Journal of Alloys and Compounds, 644 (2015) 654-662.

[126] L. Renuka, K.S. Anantharaju, S.C. Sharma, H. Nagabhushana, Y.S. Vidya, H.P. Nagaswarupa, S.C. Prashantha, A comparative study on the structural, optical, electrochemical and photocatalytic properties of ZrO 2 nanooxide synthesized by different routes, Journal of Alloys and Compounds, 695 (2017) 382-395.

[127] I.K. Konstantinou, T.A. Albanis, TiO_2-assisted photocatalytic degradation of azo dyes in aqueous solution: kinetic and mechanistic investigations, Applied Catalysis B: Environmental, 49 (2004) 1-14.

[128] S. Tieng, A. Kanaev, K. Chhor, New homogeneously doped Fe(III)–TiO_2 photocatalyst for gaseous pollutant degradation, Applied Catalysis A: General, 399 (2011) 191-197.

[129] J. Bałdyga, R. Pohorecki, Turbulent micromixing in chemical reactors — a review, The Chemical Engineering Journal and the Biochemical Engineering Journal, 58 (1995) 183-195.

[130] X. Fu, L.A. Clark, Q. Yang, M.A. Anderson, Enhanced Photocatalytic Performance of Titania-Based Binary Metal Oxides: TiO_2/SiO_2 and TiO_2/ZrO_2, Environmental Science & Technology, 30 (1996) 647-653.

[131] S.W. Liu, C.F. Song, M.K. Lü, S.F. Wang, D.L. Sun, Y.X. Qi, D. Xu, D.R. Yuan, A novel $TiO_2/Zr_xTi_{1-x}O_2$ composite photocatalytic films, Catalysis Communications, 4 (2003) 343-346.

[132] Y. Gnatyuk, N. Smirnova, A. Eremenko, V. Ilyin, Design and Photocatalytic Activity of Mesoporous TiO_2/ZrO_2 Thin Films, Adsorption Science & Technology, 23 (2005) 497-508.

[133] B. Wu, R. Yuan, X. Fu, Structural characterization and photocatalytic activity of hollow binary ZrO_2/TiO_2 oxide fibers, Journal of Solid State Chemistry, 182 (2009) 560-565.

[134] Q. Yuan, Y. Liu, L.-L. Li, Z.-X. Li, C.-J. Fang, W.-T. Duan, X.-G. Li, C.-H. Yan, Highly ordered mesoporous titania–zirconia photocatalyst for applications in degradation of rhodamine-B and hydrogen evolution, Microporous and Mesoporous Materials, 124 (2009) 169-178.

[135] C.-C. Ou, C.-S. Yang, S.-H. Lin, Selective photo-degradation of Rhodamine B over zirconia incorporated titania nanoparticles: a quantitative approach, Catalysis Science & Technology, 1 (2011) 295-307.

[136] J.C. Yu, J. Lin, R.W.M. Kwok, $Ti_{1-x}Zr_xO_2$ Solid Solutions for the Photocatalytic Degradation of Acetone in Air, The Journal of Physical Chemistry B, 102 (1998) 5094-5098.

[137] Q. Huang, W. Ma, X. Yan, Y. Chen, S. Zhu, S. Shen, Photocatalytic decomposition of gaseous HCHO by $Zr_xTi_{1-x}O_2$ catalysts under UV–vis light irradiation with an energy-saving lamp, Journal of Molecular Catalysis A: Chemical, 366 (2013) 261-265.

[138] G.N. Shao, S.M. Imran, S.J. Jeon, M. Engole, N. Abbas, M. Salman Haider, S.J. Kang, H.T. Kim, Sol–gel synthesis of photoactive zirconia–titania from metal salts and investigation of their photocatalytic properties in the photodegradation of methylene blue, Powder Technology, 258 (2014) 99-109.

[139] H. Liu, Y. Su, H. Hu, W. Cao, Z. Chen, An ionic liquid route to prepare mesoporous ZrO_2–TiO_2 nanocomposites and study on their photocatalytic activities, Advanced Powder Technology, 24 (2013) 683-688.

[140] I. Singh, R. Kumar, B.I. Birajdar, Zirconium doped TiO 2 nano-powder via halide free non-aqueous solvent controlled sol-gel route, Journal of Environmental Chemical Engineering, (2017).

[141] A. Weir, P. Westerhoff, L. Fabricius, K. Hristovski, N. von Goetz, Titanium Dioxide Nanoparticles in Food and Personal Care Products, Environmental Science & Technology, 46 (2012) 2242-2250.

[142] M. Dahl, Y. Liu, Y. Yin, Composite Titanium Dioxide Nanomaterials, Chemical Reviews, 114 (2014) 9853-9889.

[143] K. Nakata, A. Fujishima, TiO2 photocatalysis: Design and applications, Journal of Photochemistry and Photobiology C: Photochemistry Reviews, 13 (2012) 169-189.

[144] A. Guinier, X-Ray Diffraction: In Crystals, Imperfect Crystals, and Amorphous Bodies, Dove Publications, 1994.

[145] N. Hwang, A.R. Barron, BET Surface Area Analysis of Nanoparticles http://cnx.org/contents/9cBY4EHy@1/BET-Surface-Area-Analysis-of-N.

[146] E.A. Davis, N.F. Mott, Conduction in non-crystalline systems V. Conductivity, optical absorption and photoconductivity in amorphous semiconductors, The Philosophical Magazine: A Journal of Theoretical Experimental and Applied Physics, 22 (1970) 0903-0922.

[147] E. Sanchez, T. Lopez, Effect of the preparation method on the band gap of titania and platinum-titania sol-gel materials, Materials Letters, 25 (1995) 271-275.

[148] Chemiasoft, Inductively Coupled Plasma Optical Emission Spectrometry (ICP-OES), http://www.chemiasoft.com/chemd/node/52.

[149] C.J. Brinker, G.W. Scherer, The Physics and Chemistry of Sol-Gel Processing. Academic Press, New-York, in, Academic Press, San Diego, 1990, pp. xvi-18.

[150] A.C. Pierre, Introduction to Sol-Gel Processing, Kluwer Int. Ser. in Sol-Gel Processing: Technology and Applications, (1998).

[151] G.A. Seisenbaeva, V.G. Kessler, Precursor directed synthesis - "molecular" mechanisms in the Soft Chemistry approaches and their use for template-free synthesis of metal, metal oxide and metal chalcogenide nanoparticles and nanostructures, Nanoscale, 6 (2014) 6229-6244.

[152] V.G. Kessler, The chemistry behind the sol–gel synthesis of complex oxide nanoparticles for bio-imaging applications, Journal of Science Education and Technology, 51 (2009) 264–271.

[153] G.A. Seisenbaeva, V.G. Kessler, R. Pazik, W. Strek, Dalton Trans., (2008) 3412.

[154] L. Rozes, N. Steunou, G. Fornasieri, C. Sanchez, Monatshefte für Chemie, 137 (2006) 501.

[155] B. Pattier, M. Henderson, G. Brotons, A. Gibaud, Study of Titanium Oxide Sol–Gel Condensation Using Small Angle X-ray Scattering, The Journal of Physical Chemistry B, 114 (2010) 5227-5232.

[156] M.R. Mohammadi, D.J. Fray, Synthesis and characterisation of nanosized TiO_2–ZrO_2 binary system prepared by an aqueous sol–gel process: Physical and sensing properties, Sensors and Actuators B: Chemical, 155 (2011) 568-576.

[157] Q. Xu, M.A. Anderson, Sol–Gel Route to Synthesis of Microporous Ceramic Membranes: Preparation and Characterization of Microporous TiO_2 and ZrO_2 Xerogels, Journal of the American Ceramic Society, 77 (1994) 1939–1945.

[158] G.A. Seisenbaeva, V.G. Kessler, R. Pazik, W. Strek, Heteroleptic metal alkoxide “oxoclusters” as molecular models for the sol–gel synthesis of perovskite nanoparticles for bio-imaging applications, Dalton Transtions, (2008) 3412-3421

[159] K. Cheng, K. Chhor, A. Kanaev, Solvent effect on nucleation-growth of titanium-oxo-alkoxy nanoparticles, Chemical Physics Letters, 672 (2017) 119-123.

[160] S. Labidi, M. Ben Amar, J.P. Passarello, B. Le Neindre, A. Kanaev, Design of Novel Sulfated Nanozirconia Catalyst for Biofuel Synthesis, Industrial & Engineering Chemistry Research, 56 (2017) 1394-1403.

[161] M. Bouslama, M.C. Amamra, Z. Jia, M. Ben Amar, K. Chhor, O. Brinza, M. Abderrabba, J.L. Vignes, A. Kanaev, Nanoparticulate TiO_2–Al_2O_3 Photocatalytic Media: Effect of Particle Size and Polymorphism on Photocatalytic Activity, ACS Catalysis, 2 (2012) 1884-1892.

[162] H. Yutaka, N. Katsuhiko, M. Akihiko, T. Hideyasu, U. Akifumi, N. Hirotoshi, Role of Ti–O–Zr Bonding in TiO_2–ZrO_2 Catalyst for Dehydrogenation of Ethylbenzene, Bulletin of the Chemical Society of Japan, 61 (1988) 1945-1951.

[163] A. Soloviev, Procedé Sol-Gel : Etude par diffusion de la lumière de la cinétique de croissance des particules pendant l'hydrolyse-condensation de l'isopropoxyde de titane (IV), in, Thèse de doctorat de l'Université Paris 13, 2000.

[164] V.G. Kessler, The chemistry behind the sol–gel synthesis of complex oxide nanoparticles for bio-imaging applications, Journal of Sol-Gel Science and Technology, 51 (2009) 264-271.

[165] G.A. Seisenbaeva, V.G. Kessler, R. Pazik, W. Strek, Heteroleptic metal alkoxide "oxoclusters" as molecular models for the sol-gel synthesis of perovskite nanoparticles for bio-imaging applications, Dalton Transactions, (2008) 3412-3421.

[166] L. Lutterotti, P. Scardi, Simultaneous structure and size–strain refinement by the Rietveld method, Journal of Applied Crystalography, 23 (1990) 246-252.

[167] M. Horn, C.F. Schwerdtfeger, E.P. Meagher, Refinement of the structure of anatase at several temperatures, Zeitschrift für Kristallographie, 273-281 (1972).

[168] P. Bordet, A. McHale, A. Santoro, R.S. Roth, Powder neutron diffraction study of $ZrTiO_4$, $Zr_5Ti_7O_{24}$, and $FeNb_2O_6$, Journal of Solid State Chemistry, 64 (1986) 30-46.

[169] H.H. Kisi, C.J. Howard, R.J. Hill, Crystal Structure of Orthorhombic Zirconia in Partially Stabilized Zirconia, Journal of the American Ceramic Society, 72 (1989) 1757–1760

[170] S.v. Näray-Szabo, Zur Struktur des Baddeleyits ZrO_2, Zeitschrift für Kristallographie, 94 (1936) 414-416.

[171] U. Troitzsch, D.J. Ellis, The ZrO_2-TiO_2 phase diagram, Journal of Materials Science, 24 (2005) 4571- 4577.

[172] S. Ananta, R. Tipakontitikul, T. Tunkasiri, Synthesis, formation and characterization of zirconium titanate (ZT) powders, Materials Letters, 57 (2003) 2637-2642.

[173] E. López-López, I. Santacruz, L. Leon-Reina, M.A.G. Aranda, R. Moreno, C. Baudín, Reaction sintered zirconium titanate–zirconia bulk materials from $3Y_2O_3$-stabilized zirconia and TiO_2. Phase composition and their potential for thermal shock applications, Journal of the European Ceramic Society, 32 (2012) 1205-1211.

[174] U. Troitzsch, A.G. Christy, D.J. Ellis, The crystal structure of disordered $(Zr,Ti)O_2$ solid solution including srilankite: evolution towards tetragonal ZrO_2 with increasing Zr, Physics and Chemistry of Minerals, 32 (2005) 504-514.

[175] O. Khatim, M. Amamra, K. Chhor, A.M.T. Bell, D. Novikov, D. Vrel, A. Kanaev, Amorphous–anatase phase transition in single immobilized TiO_2 nanoparticles, Chemical Physics Letters, 558 (2013) 53-56.

[176] M. Laniecki, M. Ignacik, Water–gas shift reaction over sulfided molybdenum catalysts supported on TiO_2–ZrO_2 mixed oxides, Catalysis Today, 116 (2006) 400-407.

[177] J. Lang, L. Matějová, I. Troppová, L. Čapek, J. Endres, S. Daniš, Novel synthesis of $Zr_xTi_{1-x}O_n$ mixed oxides using titanyl sulphate and pressurized hot and supercritical fluids, and their photocatalytic comparison with sol-gel prepared equivalents, Materials Research Bulletin, 95 (2017) 95-103.

[178] G.D. Sizgek, E. Sizgek, C.S. Griffith, V. Luca, Mesoporous Zirconium Titanium Oxides. Part 2: Synthesis, Porosity, and Adsorption Properties of Beads, Langmuir, 24 (2008) 12323-12330.

[179] H. Kazuhito, I. Hiroshi, F. Akira, TiO_2 Photocatalysis: A Historical Overview and Future Prospects, Japanese Journal of Applied Physics, 44 (2005) 8269.

[180] E.M. Jin, J.-Y. Park, X.G. Zhao, I.-H. Lee, S.M. Jeong, H.-B. Gu, Photovoltaic properties of TiO_2–ZrO_2 fiber composite electrodes for dye-sensitized solar cells, Materials Letters, 126 (2014) 281-284.

[181] M.D. Hernández-Alonso, J.M. Coronado, B. Bachiller-Baeza, M. Fernández-García, J. Soria, Influence of Structural and Surface Characteristics of $Ti_{1-x}Zr_xO_2$ Nanoparticles on the Photocatalytic Degradation of Methylcyclohexane in the Gas Phase, Chemistry of Materials, 19 (2007) 4283-4291.

[182] L. Österlund, A. Mattsson, M. Leideborg, G. Westin, Photodecomposition of Acetone on ZrO_x-TiO_2 Thin Films in O_2 Excess and Deficit Conditions, in Nanostructured Materials and Nanotechnology: Ceramic and Engineering Science Proceedings, 28 (2007).

[183] H. Koohestani, S.K. Sadrnezhaad, Improvement in TiO_2 photocatalytic performance by ZrO_2 nanocompositing and immobilizing, Desalination and Water Treatment, 57 (2016) 28450-28459.

[184] B.-F. GAO, Y. MA, Y.-A. CAO, Z.-J. GU, G.-J. ZHANG, J.-N. YAO, Preparation and Photocatalytic Properties of $Ti_{1-x}Zr_xO_2$ Solid Solution, Chinese Journal of Chemistry,, 25 (2007) 484-489.

[185] L. Wang, F. Yang, T. Ji, Q. Yang, X. Qi, H. Du, J. Sun, Preparation and characterization of $Ti_{1-x}Zr_xO_2/ZrO_2$ nanocomposite, Scripta Materialia, 58 (2008) 794-797.

[186] M. Babaei, C. Dehghanian, P. Taheri, M. Babaei, Effect of duty cycle and electrolyte additive on photocatalytic performance of TiO_2 -ZrO_2 composite layers prepared on CP Ti by micro arc oxidation method, Surface and Coatings Technology, 307 (2016) 554-564.

[187] I. Singh, R. Kumar, B.I. Birajdar, Zirconium doped TiO2 nano-powder via halide free non-aqueous solvent controlled sol-gel route, Journal of Environmental Chemical Engineering, 5 (2017) 2955-2963.

[188] T.W. Tibbitts, K.E. Cushman, X. Fu, M.A. Anderson, R.J. Bula, Factors controlling activity of zirconia-titania for photocatalytic oxidation of ethylene, Advances in Space Research, 22 (1998) 1443-1451.

[189] S. Kataoka, D.T. Tompkins, W.A. Zeltner, M.A. Anderson, Photocatalytic oxidation in the presence of microwave irradiation: observations with ethylene and water, Journal of Photochemistry and Photobiology A: Chemistry, 148 (2002) 323-330.

[190] G. Colón, M.C. Hidalgo, J.A. Navío, Effect of ZrO_2 incorporation and calcination temperature on the photocatalytic activity of commercial TiO_2 for salicylic acid and Cr(VI) photodegradation, Applied Catalysis A: General, 231 (2002) 185-199.

[191] D. Guerrero-Araque, D. Ramírez-Ortega, P. Acevedo-Peña, F. Tzompantzi, H.A. Calderón, R. Gómez, Interfacial charge-transfer process across ZrO_2-TiO_2 heterojunction and its impact on photocatalytic activity, Journal of Photochemistry and Photobiology A: Chemistry, 335 (2017) 276-286.

[192] T. Cai, Y. Liao, Z. Peng, Y. Long, Z. Wei, Q. Deng, Photocatalytic performance of TiO_2 catalysts modified by $H_3PW_{12}O_{40}$, ZrO_2 and CeO_2, Journal of Environmental Sciences, 21 (2009) 997-1004.

[193] N.A. Badli, R. Ali, W.A. Wan Abu Bakar, L. Yuliati, Role of heterojunction $ZrTiO_4/ZrTi_2O_6/TiO_2$ photocatalyst towards the degradation of paraquat dichloride and optimization study by Box–Behnken design, Arabian Journal of Chemistry, (2016).

[194] S.-m. Chang, R.-a. Doong, Characterization of Zr-Doped TiO_2 Nanocrystals Prepared by a Nonhydrolytic Sol−Gel Method at High Temperatures, The Journal of Physical Chemistry B, 110 (2006) 20808-20814.

[195] C. Sun, L. Liu, L. Qi, H. Li, H. Zhang, C. Li, F. Gao, L. Dong, Efficient fabrication of ZrO_2-doped TiO_2 hollow nanospheres with enhanced photocatalytic activity of rhodamine B degradation, J Colloid Interface Sci, 364 (2011) 288-297.

[196] S. Polisetti, P.A. Deshpande, G. Madras, Photocatalytic Activity of Combustion Synthesized ZrO_2 and ZrO_2–TiO_2 Mixed Oxides, Industrial & Engineering Chemistry Research, 50 (2011) 12915-12924.

[197] Y.I. Gnatyuk, V.I. Yatskiv, N.P. Smirnova, V.M. Granchak, A.M. Eremenko, PHOTOCATALYTIC PROPERTIES OF MESOPOROUS TiO_2/ZrO_2 FILMS IN

GAS-PHASE OXIDATION OF ALCOHOLS, Theoretical and Experimental Chemistry, 41 (2005) 354-359.

[198] D.T. Sponza, R. Oztekin, Treatment of olive mill wastewater by photooxidation with ZrO_2-doped TiO_2 nanocomposite and its reuse capability, Environmental Technology, 37 (2016) 865-879.

[199] J.-K. Han, F. Saito, J.-G. Park, B.-T. Lee, Synthesis and Photocatalytic Activity of TiO_2-ZrO_2 Nano-Sized Powders by Sol-Gel Process, Journal of the Korean Ceramic Society, 42 (2005) 7-10.

[200] A.M. Alotaibi, S. Sathasivam, I.P. Parkin, Aerosol assisted chemical vapour deposition of a ZrO_2-TiO_2 composite thin film with enhanced photocatalytic activity, RSC Advances, 5 (2015) 67944-67950.

[201] L. Das, J.K. Basu, Photocatalytic treatment of textile effluent using titania–zirconia nano composite catalyst, Journal of Industrial and Engineering Chemistry, 24 (2015) 245-250.

[202] P. Goswami, J.N. Ganguli, Tuning the band gap of mesoporous Zr-doped TiO2 for effective degradation of pesticide quinalphos, Dalton Transactions, 42 (2013) 14480-14490.

[203] D. Guerrero-Araque, P. Acevedo-Pena, D. Ramirez-Ortega, R. Gomez, Improving photocatalytic reduction of 4-nitrophenol over ZrO2-TiO2 by synergistic interaction between methanol and sulfite ions, New Journal of Chemistry, (2017).

[204] K. Maver, U.L. Stangar, U. Cernigoj, S. Gross, R. Cerc Korosec, Low-temperature synthesis and characterization of TiO2 and TiO2-ZrO2 photocatalytically active thin films, Photochemical & Photobiological Sciences, 8 (2009) 657-662.

[205] C. Karunakaran, P. Magesan, P. Gomathisankar, P. Vinayagamoorthy, Photocatalytic Degradation of Dyes by Al_2O_3-TiO_2 and ZrO_2-TiO_2 Nanocomposites, Materials Science Forum, 734 (2013) 325-333.

[206] K. Cheng, K. Chhor, O. Brinza, D. Vrel, A. Kanaev, From nanoparticles to bulk crystalline solid: nucleation, growth kinetics and crystallisation of mixed oxide $Zr_xTi_{1-x}O_2$ nanoparticles, CrystEngComm, 19 (2017) 3955-3965.

[207] M. Benmami, K. Chhor, A.V. Kanaev, High photocatalytic activity of monolayer nanocoatings prepared from non-crystalline titanium oxide sol nanoparticles, Chemical Physics Letters, 422 (2006) 552-557.

[208] M. Benmami, K. Chhor, A.V. Kanaev, Supported Nanometric Titanium Oxide Sols as a New Efficient Photocatalyst, The Journal of Physical Chemistry B, 109 (2005) 19766-19771.

[209] M. Horn, C.F. Schwerdtfeger, E.P. Meagher, Zeitschrift für Kristallographie, 136 (1972) 273-281.

[210] G. Ehrhart, B. Capoen, O. Robbe, P. Boy, S. Turrell, M. Bouazaoui, Structural and optical properties of n-propoxide sol–gel derived ZrO2 thin films, Thin Solid Films, 496 (2006) 227-233.

[211] A.V. Emeline, V. Ryabchuk, N. Serpone, Factors affecting the efficiency of a photocatalyzed process in aqueous metal-oxide dispersions: Prospect of distinguishing between two kinetic models, Journal of Photochemistry and Photobiology A: Chemistry, 133 (2000) 89-97.

[212] G.D. Fanou, B. Yao, K. Cheng, O. Brinza, M. Traoré, A. Kanaev, K. Chhor, Elaboration of Novel NanoparticulateTiO2-P25@n-TiO2 Composite for Photocatalysis, International Journal of Advanced Applied Physics Research, 3 (2016) 19-25.

[213] B. Ohtani, Y. Ogawa, S.-i. Nishimoto, Photocatalytic Activity of Amorphous−Anatase Mixture of Titanium(IV) Oxide Particles Suspended in Aqueous Solutions, The Journal of Physical Chemistry B, 101 (1997) 3746-3752.

Annex

General process of preparing powder

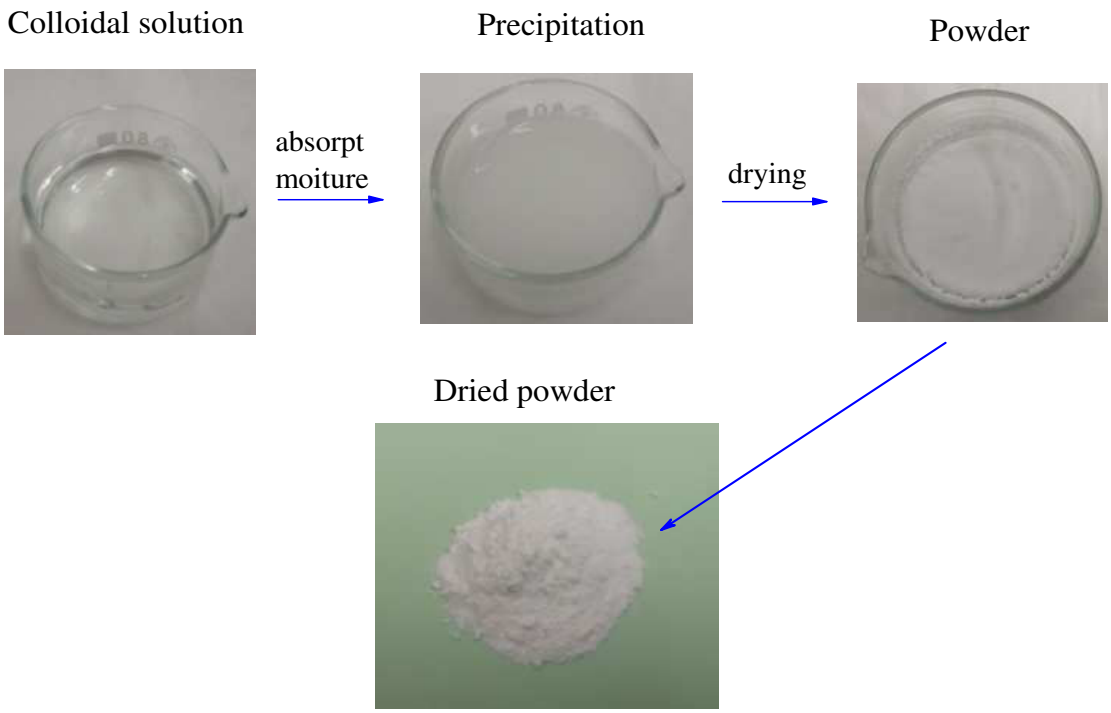

Figure annex 1: General process to get powder from colloidal solutions.

Transmission emission spectroscopy results

Some images of $Zr_xTi_{1-x}O_2$ from TEM

Crystalline of x = 0.3

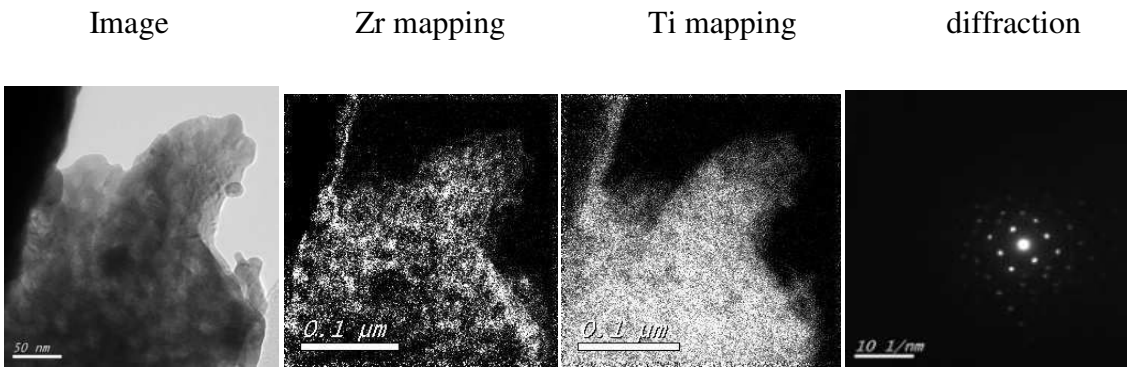

Figure annex 2: Crystalline of composite $Zr_{0.3}Ti_{0.7}O_2$ of mapping elemental and diffraction images from TEM.

Amorphous of x = 0.3

Image Zr mapping Ti mapping

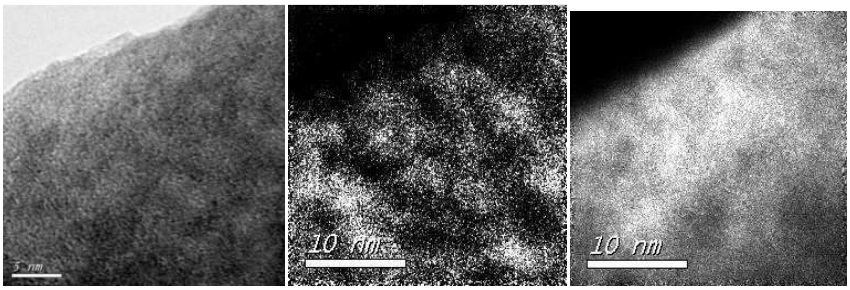

Figure annex 3: Amorphous *of oxo-$Zr_{0.3}Ti_{0.7}O_2$ of mapping elemental images from TEM.*

Crystalline of x = 0.4

Image Zr mapping Ti mapping diffraction

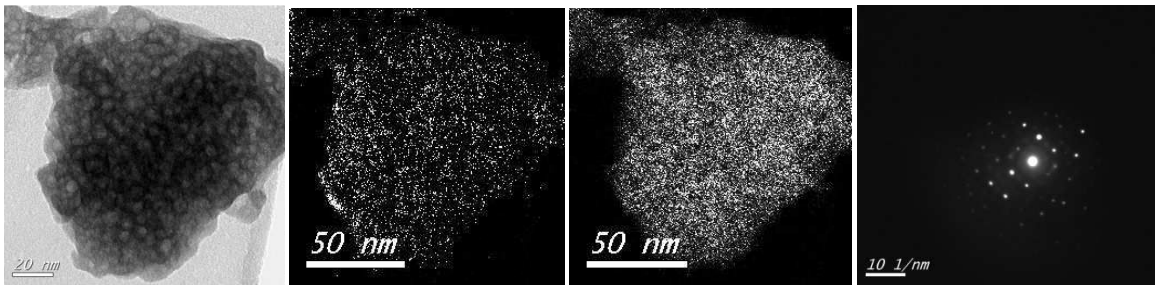

Figure annex 4: Crystalline of composite $Zr_{0.4}Ti_{0.6}O_2$ of mapping elemental and diffraction images from TEM.

Crystalline of x = 0.6

Image Zr mapping Ti mapping diffraction

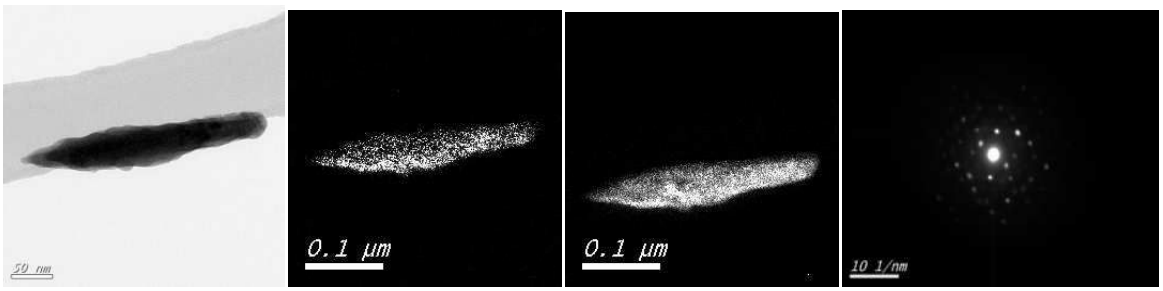

Figure annex 5: Crystalline of composite $Zr_{0.6}Ti_{0.4}O_2$ of mapping elemental and diffraction images from TEE.

Amorphous of x = 0.6

Image Zr mapping Ti mapping diffraction

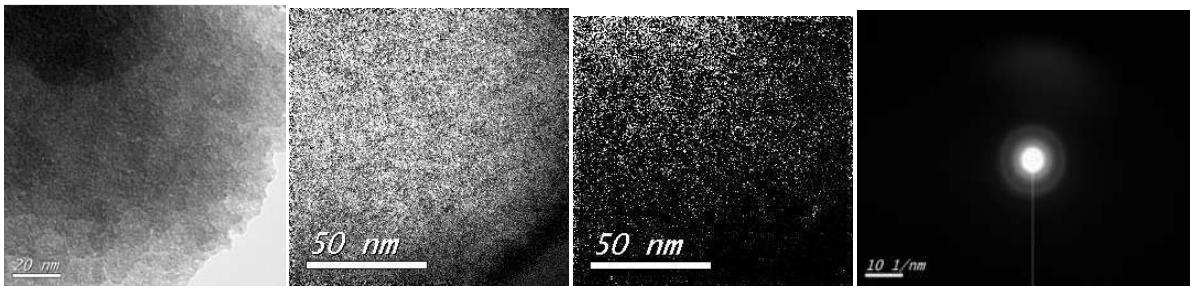

Figure annex 6: Amorphous *of oxo-$Zr_{0.6}Ti_{0.4}O_2$ of mapping elemental and diffraction images from TEM.*

Crystalline of x = 0.7

Image Zr mapping Ti mapping diffraction

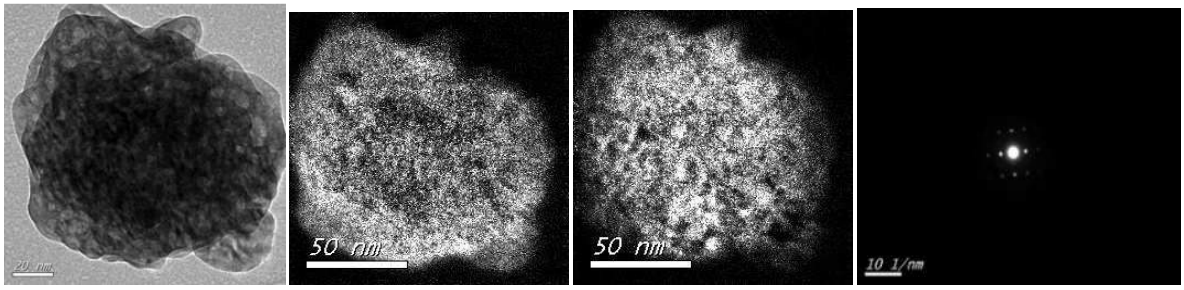

Figure annex 7: Crystalline of composite $Zr_{0.7}Ti_{0.3}O_2$ of mapping elemental and diffraction images from TEM.

Amorphous of x = 0.7

Image Zr mapping Ti mapping

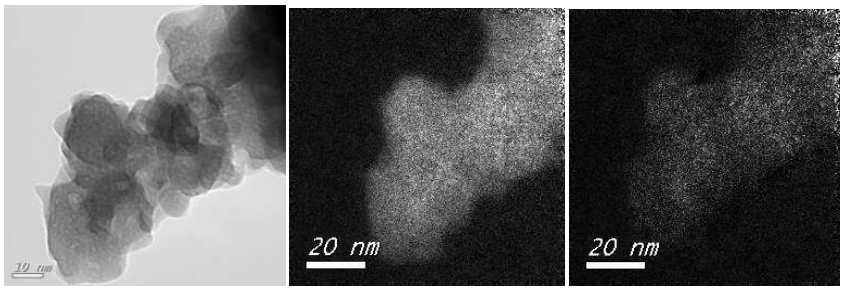

Figure annex 8: Amorphous *of oxo-$Zr_{0.7}Ti_{0.3}O_2$ of mapping elemental images from TEM.*

Band gaps in anatase domain

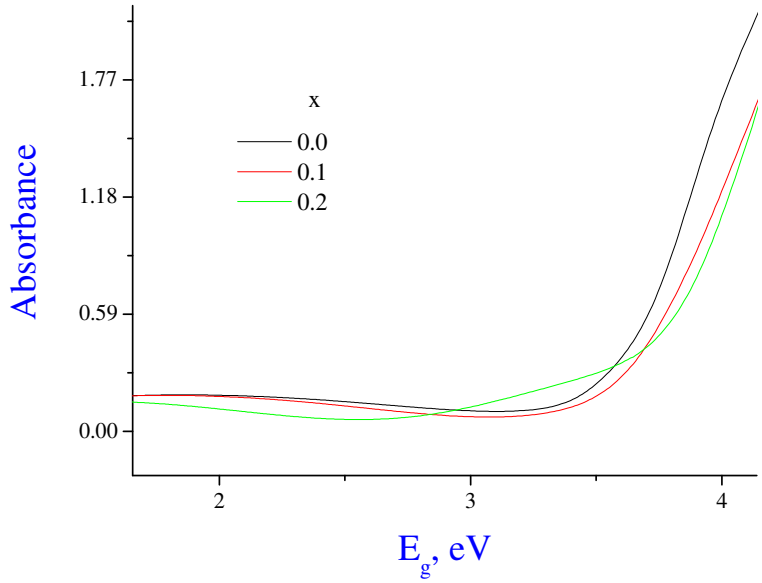

Figure annex 9: The absorbance of mixed $Zr_xTi_{1-x}O_2$ in photocatalysis domain.

Photocatalytic results

Photocatalysts of pure ZrO_2

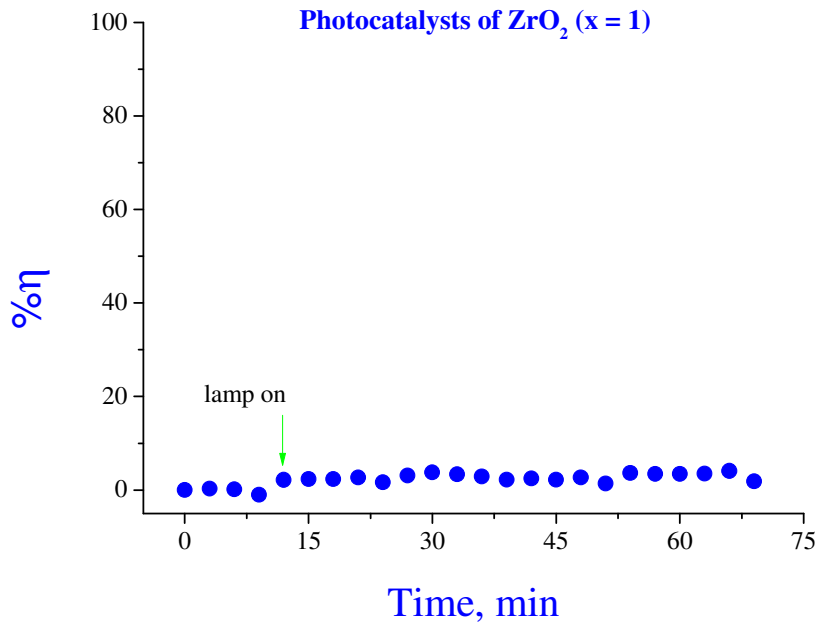

Figure annex 10: Photocatalytic activity of composite ZrO_2: $T_{calcinations}$ = 500 °C, $C_{Ethylene}$ = 120 ppm, RL = 15 cm (3.78 g), λ = 362 ± 11 nm, flow rate = 60:40 mL/min (air:ET).

Photocatalysts at 60 ppm pollutant concentration

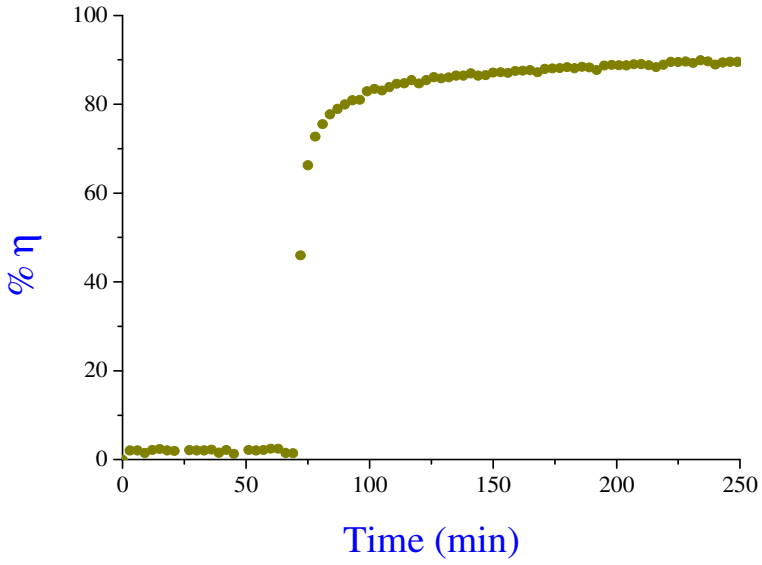

Figure annex 11: Photocatalytic activity of composite $Zr_{0.04}Ti_{0.96}O_2$: $T_{calcinations}$ = 500 °C, $C_{Ethylene}$ = 60 ppm and flow rate = 40:35 (air:ET), RL = 5 cm (1.29 g), λ = 362 ± 11 nm.

Photocatalysts at 300 ppm pollutant concentration

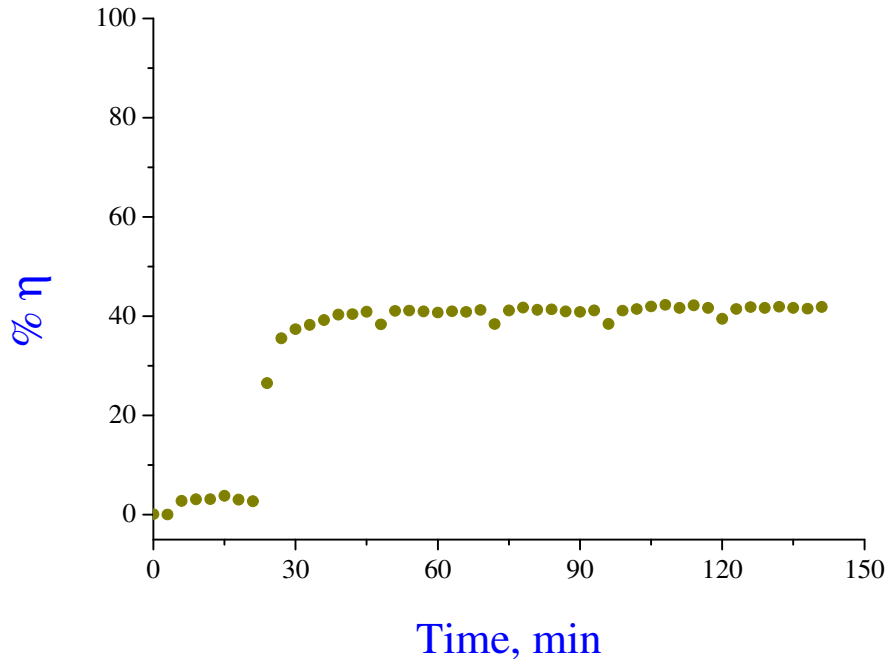

Figure annex 12: Photocatalytic activity of composite $Zr_{0.04}Ti_{0.96}O_2$: $T_{calcinations}$ = 500 °C, $C_{Ethylene}$ = 300 ppm and flow rate = 40:35 (air:ET), RL = 5 cm (1.29 g), λ = 362 ± 11 nm.

Résumé

Ce présent mémoire porte sur l'élaboration de composites nanoparticulaires $Zr_xTi_{1-x}O_2$, de l'étape de nucléation des nanoparticules au solide cristallin massif ainsi que sur leur application en photocatalyse. La synthèse a été réalisée dans un réacteur sol-gel à micromélange utilisant des précurseurs d'isopropoxyde de titane (IV) et de propoxyde de zirconium (IV) dans différents rapports molaires et taux d'hydrolyse. Ces expériences ont conduit à la formation de nanoparticules amorphes monodisperses oxo-alcoxy de zirconium-titane (ZTOA) de rayon R = 1,6 nm pour $0 \leq x \leq 0,2$, R = 2,1 nm pour $0,3 \leq x \leq 0,6$ et des particules oxo-alcoxy de zirconium (ZOA) de rayon R = 1,8 nm pour $0,7 \leq x \leq 1$. Celles-ci se transforment, après traitement thermique, en cristallite nanoporeux respectivement dans les phases anatase, orthorhombique et monoclinique / tétragonale. La température du début de transition dépend significativement de la composition x. Les particules d'anatase de composition $0 < x < 0,2$ ont été sélectionnées pour des applications photocatalytiques en phase gazeuse (éthylène) et en phase liquide (MB et phénol). La meilleure performance photocatalytique a été obtenue pour un matériau de composition optimale x = 0,0425 et traitée thermiquement à 500 °C. L'activité la plus forte enregistrée est pratiquement deux fois celle du TiO_2 pur préparé dans les mêmes conditions.

Mots-clés: composite $Zr_xTi_{1-x}O_2$, réacteur sol-gel à micromélange, nanoparticules, dispersion, photocatalyseur

Abstract

The PhD study is focused on synthesis of nanoparticulate $Zr_xTi_{1-x}O_2$ composites: from nucleation stage of nanoparticles to bulk crystalline solid and their application in photocatalysis. The synthesis was achieved in a sol-gel micromixing reactor using titanium(IV) isopropoxide and zirconium(IV) propoxide precursors in different molar and hydrolysis ratios, resulting in monodispersed zirconium-titanium oxo-alkoxy (ZTOA) nanoparticles: R=1.6 nm for $0 \leq x \leq 0.2$, R=2.1 nm for $0.3 \leq x \leq 0.6$ with orthorambic and ZOA of R=1.8 nm for $0.7 \leq x \leq 1$. They convert after heat treatment to nanoporous crystallite in respectively anatase, orthorambic and monoclinic/tetragonal crystalline phases, which onset temperature depend on x. The anatase compositions ($0 \leq x \leq 0.2$) were selected for photocatalytic applications in gas phase (ethylene) and liquid phase (MB and phenol) degradation. The optimum composition x=0.0425 heat treated at 500 °C revealed the strongest activity, two times higher than pure TiO_2. We found that the photocatalytic activity directly correlates with the specific surface area.

Keywords: Composite $Zr_xTi_{1-x}O_2$, sol-gel micromixing reactor, nanoparticles, dispersity, photocatalyst